DEVELOPMENT OF WHITE-LIGHT AND LASER-LIGHT BASED DIGITAL IMAGE CORRELATION FOR MATERIALS CHARACTERIZATION, NON-DESTRUCTIVE TESTING AND TEMPERATURE MEASUREMENT

by

SIYUAN FANG

A dissertation submitted in partial fulfillment of the
requirements for the degree of

DOCTOR OF PHILOSOPHY IN MECHANICAL ENGINEERING

2026

Oakland University
Rochester, Michigan

Doctoral Advisory Committee:

Liaxiang Yang, Ph.D., Chair
Gary Barber, Ph.D.
Hongwei Qu, Ph.D.
Marco Gerini Romagnoli, Ph.D.

To my mother and father, for encouraging me to pursue knowledge and never give up.

ACKNOWLEDGMENTS

I would like to express my sincere gratitude to my advisors, Professor Lianxiang Yang, for his continuous guidance, insightful discussions, and unwavering support throughout my Ph.D. study. His expertise, encouragement, and high standards have profoundly shaped my research thinking and academic growth. I also appreciate the members of my dissertation committee for their time, valuable feedback, and constructive suggestions. I am grateful to the faculty and staff in the Department of Engineering and Computer Science at Oakland University for providing a supportive research environment and for their assistance with laboratory resources, equipment access, and administrative coordination. Finally, I am deeply thankful to my family for their unconditional love, patience, and encouragement. This dissertation would not have been possible without the help and support of all these individuals and institutions.

Siyuan Fang

PREFACE

This dissertation focuses on speckle-based optical metrology for the characterization of sheet-metal materials, non-destructive testing (NDT) and temperature measurement. The work is organized around two themes. The first is the development of a white-light multi-camera (double-side) digital image correlation (DIC) system for accurate mechanical property characterization. By observing both faces of a specimen in a unified measurement frame, the system enables direct thickness strain measurement together with in-plane strains under standard tensile loading. This capability is used to realize direct R-value measurement without volume constant assumption, to identify the onset of localized necking via cross-sectional area evolution, and to obtain corrected tensile properties of heat-affected zones (HAZ) in tailor-welded blanks (TWB). The second theme is the development of laser-light speckle based methods for deformation and temperature measurement and for NDT. Here, controlled laser speckle is used as a high-contrast carrier for digital image correlation and as a background for background-oriented schlieren (BOS) technique. The research results aim to provide both methodological contributions and practical guidance for applying advanced optical techniques to sheet-metal mechanics and related NDT problems.

ABSTRACT

DEVELOPMENT OF WHITE-LIGHT AND LASER-LIGHT BASED DIGITAL IMAGE CORRELATION FOR MATERIALS CHARACTERIZATION, NON-DESTRUCTIVE TESTING AND TEMPERATURE MEASUREMENT

by

Siyuan Fang

Adviser: Lianxiang Yang, Ph.D.

In sheet-metal forming, material elongation is commonly accompanied by rapid thinning, making thickness strain measurement important. While digital image correlation (DIC) is widely used for deformation measurement, a typical stereo DIC setup observes only one surface and thus cannot directly access thickness information. This work employs a white-light multi-camera DIC system that images both surfaces in a unified measurement frame, enabling direct measurement of thickness strain together with in-plane strains. We further improve thickness-strain measurement accuracy and demonstrate three applications: (1) direct R-value measurement without relying on volume-constancy assumptions; (2) identification of localized necking onset by analyzing the evolution of local cross-sectional area; and (3) tensile characterization of heat-affected zones (HAZ) in tailor-welded blanks (TWB), in which front- and back-surface strain fields are recorded and analyzed to reduce geometry-induced bending effects and to correct the HAZ stress–strain curve. Collectively, these applications demonstrate the advantages and practical utility of the multi-camera DIC system for characterizing sheet-

metal properties. Beyond sheet-metal mechanics, this dissertation further develops laser-light speckle based optical methods for deformation and temperature measurement and for non-destructive testing (NDT). Controlled laser speckle is used as a high-contrast carrier for DIC, enabling robust deformation measurements under challenging conditions such as high temperature, small deformation, and biomaterials. In addition, laser speckle is employed as the background pattern for background-oriented schlieren (BOS), enabling quantitative temperature measurements that are directly compared with holographic interferometry. Furthermore, we investigate load- and temperature-induced decorrelation of laser speckle patterns as a potential new method for NDT, using correlation coefficient as indicators of local deformation. The basic theory, system configurations, results analysis and applications are shown in detail in this dissertation.

TABLE OF CONTENTS

ACKNOWLEDGMENTS iv

PREFACE v

ABSTRACT vi

LIST OF TABLES xi

LIST OF FIGURES xii

LIST OF ABBREVIATIONS xxi

CHAPTER ONE
INTRODUCTION AND SCOPE OF WORK 1

1.1 Background and motivation 1

1.2 Objectives and scope of work 4

1.3 Organization of the dissertation 5

CHAPTER TWO
FUNDEMENTAL OF DIGITAL IMAGE CORRELATION 7

2.1 Principles and workflow of digital image correlation 7

2.1.1 Overview of the DIC workflow 7

2.1.2 Speckle pattern requirements and image quality 10

2.1.3 Subset size and grid spacing 13

2.1.4 Shape function 15

2.1.5 Correlation criterion 18

2.1.6 Integer-pixel initialization and search strategies 20

2.1.7 Sub-pixel interpolation 22

2.1.8 Optimization algorithms for sub-pixel DIC 23

TABLE OF CONTENTS-CONTINUED

2.2 Stereo three-dimensional DIC 24

2.2.1 Camera model 24

2.2.2 Lens distortion 27

2.2.3 Camera calibration 29

2.2.4 Epipolar geometry 30

2.2.5 Triangulation and 3D reconstruction 32

2.3 Multi-camera (double-side) DIC 34

2.3.1 Thickness strain reconstruction 35

2.3.2 Eliminate thickness strain noise by RANSAC 36

2.3.3 Thickness and thickness-strain evaluation 38

2.3.4 Thickness-strain accuracy optimization 39

SECTION ONE
WHITE-LIGHT SPECKLE DIC FOR MATERIALS CHARCTERIZATION

CHAPTER THREE
DIRECT R-VALUE MEASUREMENT 42

3.1 Introduction to R-value 42

3.2 Experimental results and discussion 44

3.3 Summary 50

CHAPTER FOUR
LOCALIZED NECKING DETECTION 52

4.1 Introduction to localized necking 52

4.2 Localized necking detection based on cross-sectional area evolution 54

TABLE OF CONTENTS-CONTINUED

4.2.1 Cross-sectional area from thickness and width engineering strains 55

4.2.2 Determination of the necking boundary 56

4.2.3 Time-dependent cross-sectional area criterion for necking onset 57

4.2.4 Determination of limit strains at necking onset 58

4.3 Experimental results 59

4.4 Comparison and discussion 66

4.5 Summary 69

CHAPTER FIVE
TENSILE PROPERTIES OF HAZ IN TAILOR-WELDED BLANKS WITH UNEVEN THICKNESS 72

5.1 Introduction to HAZ 72

5.2 Experimental methodology 74

5.2.1 Materials and sample preparation 74

5.2.2 Microhardness test 75

5.2.3 Nanoindentation test 76

5.2.4 Tensile test set up 78

5.3 Experimental results and discussion 79

5.3.1 Micorhardness distribution 79

5.3.2 Nanoindentation for Young’s modulus measurements 80

5.3.3 Determination of HAZ position from the thickness distribution 81

5.3.4 Temporal and spatial distribution of major strains 82

5.3.5 Effect of bending in tensile tests 85

5.3.6 Tensile behavior in HAZ 87

5.3.7 A novel approach to calibrate stress-strain curves in HAZ with uneven thickness 89

5.4 Summary 94

SECTION TWO
LASER-LIGHT SPECKLE DIC FOR DEFORMATON, TEMPERATURE MEASUREMENT AND NDT

CHAPTER SIX
LASER-LIGHT SPECKLE DIC FOR DISPLACEMENT AND STRAIN MEASUREMENT 97

6.1 Introduction 97

6.2 Generation and characteristics of laser-light speckle 98

6.2.1 Laser-light speckle pattern 98

6.2.2 Optimization of laser-light speckle quality 100

6.3 Experiment for displacement and strain measurement 105

6.3.1 Decorrelation 105

6.3.2 Solutions for decorrelation 108

6.3.3 Small displacement gradient measurement 111

6.3.4 Out-of-plane displacement measurement 114

6.3.5 Tensile test strain measurement 115

6.4 Summary 116

TABLE OF CONTENTS-CONTINUED

CHAPTER SEVEN
TEMPERATURE MEASUREMENT USING BOS WITH LASER-LIGHT SPECKLE AND HOLOGRAPHY 119

7.1 Introduction 121

7.2 Fundamental of BOS and ESPI 122

7.2.1 BOS 121

7.2.2 Holographic interferometry 123

7.2.3 Temperature field reconstruction 125

7.2.4 New synchronous measurement design 126

7.3 Experimental results and discussion 128

7.3.1 Accuracy 130

7.3.2 Uncertainty 133

7.3.3 Sensitivity 137

7.4 Summary 141

CHAPTER EIGHT
LASER-LIGHT SPECKLE DECORRELATION FOR NDT 143

8.1 Introduction 143

8.2 Decorrelation theory 145

8.2.1 Speckle field model under local surface tilt 146

8.2.2 ZNCC-based decorrelation operator 146

8.2.3 Ring-shaped decorrelation pattern 149

8.3 Decorrelation image enhancement and automatic defect detection 150

8.3.1 Decorrelation image enhancement for weak response 150

8.3.2 Automatic defect detection based on YOLOv8 152

8.4 Experimental results and discussion 155

8.4.1 Experimental set-up and decorrelation behavior 155

8.4.2 Image enhancement results 156

8.4.3 Automatic defect detection results 158

8.5 Comparison with holography and shearography 162

8.6 Summary 165

CHAPTER NINE
CONCLUSION 167

REFERENCES 170

LIST OF TABLES

Table 4.1	Results of limit strain for BH240	69
Table 4.2	Results of limit strain for DP590	69
Table 5.1	The regression statistical analysis of the nominal strain, front surface strain and back surface strain in the elastic stage	93
Table 5.2	Comparison of Young’s Modulus, yield strength and tensile strength	94
Table 6.1	Displacement measurement performance of laser-light speckle and white-light speckle	114
Table 7.1	Percent error of temperature of BOS method versus holographic interferometry and thermocouple along radial distributions at 10mm heights	133
Table 7.2	Percent error of temperature of BOS method versus holographic interferometry and thermocouple along radial distributions at 30mm heights	133
Table 7.3	Percent error of temperature of BOS method versus holographic interferometry and thermocouple along radial distributions at 50mm heights	133
Table 7.4	Average background speckle pattern displacement under different conditions	140

LIST OF FIGURES

Figure 2.1	The workflow of DIC	10
Figure 2.2	Speckle pattern: (a)Painted speckle; (b)Laser speckle; (c)Natural speckle (rock)	13
Figure 2.3	The concept of subset and grid spacing	14
Figure 2.4	The schematic of deformation model in shape function	18
Figure 2.5	The schematic of pinhole camera model	27
Figure 2.6	The schematic of two types of lens distortion: (a) Barrel distortion; (b) Pincushion distortion	29
Figure 2.7	Checkboard calibraiton patttern	30
Figure 2.8	The schematic of epipolar geometry	32
Figure 2.9	The schematic of the double-side DIC system	36
Figure 2.10	Double-side calibration board	38
Figure 2.11	Thickness strain history with noise	41
Figure 2.12	Thickness strain history after RANSAC fitting	42
Figure 3.1	Experimental set-up of the R-value measurement	48
Figure 3.2	The schematic diagram of DP 980	48
Figure 3.3	Full field strain distribution of sample surface measured by DIC system: (a) distribution of length strain; (b) distribution of width strain; (c) distribution of thickness strain	48
Figure 3.4	Calculation area of R-value: (a) Non-necking area; (b)Necking area	49
Figure 3.5	The R-value curve by two different measurement methods in the non-necking area	49
Figure 3.6	The R-value curve by two different measurement methods in the necking area	49

Figure 4.1	Areas not covered appear at the edge	55
Figure 4.2	Width and thickness strain distributions along the cross section: (a) Before necking; (b) Necking stage	56
Figure 4.3	The schematic of the proposed localized necking detection method: (a) Cross-sectional area evolution curve; (b) Determination of boundary of the necking region	57
Figure 4.4	Full field engineering strain distribution of BH240: (a) Length strain; (b) Width strain; (c) Thickness strain	61
Figure 4.5	Spatial distribution of thickness strain and curvature of BH240	61
Figure 4.6	Cross-sectional area evolution curves located in different regions for BH240	62
Figure 4.7	First-order derivative of line 3 for BH240	62
Figure 4.8	Determination of limit major strain and limit minor strain at localized necking time for BH240	63
Figure 4.9	Full field engineering strain distribution of DP590: (a) Length strain; (b) Width strain; (c) Thickness strain	64
Figure 4.10	Spatial distribution of thickness strain and curvature of DP590	64
Figure 4.11	Cross-sectional area evolution curves located in different regions for DP590	65
Figure 4.12	First-order derivative of line 3 for DP590	65
Figure 4.13	Determination of limit major strain and limit minor strain at localized necking time for BH240	66
Figure 4.14	Determination of localized necking strain for BH240 by different methods.: (a) ISO method; (b) Curvature method; (c) Bifurcation method; (d) Second derivative method	69
Figure 5.1	The schematic of specimen waterjet cutting	75

Figure 5.2 Microhardness test specimen and test lines 75

Figure 5.3 A typical load-depth curve 77

Figure 5.4 The schematic of the sample surface before and after loading 77

Figure 5.5 Vickers hardness profile across the weld seam 80

Figure 5.6 Nanoindentation test results of HAZ 1, FZ and HAZ 2: (a) Young's modulus profile; (b) Average Young's Modulus 81

Figure 5.7 Identification of HAZ: (a) Full-field color contour of thickness distribution; (b) Thickness profile along a 10 mm-long line gauge across the weld seam 82

Figure 5.8 Full-field major strains distribution on the front and back sides of the tensile specimen at different maximum strain levels of 0.5%, 5%, 10% and 16% 84

Figure 5.9 The spatial distribution of major strains across the weld seam at different maximum strain levels of 0.5%, 5%, 10% and 16% 84

Figure 5.10 Full-field standard deviation of major strains distribution on the front and back sides of the tensile specimen at different maximum strain levels of 0.5%, 5%, 10% and 16% 85

Figure 5.11 Section of TWB specimen with internal loads 86

Figure 5.12 Spatial distribution of out-of-plane displacement at different times during tensile tests 87

Figure 5.13 Tensile behaviors in HAZ: (a) Major strains history; (b) Engineering stress-strain curves 88

Figure 5.14 The schematic of the proposed stress-strain curve calibration method 91

Figure 5.15 The regression statistical analysis of the nominal strain, front surface strain and back surface strain in the elastic stage 93

Figure 5.16 (a) Corrected major strain evolutions; (b) Corrected engineering stress-strain curves in HAZ 1 94

Figure 6.1	Generation of laser-light speckle: (a) Objective speckle; (b) Subjective speckle	100
Figure 6.2	Laser speckle patterns at different apertures and quality assessment results	102
Figure 6.3	Laser speckle patterns at different beam expander and quality assessment results	103
Figure 6.4	Laser speckle patterns at different laser power and quality assessment results	104
Figure 6.5	Experimental setup for displacement of laser-light speckle and white-light speckle	107
Figure 6.6	Full-field displacement results of laser-light speckle and white-light speckle	107
Figure 6.7	(a) Average displacement results; (b) Displacement errors relative to the micro-displacement platform	108
Figure 6.8	Laser-light speckle displacement error compensation by linear fitting	109
Figure 6.9	Comparison of sequential and incremental correlation	111
Figure 6.10	Cumulative error generation in the incremental correlation	111
Figure 6.11	Experimental set-up for small displacement gradient measurement	113
Figure 6.12	Full-field vertical displacement measurement results: (a) Holography; (b)Laser-light speckle DIC; (c) White-light speckle DIC.	113
Figure 6.13	(a) Spatial displacement distribution along the 120mm gauge line; (b) Average percent error relative to the holography	113
Figure 6.14	Failure of laser-light speckle dual camera matching	115
Figure 6.15	Experimental set-up for tensile test	116

Figure 6.16	Stress-strain curve of DP 980	116
Figure 7.1	Background-oriented Schlieren schematic	123
Figure 7.2	Holographic interferometry schematic	125
Figure 7.3	The schematic diagram of synchronous measurement of temperature field	127
Figure 7.4	Experimental set-up	128
Figure 7.5	Experiment results from BOS: (a) Displacement in x direction; (b) Displacement in y direction; (c) Temperature field map	129
Figure 7.6	Experiment results from holographic interferometry: (a) Phase map; (b) Unwrapped phase map; (c) Temperature field map	130
Figure 7.7	Temperature field distribution along the radial direction at different heights from the alcohol lamp flame: (a) 10mm height; (b) 30mm height; (c) 50mm height	132
Figure 7.8	Correlation coefficient map	137
Figure 7.9	Uncertainty of x-displacement obtained by the software used from Dantec Dynamic GmbH, Germany	137
Figure 7.10	Horizontal displacement distribution under different L_b conditions	139
Figure 7.11	Horizontal displacement distribution under different f conditions	140
Figure 7.12	Average background speckle pattern displacement	140
Figure 7.13	Phase map under different L_b conditions	141
Figure 7.14	Phase map under different f conditions	141
Figure 8.1	Schematic illustration of defect-induced local deformation before and after loading	146
Figure 8.2	The typical ring-shaped decorrelation pattern	150

Figure 8.3 The YOLOv8 network for automatic defect detection 154

Figure 8.4 The workflow of proposed method 154

Figure 8.5 The experimental set-up 156

Figure 8.6 Evolution of decorrelation maps for a specimen with three defects under heat-gun excitation 156

Figure 8.7 Enhancement of weak decorrelation signatures under small loading: (a) Raw decorrelation map under small thermal loading; (b) Effect of linear contrast stretching parameter k on the decorrelation map (γ=1); (c)Effect of gamma correction γ on the decorrelation map (k=5) 158

Figure 8.8 Representative decorrelation defect images in dataset 159

Figure 8.9 Training convergence curves of YOLOv8 in terms of (a) mAP_{50} and (b) $\mathrm{mAP}_{50:95}$. 161

Figure 8.10 Representative YOLOv8 detection results on the test set: (a) Weak signature case. (b) Multiple defect case. (c) Difeerent defect shape case 162

Figure 8.11 Sensitivity comparison under vacuum-loading conditions: (a) Decorrelation maps; (b) Holograms; and (c) Shearograms 163

Figure 8.12 YOLOv8 detection results on decorrelation maps under vacuum loading 164

LIST OF ABBREVIATIONS

AP	Average Precision
BCE	Binary Cross-Entropy
BOS	Background-oriented Schlieren
CCD	Charge Coupled Device
DIC	Digital Image Correlation
ESPI	Electronic Speckle Pattern Interferometry
FLD	Forming Limit Diagram
FZ	Fusion Zone
HAZ	Heat-affected Zone
MAD	Median Absolute Deviation
NCC	Normalized Cross-Correlation
NDT	Non-destructive Testing
PZT	Piezoelectric Transducer
RANSAC	Random Sample Consensus
SPPF	Spatial Pyramid Pooling-Fast
SAD	Sum of Absolute Differences
SSD	Sum of Squared Differences
TWB	Tailor Welded Blanks
ZNCC	Zero-mean Normalized Cross-correlation
ZNSSD	Zero-mean Normalized Sum of Squared Differences

CHAPTER ONE

INTRODUCTION AND SCOPE OF WORK

1.1 Background and motivation

Accurate characterization of deformation and failure in sheet-metal components is a key enabler for lightweight design in automotive, aerospace, and other manufacturing industries [1-2]. Modern forming processes exploit the full deformation capacity of advanced high-strength steels and aluminum alloys, often operating close to forming limits in order to reduce thickness and mass while maintaining structural integrity. In parallel, and tailor welded blanks (TWB) are increasingly used to locally thickness and strength, which introduces spatially varying mechanical properties, especially in the heat-affected zone (HAZ). As a result, there is a growing need for experimental techniques that can provide reliable, spatially resolved information on material behavior under realistic loading conditions.

Classical mechanical testing methods typically rely on global load–displacement curves and localized mechanical gauges such as extensometers or strain gauges. While these approaches remain important, they provide only limited insight into the full-field deformation and are not well suited to capture local phenomena such as strain localization, necking, or property gradients in welds. Optical full-field techniques, in particular digital image correlation (DIC), have therefore become standard tools in experimental mechanics [3-5]. DIC provides non-contact measurements of displacement and strain fields based on images of a random speckle pattern applied to the specimen surface. It can be used with standard testing machines and can accommodate a wide

wide variety of specimen geometries [6-19].

Despite these advantages, several critical challenges remain when using conventional DIC for sheet-metal forming and welded structures. One of the most important is the characterization of thickness deformation. In sheet-metal forming, material elongation is commonly accompanied by thinning, and the evolution of thickness strain has strong implications for R-value evaluation, necking behavior, and stress state in welded regions. Yet in most experimental studies, thickness strain is not measured directly; instead, it is inferred from assumptions such as volume constancy or from pointwise thickness measurements, which may not accurately represent the local behavior within the gauge section.

A second challenge arises in the characterization of TWB. The presence of thickness transitions, weld beads, and HAZ softening or strengthening leads to complex strain and stress distributions. Under tensile loading, the mismatch in stiffness and geometry can cause pronounced bending and non-uniform stress states, making it difficult to extract reliable tensile properties for the HAZ from conventional “one-side” measurements.

Digital image correlation has become one of the most widely used optical metrology techniques in solid mechanics. In its standard three-dimensional implementation, a stereo pair of cameras observes a single surface, and three-dimensional coordinates and displacement are reconstructed by correlating images of a speckle pattern before and after deformation. For sheet-metal testing, conventional stereo DIC provides detailed in-plane strain fields and out-of-plane displacement on the observed surface. However, when only one surface is measured, the thickness strain must be inferred indirectly. In many studies, this inference relies on the volume constant assumption combined with estimates of the in-plane strains. This can be adequate in some regimes, but it does not capture asymmetry or complexity in the strain distribution through the thickness, nor does it provide a direct experimental basis to validate the assumptions.

To overcome this limitation, multi-camera (double-side) DIC extends the idea of stereo vision by simultaneously imaging both front and back surfaces of the specimen and reconstructing their deformation in a unified coordinate system [20]. This configuration opens the possibility to directly estimate thickness changes and associated thickness strain from geometrical information rather than purely from constitutive assumptions, while preserving the advantages of full-field, non-contact measurement.

Laser-light speckle plays an important role in DIC and other optical methods [21-28]. When coherent laser-light illuminates a rough surface or a random diffuser, it generates a granular speckle pattern that can serve as a natural or engineered texture for correlation. Compared to painted white-light speckles, laser-light speckle can offer higher contrast and tunable grain size by adjusting optical parameters. However, the same coherence that enhances image quality also makes laser-light speckle sensitive to decorrelation: small changes in surface geometry, illumination angle can lead to substantial changes in the intensity pattern. This sensitivity is a double-edged sword. On one hand, decorrelation can degrade correlation algorithms; on the other hand, decorrelation itself may carry information about underlying physical changes and can therefore be explored as a new indicator in non-destructive testing (NDT). Moreover, laser speckle can be used as a background pattern in background-oriented schlieren (BOS) techniques, where apparent displacements in the background pattern are used to infer refractive-index gradients and, ultimately, temperature fields in transparent media. Combining laser speckle with BOS and interferometric methods, such as holographic interferometry, enables optical measurements for temperature and flow.

1.2 Objectives and scope of work

The overarching goal of this dissertation is to develop and validate speckle-based optical methods that enable accurate measurement of deformation and temperature, with a focus on sheet-metal property characterization and on optical techniques that can inform NDT. This broad goal is pursued through two main research directions:

(i) White-light multi-camera DIC for sheet-metal mechanics.

The first direction focuses on the development and application of a multi-camera DIC system that observes both faces of a sheet specimen in a unified measurement frame. The objectives are to:

- design and implement a dual-side configuration and calibration procedure for simultaneous front–back imaging;
- reconstruct full-field in-plane and thickness strains under tensile loading;
- use dual-side measurements to enhance materials property characterization, including direct R-value measurement without volume-constancy assumptions;
- propose and evaluate a localized necking onset criterion based on the evolution of local cross-sectional area; and
- establish methods to correct stress–strain curves and extract tensile properties of weld HAZ in TWB by mitigating bending effects using front–back strain information.

(ii) Laser-light speckle-based deformation and temperature measurement and NDT.

The second direction develops laser-speckle–based optical methods for deformation and temperature measurements and explores their relevance to NDT. The objectives are to:

• investigate the generation and control of laser speckle as a high-contrast carrier for DIC under challenging conditions such as high temperature, small deformation, and reflective surfaces;

• study load- and temperature-induced decorrelation of speckle patterns as a potential indicator of local mechanical or thermal changes;

• use laser speckle as a background pattern for BOS and compare the resulting temperature measurements with those obtained from holographic interferometry.

The scope of this work is primarily experimental. The material systems considered are metallic sheets relevant to automotive and structural applications, including base materials and TWB with defined thickness transitions and weld configurations. The main tests are uniaxial tensile tests under controlled conditions. The optical setups include multi-camera dual-side DIC systems, laser-light speckle DIC configurations, and BOS/holography arrangements with speckle backgrounds.

1.3 Organization of the dissertation

The remainder of this dissertation is organized as follows.

Chapter 2 introduces the necessary background and fundamental on DIC, camera calibration, multi-camera 3D reconstruction. Chapters 3–5 constitute the first part of the work and focus on the development and application of the multi-camera DIC system for sheet-metal mechanics. Chapter 3 addresses direct R-value measurement based on combined in-plane and thickness strains. Chapter 4 presents a localized necking onset criterion derived from the evolution of local cross-sectional area. Chapter 5 deals with tensile characterization and stress–strain curve correction for weld HAZs in tailor-welded blanks using front–back strain data. Chapters 6–7 form the second part of the work and address laser-light speckle–based methods for deformation, temperature measurement, and the exploration of decorrelation phenomena as potential NDE indicators. Chapter 6 discusses speckle DIC, speckle generation, and decorrelation under mechanical and thermal loading. Chapter 7 presents temperature measurement using BOS with laser speckle as a background and compares the results with holographic or interferometric methods, with an emphasis on sensitivity, uncertainty, and robustness.

CHAPTER TWO

FUNDAMENTALS AND METHODOLOGY OF DIGITAL IMAGE CORRELATION

2.1 Principles and workflow of digital image correlation

DIC has become a standard full-field measurement technique in experimental mechanics due to its non-contact nature, flexibility in specimen geometry, and compatibility with conventional loading systems. This section provides a step-by-step review of the DIC workflow and the major technical choices at each stage, including subset definition and shape functions, correlation criteria, search and sub-pixel refinement schemes, reliability assessment, and strain evaluation. The purpose is to establish a consistent notation and methodological baseline for the stereo/3D and double-side formulations introduced later in this chapter and used throughout the dissertation.

2.1.1 Overview of the DIC workflow

DIC is a speckle-based, image-driven measurement technique that estimates displacement and strain by comparing a reference image of a specimen surface with one or more images acquired after deformation. Although numerous variants exist (2D/3D, local/global, white-light/laser-light), most DIC implementations follow a common workflow. A standard DIC workflow can be summarized into several stages, as illustrated conceptually in figure 2.1.

(1) Speckle pattern preparation / texture formation.

DIC requires a spatially random intensity texture on the measured surface. In practice this is provided by a painted speckle pattern under incoherent illumination or by laser speckle formed by coherent scattering. The pattern must contain sufficient grayscale gradients within each subset to ensure uniqueness of the match; otherwise, correlation becomes ill-posed and the displacement estimate becomes noisy or unstable.

(2) Image acquisition and experimental imaging control.

Reference and deformed images must be acquired with stable view geometry and adequate image quality. Key factors include focus, depth of field, exposure, motion blur, sensor noise, and illumination stability. For stereo/3D DIC and multi-camera configurations, synchronization and rigid mounting are essential. In long experiments or thermal tests, intensity drift and refractive-index fluctuations can become additional sources of decorrelation, motivating normalized correlation criteria and robust processing.

(3) Subset definition, and grid design.

The surface is discretized into a grid of calculation points. Around each point, a subset (correlation window) is defined, typically square. Two parameters dominate this stage: subset size (controls robustness vs spatial resolution) and step size (controls output density and computational cost). Masking strategies are often applied to exclude holes, edges, glare regions, and areas with poor texture, because incomplete or contaminated subsets frequently cause outliers.

(4) Similarity measure (correlation criterion) selection.

A correlation criterion quantifies how well a reference subset matches a candidate deformed subset. Common choices include ZNCC/ZNSSD for robustness to brightness offset/scale changes, and more specialized criteria (e.g., gradient-based or robust norms) for challenging imaging conditions. This selection directly affects sensitivity to illumination drift and the stability of the optimization.

(5) Integer-pixel initialization.

Because the correlation objective is generally non-convex, DIC requires a good initial guess. Coarse matching is typically performed at integer-pixel resolution using a search window, multi-scale image pyramids, or predictors from neighboring points and previous frames. Reliable initialization is especially important when large rigid-body motion, rapid deformation, or abrupt local changes occur.

(6) Sub-pixel refinement via an optimization solver.

With a coarse estimate available, DIC refines the displacement (and possibly deformation parameters within the subset) to sub-pixel precision. This step involves image interpolation for non-integer coordinates and iterative optimization (e.g., Gauss–Newton/Newton–Raphson, inverse compositional schemes, or Levenberg–Marquardt). The deformation (shape) function order (0th/1st/2nd) determines the parameter set solved in this refinement.

(7) Quality assessment and outlier handling.

DIC outputs are commonly accompanied by quality metrics such as correlation coefficient, residual error, or convergence flags. Low-quality points are removed or corrected using correlation thresholds and neighborhood consistency checks. This stage is critical near specimen edges, in regions with glare, and in zones with strong gradients where decorrelation is likely.

In the following sections, each stage is reviewed in detail. Section 2.1.2 discusses speckle and imaging requirements; Sections 2.1.3–2.1.5 review subset design, shape functions, and correlation criteria; Sections 2.1.6–2.1.8 examine search strategies, interpolation, and optimization algorithms; and Sections 2.1.9–2.1.10 summarize reliability assessment and strain computation, providing the methodological basis for the multi-camera DIC developments in later chapters.

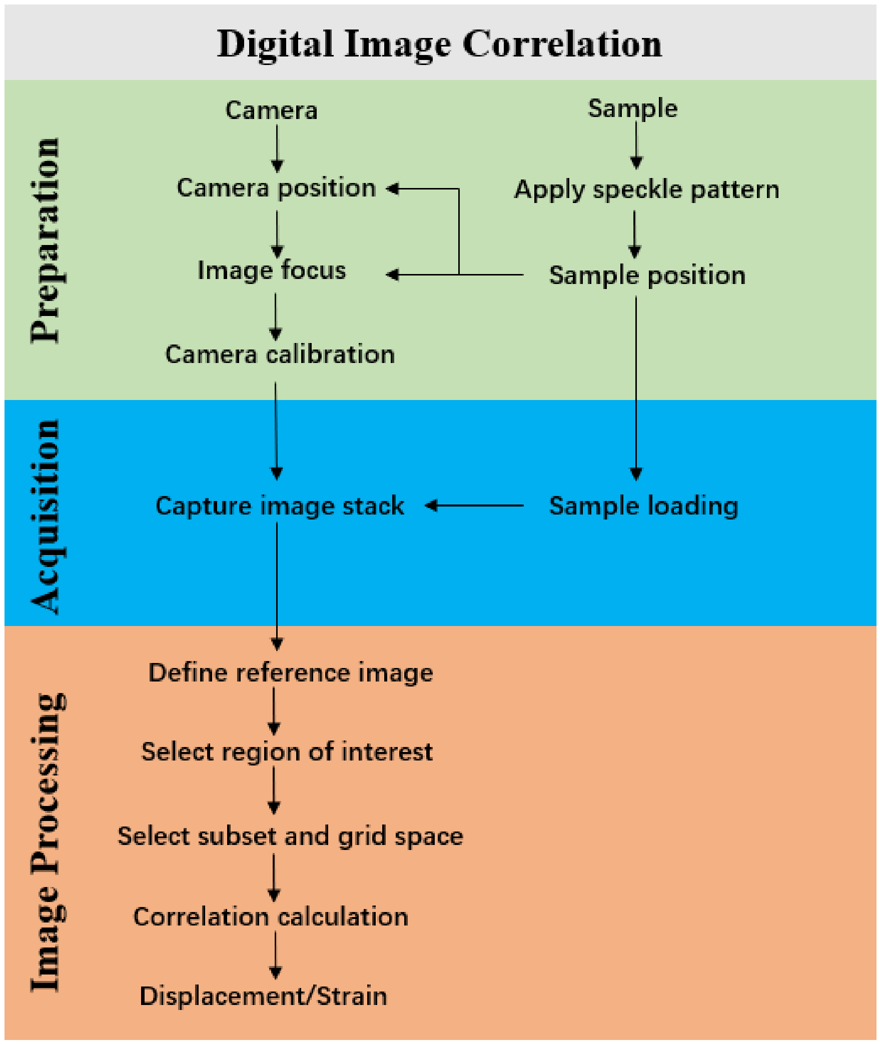

Figure 2.1 The workflow of DIC.

2.1.2 Speckle pattern requirements and image quality

The performance of DIC is fundamentally limited by the information content of the recorded images. Regardless of the correlation criterion or optimization scheme, reliable displacement estimation requires a surface texture that provides unique grayscale "signatures" within subsets and imaging conditions that preserve that texture with sufficient signal-to-noise ratio and minimal distortion [29-30]. Because sub-pixel interpolation and strain differentiation amplify deficiencies in the raw image data, speckle design and image quality control are commonly the most decisive steps in the overall measurement chain.

A speckle pattern serves as the carrier of spatial information for correlation. From an imaging perspective, DIC is sensitive to local grayscale gradients: subsets must contain enough random, non-repeating intensity variation so that the best match in the deformed image is unique. This motivates patterns that are spatially random, approximately isotropic, and uniformly distributed across the region of interest. Texture can be generated by painted speckles, laser speckle from coherent scattering and natural texture., as shown in figure 2.2. Painted speckles are typically stable over time, whereas laser speckle can provide very high contrast but may exhibit stronger decorrelation when the surface state or optical path changes. Speckle size must be considered together with subset size and image magnification. If speckle features are too small relative to pixel resolution, the texture becomes dominated by sensor noise and interpolation artifacts; if speckles are too large, each subset contains too few independent features and correlation becomes less unique. In practice, the goal is to ensure that each subset contains multiple well-resolved speckle features and sufficient intensity variation in both directions. This coupling leads to the classic trade-off between robustness and spatial resolution: larger subsets enhance uniqueness and noise averaging but reduce the ability to resolve sharp gradients, whereas smaller subsets improve spatial resolution but demand higher quality texture and produce higher noise.

Image exposure and grayscale stability have similarly strong impact on correlation quality. Saturation in highlights or shadows removes grayscale information and can bias correlation, while low contrast reduces gradient magnitude and lowers sub-pixel sensitivity. Although normalized criteria mitigate affine brightness changes (offset and scale), they cannot fully compensate for spatially varying illumination, specular glare, or non-linear intensity changes. For this reason, stable illumination, fixed camera settings and careful control of reflections are generally more effective than relying on algorithmic robustness alone. Optical quality and acquisition stability are also essential. Defocus acts as a low-pass filter that suppresses high-frequency content in the speckle field, increasing displacement noise; motion blur from vibration or insufficient shutter speed similarly smears speckle features and can introduce bias. Lens distortion influences the mapping between pixels and physical coordinates; in stereo configurations it additionally affects triangulation and coordinate unification.

In practice, it is beneficial to perform quick acceptance checks before correlation, such as verifying that the grayscale histogram avoids clipping, that focus and sharpness are consistent over the region of interest, and that short “no-load” image pairs yield a displacement/strain noise floor consistent with expectations. These checks help distinguish algorithmic issues from image-quality limitations and reduce the risk of propagating poor image quality into unreliable strain fields.

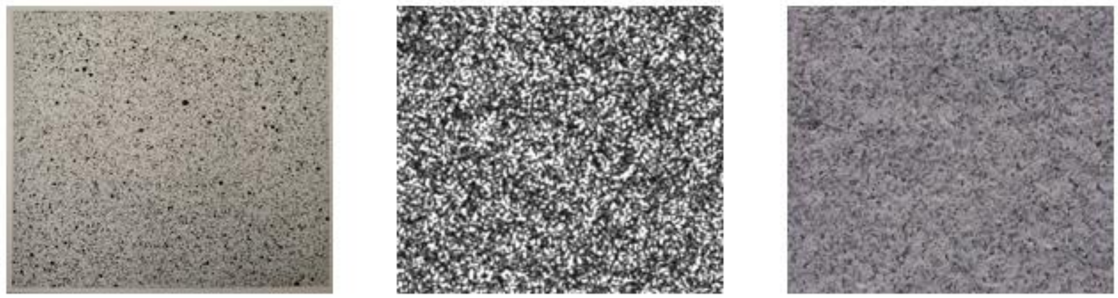

(a) (b) (c)

Figure 2.2 Speckle pattern: (a)Painted speckle; (b)Laser speckle; (c)Natural speckle (rock).

2.1.3 Subset size and grid spacing

A defining feature of DIC is that matching is performed on subsets (also referred to as correlation windows) rather than on individual pixels, as shown in figure 2.3. A subset provides a local neighborhood with sufficient grayscale information to yield a unique match in the deformed image, while remaining small enough that the deformation within the neighborhood can be described by a low-order kinematic model. The selection of subset size and grid spacing handling therefore directly governs the balance between spatial resolution, robustness, and computational cost. Let $\mathbf{x_0} = (x_0, y_0)$ denote a calculation point in the reference image $f(x, y)$. A square subset $\Omega(\mathbf{x_0})$ of half-size mmm is commonly defined as:

$$\Omega(\mathbf{x_0}) = \{(x, y) : x \in [x_0 - m, x_0 + m], y \in [y_0 - m, y_0 + m]\} \qquad (2.1)$$

corresponding to a (2m+1) ×(2m+1) pixel window. The DIC task at $\mathbf{x_0}$ is to find a parameter vector $\mathbf{p}$ (translation and possibly deformation terms) such that the mapped subset in the deformed image $g(x, y)$best matches the reference subset according to a chosen correlation criterion. A larger subset generally improves matching uniqueness and reduces sensitivity to sensor noise, illumination nonuniformity, and minor texture defects, since more independent grayscale features contribute to the objective function. However, large subsets reduce spatial resolution, smooth the measured fields, and can bias results in regions with steep gradients because the true deformation may vary significantly within the window. Conversely, smaller subsets improve spatial resolution and are better suited to capturing localized deformation, but their reduced information content makes them more sensitive to speckle quality and can increase noise level. A typical subset size contains 3-5 speckles.

DIC computes displacements at a set of grid points within a selected region. The grid spacing determines how densely the field is sampled. Smaller step sizes produce denser displacement/strain maps and allow more detailed visualization of gradients, but increase computational cost and yield heavily overlapping subsets. Overlap is not inherently problematic; it can improve smoothness and reduce random noise when gradients are moderate. However, it does not guarantee arbitrarily high spatial resolution because the effective resolution remains constrained by subset size and by whatever strain computation window is used later. Larger step sizes reduce cost but may undersample narrow localization zones and can miss the true peak strain location.

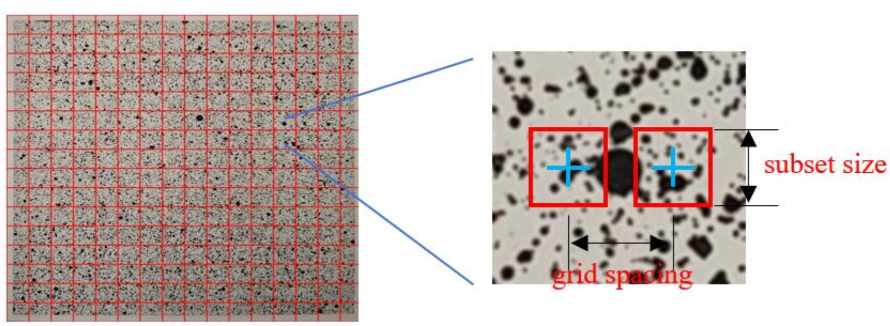

Figure 2.3 The concept of subset and grid spacing.

2.1.4 Shape function

After the subset and the computation grid are defined, the next step is to model how points inside the reference subset are mapped to their locations in the deformed image., as shown in figure 2.4. This mapping is commonly referred to as the subset deformation model or shape function. The role of the shape function is twofold: it (i) provides a kinematic description of local deformation within the subset, and (ii) determines the set of unknown parameters to be solved during correlation. Choosing an appropriate model order is therefore essential for both accuracy and numerical stability. A model that is too simple may be unable to represent the true local deformation, whereas an overly complex model may overfit noise, increase computational cost, and reduce convergence robustness.

Let $\mathbf{x} = (x, y)$ denote a point inside the reference subset and $\mathbf{x_0} = (x_0, y_0)$ the subset center. Define the local subset coordinates $\Delta x = x - x_0$and $\Delta y = y - y_0$. A general mapping can be written as:

$$\mathbf{x}' = \mathbf{W}\,(\mathbf{x}; \mathbf{p}) \tag{2.2}$$

where $\mathbf{x}' = (x', y')$ is the mapped coordinate in the deformed image and $\mathbf{p}$ is the vector of deformation parameters.

The simplest model is 0th-order model which assumes that the entire subset translates rigidly without internal distortion:

$$\begin{cases} x' = x + u \\ y' = y + v \end{cases} \tag{2.3}$$

where u and v are the in-plane displacements of the subset center. The corresponding parameter vector is $\mathbf{p} = [u, v]^T$.

This model is computationally efficient and can be adequate when deformation gradients over the subset are negligible, such as in nearly rigid-body motion, very small strain, or when extremely small subsets are used. However, under the larger deformation, internal subset distortion (stretching, shear, and rotation) becomes significant. In such cases, a translation-only model tends to reduce correlation quality and can bias displacement estimation because it forces the algorithm to explain true deformation with an incorrect motion model.

To capture the most common local deformation modes, DIC typically adopts a first-order (affine) model in which displacement varies linearly within the subset:

$$\begin{cases} x' = x + u + u_x \Delta x + u_y \Delta y \\ y' = y + v + v_x \Delta x + v_y \Delta \mathrm{y} \end{cases} \tag{2.4}$$

where u and v are the translations at the subset center and $\{ u_x, u_y, v_x, v_y\}$ are the local displacement gradients. The parameter vector becomes:

$$\mathbf{p} = [\mathrm{u}, \mathrm{v}, u_x, u_y, v_x, v_y]^T \tag{2.5}$$

The affine model can represent translation, in-plane rotation, normal strains, and shear strains within the subset. It is also directly connected to strain estimation: the displacement gradients solved at the subset level can be interpreted as local kinematic measures and can serve as inputs to later strain computation steps, although additional spatial smoothing is often required to control noise.

A second-order model includes quadratic terms to represent non-uniform displacement gradients within the subset:

$$\begin{cases} x' = x + u + u_x \Delta x + u_y \Delta y + \frac{1}{2} u_{xx} \Delta x^2 + u_{xy} \Delta x \Delta y + \frac{1}{2} u_{yy} \Delta y^2 \\ y' = y + v + v_x \Delta x + v_y \Delta y + \frac{1}{2} v_{xx} \Delta x^2 + v_{xy} \Delta x \Delta y + \frac{1}{2} v_{yy} \Delta y^2 \end{cases} \tag{2.6}$$

This model can better accommodate curvature and strong spatial variation of strain, and is therefore potentially beneficial in regions where deformation changes rapidly over a short length scale. However, the quadratic model introduces substantially more parameters, which increases the dimension of the optimization problem and typically requires higher-quality images and stronger texture information to remain stable. It is also more prone to overfitting noise and may yield less robust convergence, especially when the subset does not contain enough independent grayscale features to support the expanded parameter set.

In practical DIC, the model order should be selected based on the expected deformation complexity, the subset size, and the imaging quality. Increasing model order is not guaranteed to improve accuracy; instead, it trades bias (from under-modeling) against variance (from increased sensitivity to noise and reduced numerical stability). In most quasi-static sheet-metal tensile tests with adequate texture and moderate subset sizes, the first-order affine model provides reliable performance, while translation-only models are primarily useful for rigid-motion estimation or coarse initialization, and quadratic models are reserved for highly non-affine deformation scenarios.

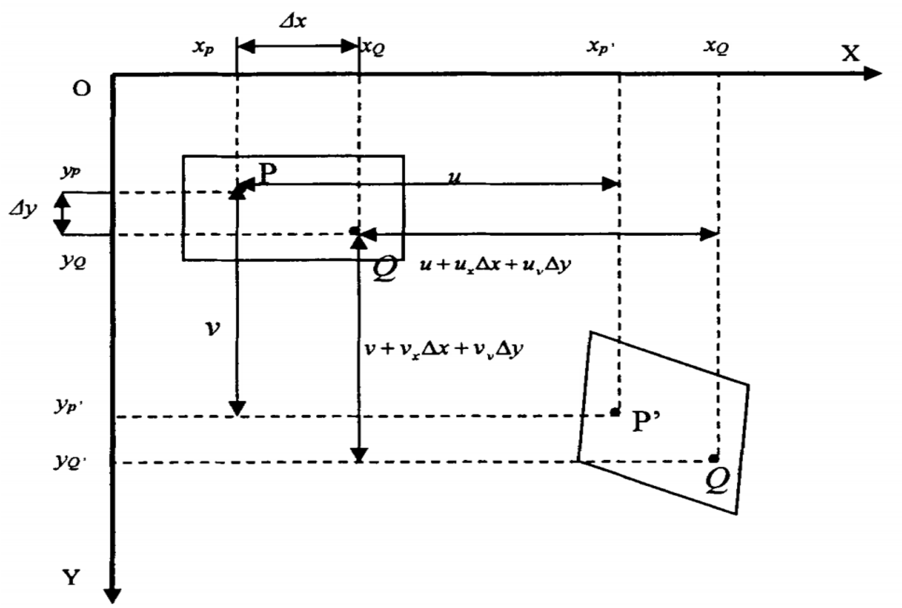

Figure 2.4 The schematic of deformation model in shape function.

2.1.5 Correlation criterion

With the subset defined and a shape function selected, the DIC problem can be written as an optimization task: determine the parameter vector **p** such that the reference subset $f(x)$ best matches the mapped deformed subset $g(\mathbf{W}(\mathbf{x};\mathbf{p}))$. This requires a quantitative measure of similarity between the two subsets, commonly referred to as the correlation criterion. Different criteria embody different assumptions on illumination stability and noise, and they directly affect robustness to brightness drift, glare, and local decorrelation. Let Ω denote the set of pixels inside the subset. For convenience, define discrete intensities:

$$f_i = f(x_i), \qquad g_i(\mathbf{p}) = g\big(\mathbf{W}(\mathbf{x}_i;\mathbf{p})\big), \qquad x_i \epsilon \Omega \tag{2.7}$$

and let $\bar{f}$, $\bar{g}$ and σ_f, σ_g denote the mean and standard deviation over Ω.

The most direct approach is to minimize an intensity difference measure. Two basic examples are the sum of absolute differences (SAD) and the sum of squared differences (SSD):

$$C_{SAD}(\mathbf{p}) = \sum_{i\epsilon\Omega}|f_i - g_i(\mathbf{p})| \tag{2.8}$$

$$C_{SSD}(\mathbf{p}) = \sum_{i\epsilon\Omega}|f_i - g_i(\mathbf{p})|^2 \tag{2.9}$$

These criteria are simple and computationally efficient, and SSD in particular aligns naturally with least-squares optimization. However, they implicitly assume that the grayscale values are preserved between images (brightness constancy). In practical experiments, this assumption is often violated by illumination fluctuations, heating-induced radiance changes, camera gain drift, or vignetting. As a result, SAD/SSD are typically most suitable when imaging conditions are tightly controlled and intensity variations are minimal.

To reduce sensitivity to illumination offsets and scaling, correlation-based criteria normalize intensities within the subset. The normalized cross-correlation (NCC) family evaluates the correlation between f_i and $g_i$and most common form used in DIC is the zero-mean normalized cross-correlation (ZNCC):

$$C_{ZNCC}(\mathbf{p}) = \frac{\sum_{i\epsilon\Omega}(f_i-\bar{f})(g_i(\mathbf{p})-\bar{g})}{\sqrt{\sum_{i\epsilon\Omega}(f_i-\bar{f})^2}\sqrt{\sum_{i\epsilon\Omega}(g_i(\mathbf{p})-\bar{g})^2}} \tag{2.10}$$

Because the mean is removed and the result is normalized by the subset standard deviations, ZNCC is invariant to affine changes in intensity of the form $g = af + b$ within the subset (with constants *a* and *b*). This makes it significantly more robust than SSD to moderate illumination changes.

An alternative, but closely related, formulation is the zero-mean normalized sum of squared differences (ZNSSD):

An alternative, but closely related, formulation is the zero-mean normalized sum of squared differences (ZNSSD):

$$C_{ZNSSD}(\mathbf{p}) = \sum_{i\epsilon\Omega}\left(\frac{f_i-\bar{f}}{\sigma_f} - \frac{g_i(\mathbf{p})-\bar{g}}{\sigma_g}\right)^2 \tag{2.11}$$

ZNSSD integrates normalization into a least-squares structure, which is convenient for Gauss–Newton-type solvers. ZNSSD and ZNCC are often regarded as nearly equivalent in practice because both remove mean intensity and normalize contrast, leading to similar robustness against brightness drift. The choice between them is frequently guided by computational convenience and solver implementation rather than by large performance differences.

2.1.6 Integer-pixel initialization and search strategies

The correlation criteria define an objective function $C(\mathbf{p})$ that is generally non-convex, especially when the displacement is large, the speckle texture is weak, or the subset undergoes significant distortion. As a result, DIC does not typically start directly from sub-pixel optimization. Instead, most implementations first obtain a reliable integer-pixel estimate of the subset motion, which serves as the initial guess for subsequent sub-pixel refinement. This section reviews commonly used initialization and search strategies, with emphasis on their roles in robustness, computational efficiency, and convergence radius.

Let the translation components of the parameter vector be (u, v). The integer-pixel stage aims to estimate (u, v) on the pixel grid, sometimes together with a simplified deformation model, by evaluating the chosen similarity measure across candidate shifts. The most direct approach is an exhaustive scan within a prescribed search window, evaluating the correlation criterion for each integer shift and selecting the best candidate. This strategy is simple and robust when the search window is sufficiently large, but its cost grows rapidly with window size and with the number of grid points. For dense grids or large displacements, purely exhaustive searches can become computationally prohibitive.

To address large motion efficiently, hierarchical strategies are widely adopted. A typical method is a coarse-to-fine (multi-resolution) pyramid, where images are progressively downsampled. Integer-pixel matching is performed at the coarsest level to estimate a large-scale displacement, and this estimate is then scaled and refined at the next level, continuing until the original resolution is reached. This approach increases the effective convergence basin and greatly reduces the computational burden relative to a large exhaustive window at full resolution. A related idea is nested searching: a coarse scan identifies a small neighborhood that contains the optimum, followed by a finer scan around that neighborhood. Both approaches aim to reduce candidate evaluations while retaining robust capture of large displacements.

Rather than searching blindly, many DIC workflows exploit the fact that displacement fields are typically smooth in space and vary gradually in time (except near discontinuities). Two common predictors are therefore used which are spatial predictor and temporal predictor. Spatial predictor: The displacement at a point is initialized using the already-solved neighboring. This is particularly effective when the motion field is smooth and when grid points are densely spaced. Temporal predictor: For image sequences, the displacement from the previous increment (or a linear extrapolation from multiple previous increments) is used as the initial guess. This approach is central to incremental DIC, where each frame is correlated relative to its immediate predecessor (or to a slowly updated reference), thereby keeping inter-frame displacements small.

Predictor-based initialization significantly improves efficiency and robustness by shrinking the required search window and reducing the probability of converging to an incorrect local optimum. However, it can be less effective in regions with abrupt deformation changes.

2.1.7 Sub-pixel interpolation

Integer-pixel initialization provides a discrete estimate of the subset motion, but the accuracy demanded in experimental mechanics typically requires sub-pixel displacement resolution. Sub-pixel refinement is possible because the grayscale intensity field can be viewed as a sampled version of an underlying continuous image; by interpolating the image intensity at non-integer coordinates, DIC can evaluate the correlation objective for fractional shifts and iteratively converge to a sub-pixel optimum.

Digital images are sampled on a discrete pixel grid, but DIC algorithms treat them as continuous functions when performing sub-pixel matching. The most frequently used interpolation schemes in DIC include bilinear interpolation, bicubic interpolation and spline interpolation. Bilinear interpolation uses the four nearest pixel values to approximate intensity. It is computationally efficient and easy to implement, but it provides only a piecewise linear approximation and may introduce bias when high-frequency texture content is important. Bicubic interpolation uses a larger neighborhood and yields smoother intensity and gradient estimates. It generally reduces interpolation bias relative to bilinear interpolation and is widely adopted as a default in many DIC implementations. Spline interpolants provide smooth higher-order approximations and can deliver accurate derivatives, which is helpful because many solvers use image gradients. The trade-off is increased computational cost and more complex implementation. In practice, the choice of interpolation is a balance between accuracy and speed. For high-quality speckle images with strong gradients, higher-order interpolation often improves robustness and reduces systematic error, particularly when the solver relies on image gradients.

2.1.8 Optimization algorithms for sub-pixel DIC

Once interpolation finished, sub-pixel DIC can be formulated as a parameter estimation problem: find the subset deformation parameters **p** that optimize a chosen similarity criterion. In most practical implementations, this is solved by iterative numerical optimization because the objective function is nonlinear in **p**. The choice of optimization algorithm affects convergence radius, robustness under noise and mild decorrelation, and computational efficiency—especially when dense grids and long image sequences are processed. A convenient way to describe DIC optimization is through a residual-based least-squares form. For a pixel $\mathbf{x}_i$ inside the subset Ω, define the mapped intensity in the deformed image as $g_i(\mathbf{p}) = g\big(\mathbf{W}(\mathbf{x}_i; \mathbf{p})\big)$, and define an intensity residual $r_i(\mathbf{p}) = f_i - g_i(\mathbf{p})$. The classical SSD objective is then:

$$J(\mathbf{p}) = \sum_{i \epsilon \Omega} r_i(\mathbf{p})^2 \tag{2.12}$$

and normalized criteria such as ZNSSD can be written in an analogous residual form after intensity normalization. In each case, iterative solvers update **p** by linearizing the residual function around the current estimate $\mathbf{p}^k$ and solving for an increment $\Delta\mathbf{p}$ such that

$\mathbf{p}^{k+1} = \mathbf{p}^k + \Delta\mathbf{p}$. Let $\mathbf{r}(\mathbf{p})$ denote the residual vector and $\mathbf{J}(\mathbf{p}) = \boldsymbol{\partial}\mathbf{r}/\boldsymbol{\partial}\,\mathbf{p}$ the Jacobian with respect to parameters. In nonlinear least squares, a widely used update is the Gauss–Newton step:

$$(\mathbf{J}^{\boldsymbol{T}}\mathbf{J})\Delta\mathbf{p} = -\mathbf{J}^{\boldsymbol{T}}\boldsymbol{r} \tag{2.13}$$

which approximates the Hessian by $\mathbf{J}^{\boldsymbol{T}}\mathbf{J}$ and avoids explicit second-order derivative calculations. Gauss–Newton methods are popular in DIC because they converge rapidly when the initial estimate is sufficiently close to the optimum (typically ensured by integer-pixel initialization) and because the least-squares structure matches common DIC objective functions.

2.2 Stereo three-dimensional DIC

While Section 2.1 reviewed DIC as a subset-based matching framework on image intensity fields, many experimental mechanics problems require three-dimensional (3D) surface kinematics, including out-of-plane motion and true surface strain. Stereo 3D DIC addresses this need by combining (i) spatial correspondence obtained by correlation on image pairs and (ii) geometric reconstruction based on camera calibration and triangulation. In essence, stereo DIC replaces the “pixel-to-pixel” viewpoint with a “ray-to-ray” viewpoint: each camera observation defines a viewing ray in 3D space, and the 3D point is reconstructed from the intersection of the rays. This section provides the methodological basis for later multi-camera model by introducing the camera model, calibration, stereo geometry, and 3D reconstruction workflow.

2.2.1 Camera model

Stereo 3D DIC relies on a quantitative relationship between a physical point on the specimen surface and its recorded pixel coordinates in each camera. This relationship is commonly derived from the pinhole camera model and then augmented by lens distortion, as shown in figure 2.5. The derivation naturally separates into two parts: a rigid-body transform that maps the world coordinates into the camera coordinate system (the extrinsic parameters), and a projection-plus-sampling model that maps camera coordinates onto the digital sensor (the intrinsic parameters).

Let a 3D point in the world coordinate system be $\mathbf{X} = [X, Y, Z]^T$, $\widetilde{\mathbf{X}} = [X, Y, Z]^T$. The camera coordinate system is defined with origin at the camera center, and axes (X_c, Y_c, Z_c) fixed to the camera such that Z_c is aligned with the optical axis. The mapping from world coordinates to camera coordinates is a rigid transformation:

$$\mathbf{X}_c = \mathbf{R}\mathbf{X} + \mathbf{t} \tag{2.14}$$

where **R** is a rotation matrix and **t** is a translation vector. In homogeneous form this becomes:

$$\widetilde{\mathbf{X}_c} = \begin{bmatrix} \mathbf{R} & \mathbf{t} \\ \mathbf{0}^T & 1 \end{bmatrix} \widetilde{\mathbf{X}} \tag{2.15}$$

These **R**, **t** are the extrinsic parameters: they encode the camera pose (orientation and position) relative to the world frame.

Under the ideal pinhole model, a 3D point in camera coordinates $\mathbf{X}_c = [X_c, Y_c, Z_c]^T$ projects to a point on the normalized image plane by perspective division:

$$\begin{cases} x_n = \frac{X_c}{Z_c} \\ y_n = \frac{Y_c}{Z_c} \end{cases} \tag{2.16}$$

These (x_n, y_n) are normalized image coordinates measured in metric units on an image plane whose scale is not yet tied to pixels. To connect this projection to the physical sensor, introduce the focal length f and a sensor coordinate system (x_s, y_s) on the imaging plane:

$$\begin{cases} x_s = f x_n = f \frac{X_c}{Z_c} \\ y_s = f y_n = f \frac{Y_c}{Z_c} \end{cases} \tag{2.17}$$

A digital camera records these coordinates on a discrete pixel grid. Let the pixel sizes along the sensor axes be p_x and p_y. Converting from metric sensor coordinates to pixel coordinates gives:

$$\begin{cases} u = \frac{x_s}{p_s} + c_x \\ v = \frac{y_s}{p_y} + c_y \end{cases} \tag{2.18}$$

where (c_x, c_y) is the principal point. Substituting x_s, y_s yields:

$$\begin{cases} u = (\frac{f}{p_x}) \frac{X_c}{Z_c} + c_x \\ v = (\frac{f}{p_y}) \frac{Y_c}{Z_c} + c_y \end{cases} \tag{2.19}$$

Defining $f_x = f/p_x$ and $f_y = f/p_y$, the equations become:

$$\begin{cases} u = f_x \frac{X_c}{Z_c} + c_x \\ v = f_y \frac{Y_c}{Z_c} + c_y \end{cases} \tag{2.20}$$

If the sensor axes are not perfectly orthogonal (rare in modern cameras but included for completeness), a skew term γ can be introduced, leading to the standard intrinsic matrix:

$$\mathbf{K} = \begin{bmatrix} f_x & \gamma & c_x \\ 0 & f_y & c_y \\ 0 & 0 & 1 \end{bmatrix} \tag{2.21}$$

These quantities $(f_x, f_y, c_x, c_{y,}\gamma)$are the intrinsic parameters, describing how the camera maps rays into pixel coordinates.

Combining the extrinsic rigid transform with the intrinsic mapping produces the familiar homogeneous projection equation. Start by writing the camera-frame point in homogeneous coordinates:

$$\widetilde{\mathbf{X}_c} = [\mathbf{R}\ \mathbf{t}]\widetilde{\mathbf{X}} \tag{2.22}$$

Perspective projection can be compactly expressed by introducing a scale factor s:

$$s\tilde{\mathbf{x}} = \mathbf{K}[\mathbf{R}\ \mathbf{t}]\widetilde{\mathbf{X}} \tag{2.23}$$

where $\tilde{\mathbf{x}} = [u, v, 1]^T$. Defining the camera projection matrix $\mathbf{P} = \mathbf{K}[\mathbf{R}|\mathbf{t}]$, the model becomes $s\tilde{\mathbf{x}} = \mathbf{P}\widetilde{\mathbf{X}}$. This equation is the core of stereo geometry: for each camera, it maps a 3D point in the world frame to a 2D pixel prediction. Stereo 3D DIC uses this model in reverse—given pixel observations from multiple calibrated cameras, it reconstructs $\mathbf{X}$ by triangulation.

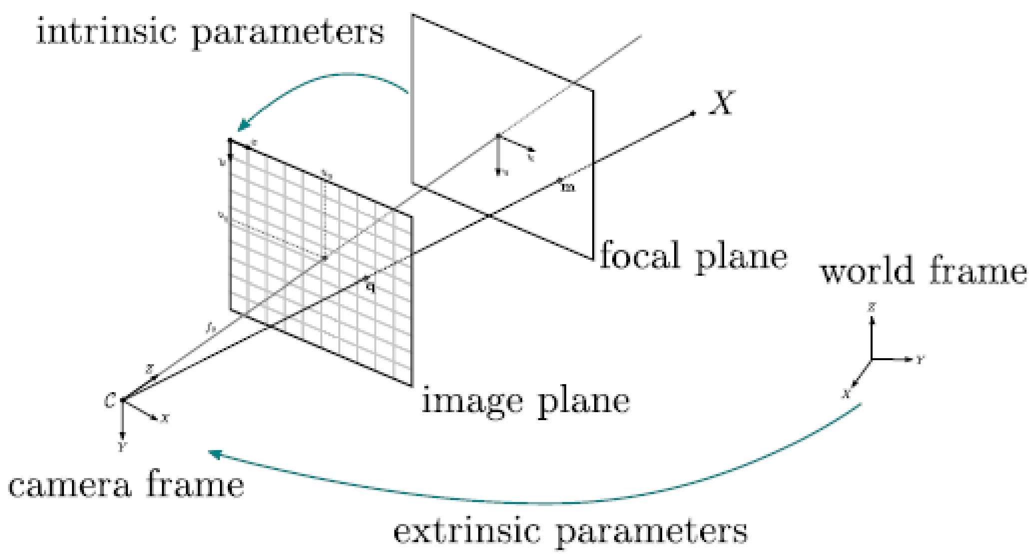

Figure 2.5 The schematic of pinhole camera model.

<u>2.2.2 Lens distortion</u>

The pinhole model assumes an ideal central projection in which straight rays project to straight lines on the image plane. Real lenses introduce systematic deviations from this ideal mapping, commonly grouped into radial distortion and tangential distortion. In stereo 3D DIC, distortion errors are especially important because depth is inferred from small differences between two camera observations; spatially varying distortion can therefore translate into spatially varying depth bias and inconsistent surface curvature in the reconstructed geometry. For this reason, distortion is explicitly modeled and corrected as part of the camera model used for reconstruction. A schematic demonstration of two typical lens distortion is illustrated in figure 2.6.

Distortion is conveniently expressed in the normalized image plane, i.e., after transforming a world point $\mathbf{X}$ into camera coordinates $\mathbf{X}_c = [X_c, Y_c, Z_c]^T$ and applying perspective division, let $r^2 = x_n^2 + y_n^2$. A widely used radial distortion model maps (x_n, y_n) to (x_r, y_r) by:

$$\begin{cases} x_r = x_n(1 + k_1 r^2 + k_2 r^4 + k_3 r^6) \\ y_r = y_n(1 + k_1 r^2 + k_2 r^4 + k_3 r^6) \end{cases} \tag{2.24}$$

where k_1, k_2, k_3 are radial distortion coefficients. Tangential distortion, which accounts for lens decentering and misalignment, is then incorporated as:

$$\begin{cases} x_d = x_r + 2p_1 x_n y_n + p_2(r^2 + 2x_n^2) \\ y_d = y_r + p_1(r^2 + 2y_n^2) + 2p_2 x_n y_n \end{cases} \tag{2.25}$$

where p_1, p_2 are tangential distortion coefficients. The distorted normalized coordinates (x_d, y_d) are converted to pixel coordinates through the intrinsic parameters:

$$\begin{cases} u = f_x x_d + \gamma y_d + c_x \\ v = f_y y_d + c_y \end{cases} \tag{2.26}$$

This completes the forward model from a 3D point $\mathbf{X}$ to its distorted pixel projection (u, v), and it is the model minimized during calibration through reprojection error.

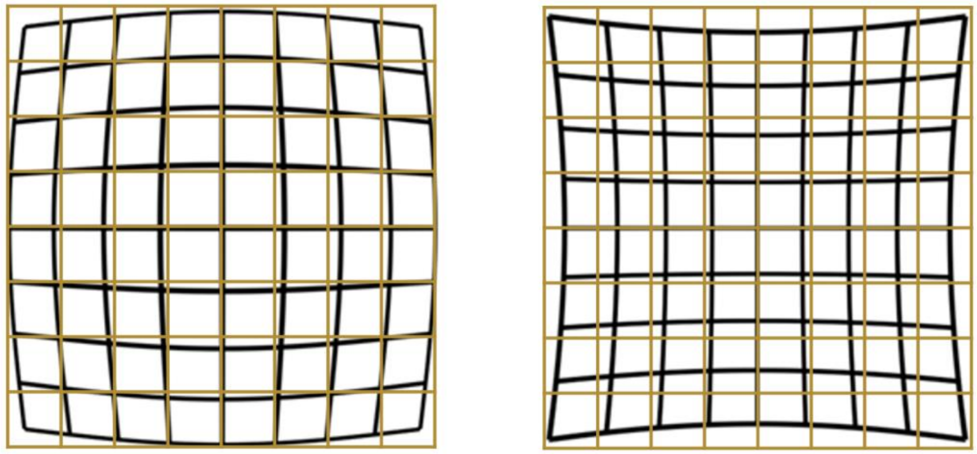

Figure 2.6 The schematic of two types of lens distortion: (a) Barrel distortion; (b) Pincushion distortion.

2.2.3 Camera calibration

Calibration is the process of estimating the parameter set $\Theta = \{f_x, f_y, c_x, c_y, \gamma, k_1, k_2, k_3, p_1, p_2, \mathbf{R}_k, \mathbf{t}_k\}$, given a set of known calibration target points and their measured pixel coordinates. In practical DIC systems, the calibration target is typically a planar checkerboard or dot grid, as shown in figure 2.7. For each calibration image k, a set of target points $\mathbf{X}_j$(expressed in the target coordinate system) are detected in the image as pixel coordinates $\mathbf{x}_{j,k}^{meas} = [u_{j,k}, v_{j,k}]^T$. The calibration parameters are then obtained by minimizing the total reprojection error:

$$\min_{\Theta} \sum_{k=1}^{N_{img}} \sum_{j=1}^{N_{pt}} \left\| \mathbf{x}_{j,k}^{meas} - \mathbf{x}_{j,k}^{proj}(\Theta, \mathbf{X}_j) \right\|^2 \tag{2.27}$$

where $\mathbf{x}_{j,k}^{proj}$ is the model-predicted pixel coordinate computed using the projection in Section 2.2.1 plus the distortion mapping above. Because this is a nonlinear least-squares problem, solvers commonly apply iterative optimization to refine parameters until the reprojection residuals are minimized.

A key practical requirement for reliable estimation of distortion and intrinsics is that calibration images must cover the full range of radii r over the sensor, meaning that detected points should populate both the center and edges of the field of view. If calibration poses only occupy a small central region, distortion parameters can become weakly constrained and still yield deceptively low reprojection error near the center while producing bias at the periphery. In addition, the calibration poses should span a depth range that is representative of the measurement volume in experiments; although planar targets provide 2D point sets, varying the target's pose and distance supplies the geometric diversity needed to constrain extrinsic parameters robustly.

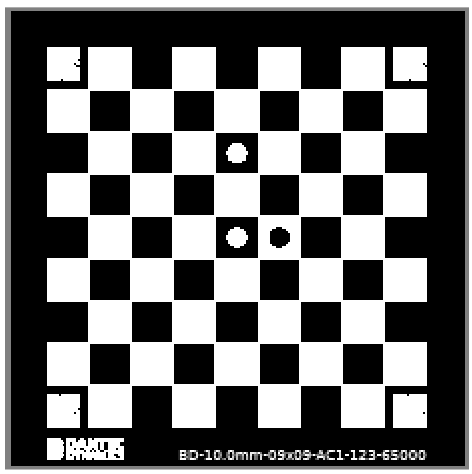

Figure 2.7 Checkboard calibraiton patttern.

2.2.4 Epipolar geometry

With the camera model, distortion treatment, and calibration established, stereo reconstruction reduces to one core requirement: the same physical surface point must be identified in both camera images so that two viewing rays can be formed for triangulation, as shown in figure 2.8. This mapping between a point observed in the left image and its counterpart in the right image is the stereo correspondence problem. In stereo DIC, correspondence is strongly assisted by calibration through epipolar geometry, which provides a deterministic geometric constraint that narrows the search space and improves robustness.

Consider a world point **X** that projects to homogeneous pixel coordinates $\tilde{\mathbf{x}}_L = [u_L, v_L, 1]^T$ and $\tilde{\mathbf{x}}_R = [u_R, v_R, 1]^T$ in the left and right cameras, respectively. For a calibrated stereo pair, these image points satisfy the epipolar constraint:

$$\tilde{\mathbf{x}}_R^T \mathbf{F} \tilde{\mathbf{x}}_L = 0 \tag{2.28}$$

where **F** is the fundamental matrix, determined by the relative pose between the two cameras and their intrinsics. Geometrically, $\tilde{\mathbf{x}}_L$ defines a 3D ray emitted from the left camera center; together with the right camera center, this ray defines an epipolar plane that intersects the right image plane along a line. That intersection is the epipolar line on which the corresponding point $\tilde{\mathbf{x}}_R$ must lie. Therefore, for any candidate point in one image, the search for its correspondence in the other image is reduced from a 2D region to a 1D curve.

It is often useful to express epipolar geometry in normalized coordinates. Let $\tilde{\mathbf{x}}_L^n = \mathbf{K}_L^{-1} \tilde{\mathbf{x}}_L$ and $\tilde{\mathbf{x}}_R^n = \mathbf{K}_R^{-1} \tilde{\mathbf{x}}_R$ be undistorted normalized image points. The constraint can then be written using the essential matrix **E**:

$$(\tilde{\mathbf{x}}_R^n)^T \mathbf{E} \tilde{\mathbf{x}}_L^n = 0, \mathbf{E} = [\mathbf{t}]_\times \mathbf{R} \tag{2.29}$$

where **R** and **t** describe the relative rotation and translation from the left camera to the right camera, and $[\mathbf{t}]_\times$ is skew-symmetric matrix representing the cross product with **t**. The relationship between **E** and **F** is:

$$\mathbf{F} = \mathbf{K}_R^{-T} \mathbf{E} \mathbf{K}_L^{-1} \tag{2.30}$$

which makes explicit how intrinsics and extrinsics jointly determine epipolar lines. In DIC practice, whether the epipolar constraint is implemented via **F** in pixel space or via **E** in normalized space depends on software conventions, but the underlying role is identical: restrict and validate correspondence.

A further practical enhancement is stereo rectification, which applies homographies to the two images so that epipolar lines become (approximately) horizontal and aligned, simplifying correspondence to a 1D search along rows. Rectification is not required—one can match directly along general epipolar lines—but it provides a convenient computational and visualization advantage, and it is widely used in stereo vision.

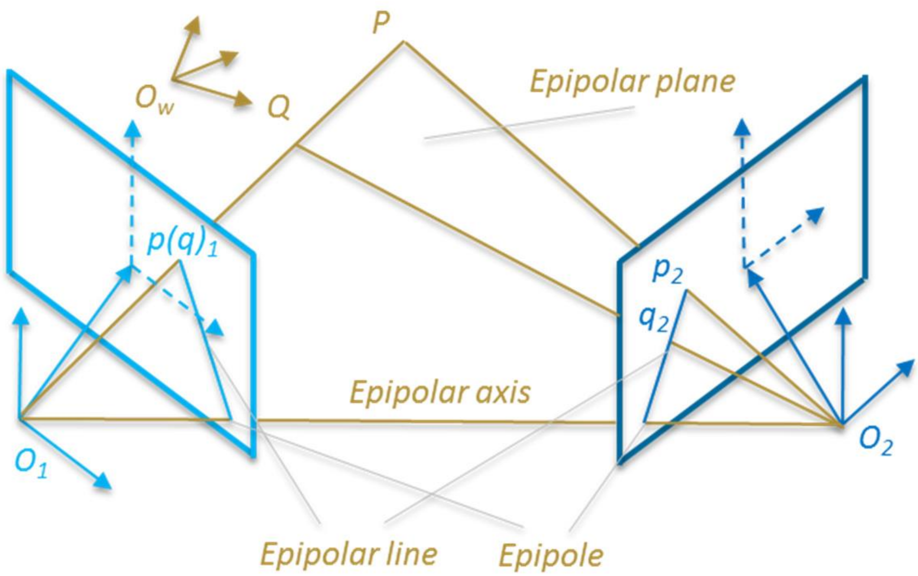

Figure 2.8 The schematic of epipolar geometry.

2.2.5 Triangulation and 3D reconstruction

Once stereo correspondence is established under the epipolar constraint, the 3D position of a surface point can be reconstructed from its two image observations through triangulation. Conceptually, each pixel observation defines a viewing ray that originates from the camera center and passes through the image plane. Triangulation estimates the 3D point as the best intersection of the two rays, with calibration providing the ray directions and the camera poses. Because pixel-level noise and calibration residuals prevent perfect intersection, practical triangulation solves a best-fit problem rather than a strict geometric intersection.

Let the calibrated projection matrices of the left and right cameras be $\mathbf{P}_L = \mathbf{K}_L[\mathbf{R}_L|\mathbf{t}_L]$ and $\mathbf{P}_R = \mathbf{K}_R[\mathbf{R}_R|\mathbf{t}_R]$, the corresponding pixel observations be $\tilde{\mathbf{x}}_L = [u_L, v_L, 1]^T$ and $\tilde{\mathbf{x}}_R = [u_R, v_R, 1]^T$. In homogeneous coordinates, ideal projection satisfies:

$$\tilde{\mathbf{x}} \sim \mathbf{P}\widetilde{\mathbf{X}} \tag{2.31}$$

where $\widetilde{\mathbf{X}} = [X, Y, Z, 1]^T$ and $\sim$ denotes equality up to scale. A standard way to derive a linear triangulation system is to use the fact that $\tilde{\mathbf{x}}$ must be collinear with $\mathbf{P}\widetilde{\mathbf{X}}$, which implies:

$$\tilde{\mathbf{x}} \times \left(\mathbf{P}\widetilde{\mathbf{X}}\right) = 0 \tag{2.32}$$

Expanding the cross product yields two independent linear equations per view. Writing **P** by rows as $\mathbf{P} = \begin{bmatrix} \mathbf{p}_1^T \\ \mathbf{p}_2^T \\ \mathbf{p}_3^T \end{bmatrix}$, the constraints for one camera can be expressed as:

$$\begin{cases} u\mathbf{p}_3^T\widetilde{\mathbf{X}} - \mathbf{p}_1^T\widetilde{\mathbf{X}} = 0 \\ v\mathbf{p}_3^T\widetilde{\mathbf{X}} - \mathbf{p}_1^T\widetilde{\mathbf{X}} = 0 \end{cases} \tag{2.33}$$

Applying these equations to both cameras produces a homogeneous linear system $\mathbf{A}\widetilde{\mathbf{X}} = \mathbf{0}$, with $\mathbf{A} \in \mathbb{R}^{4\times4}$ assembled from the two equations per camera. The 3D point $\widetilde{\mathbf{X}}$ is then obtained (up to scale) as the right singular vector of **A** corresponding to the smallest singular value, followed by dehomogenization to recover $[X, Y, Z]^T$. This linear method is efficient and is commonly used to initialize 3D reconstruction.

Although linear triangulation is widely used, it is not optimal under image noise because it does not directly minimize reprojection error. A refined estimate is obtained by nonlinear triangulation, which minimizes the sum of squared reprojection errors in both cameras:

$$\min_{\mathbf{X}} \|\mathbf{x}_L - \pi(\mathbf{P}_L, \mathbf{X})\|^2 + \|\mathbf{x}_R - \pi(\mathbf{P}_R, \mathbf{X})\|^2 \tag{2.34}$$

where $\pi(\cdot)$ denotes the projection function. In practice, linear triangulation provides a good initial guess, and the nonlinear refinement improves accuracy. In stereo DIC, triangulation is applied repeatedly to reconstruct the specimen surface at the reference state and at subsequent deformed states. A common workflow reconstructs the reference 3D surface from the stereo pair at t_0, then tracks image-plane motion over time in each view using 2D correlation, and finally triangulates the paired pixel coordinates at each time step to obtain $\mathbf{X}(t)$. The 3D displacement field is computed as:

$$\mathbf{U}(\mathbf{X}) = \mathbf{X}_{def} - \mathbf{X}_{ref} = \begin{bmatrix} U \\ V \\ W \end{bmatrix} \tag{2.35}$$

where *U*, *V*, *W* denote in-plane and out-out-plane displacement component. With all quantities expressed in a unified world coordinate system defined by calibration. Because the reconstructed surface is discrete and strain requires differentiation, later strain computation typically employs local fitting or smoothing over a neighborhood; nevertheless, the fidelity of **U** depends directly on the accuracy of correspondence and triangulation.

2.3 Multi-camera (double-side) DIC

2.3.1 Motivation and concept of a double-side measurement

Conventional stereo 3D-DIC reconstructs the 3D kinematics of one observed surface, which is sufficient for many applications but cannot directly provide through-thickness information for thin sheet specimens. In sheet-metal deformation, thickness change is often a key output because it is closely tied to local instability and failure, yet a single-surface measurement only offers indirect routes to infer thickness evolution. This limitation has motivated a series of alternative thickness-strain measurement approaches, including intermittent thickness readings using calipers, attaching miniature sensors on the specimen edge, or imaging the side surface and approximating thickness strain from the minor strain measured on that edge. However, such methods are inherently restricted in spatial coverage and, for sheet metals, side-surface imaging is also resolution-limited because the thickness dimension is much smaller than the in-plane dimensions, making whole-field thickness strain difficult to obtain reliably.

A seemingly straightforward workaround is to place two independent stereo DIC systems on the front and back sides. In practice, the major difficulty is that the two reconstructed datasets are not automatically expressed in a common coordinate system, so point-wise combination for thickness evaluation becomes cumbersome and error-prone. To address this, a double-side DIC treats the setup as one integrated system: two stereo subsystems observe the front and back surfaces, and the information from the two subsystems is explicitly linked through a unified calibration strategy. A typical implementation uses four cameras, with cameras 1–2 forming a stereo pair for the front surface and cameras 3–4 forming a stereo pair for the back surface. Each pair performs standard stereo reconstruction on its side, but the overall system is calibrated and constrained so that the two reconstructions can be expressed in a unified world coordinate system, enabling direct thickness-related evaluation. Figure 2.9 is the schematic of the double-side DIC system.

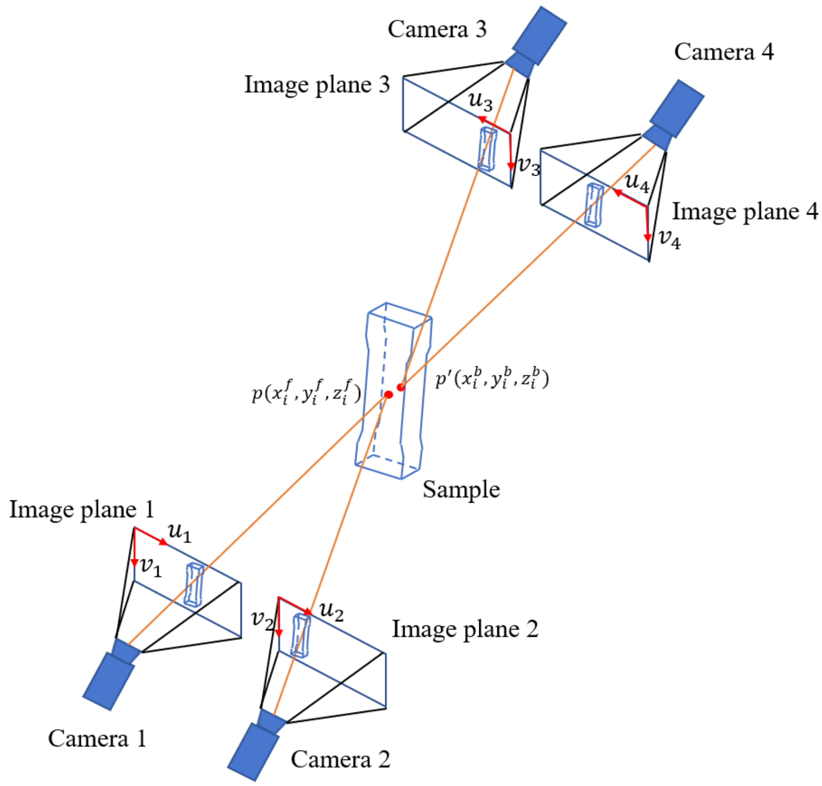

Figure 2.9 The schematic of the double-side DIC system.

2.3.2 Unified calibration and coordinate unification

A double-side DIC system can be modeled as two stereo-vision subsystems: a front subsystem and a back subsystem. Each subsystem is capable of performing a conventional stereo reconstruction on its own observed surface, but the key requirement for thickness-related evaluation is that the two reconstructions must be expressed in one common coordinate system rather than two unrelated local frames. For each camera *k*, the homogeneous sensor coordinate $\tilde{\mathbf{x}}_k' = [x_{s,k}', y_{s,k}', 1]^T$ can be expressed as a distortion operation applied to the ideal projection of a 3D point:

$$\tilde{\mathbf{x}}'_k = \mathbf{D}_k \tilde{\mathbf{x}}_k = \mathbf{D}_k \mathbf{P}_k \tilde{\mathbf{X}} \tag{2.36}$$

where $\mathbf{D}_k$ represents the distortion (correction) mapping and $\mathbf{P}_k$ is the camera projection matrix.

Because the system contains two stereo subsystems, the reconstructed 3D points are naturally referenced to two world coordinate systems: one associated with the front subsystem $\tilde{\mathbf{X}}_f = \left[X_f, Y_f, Z_f, 1\right]^T$ and one associated with the back subsystem $\tilde{\mathbf{X}}_b = [X_b, Y_b, Z_b, 1]^T$. To enable thickness evaluation, the next step is to connect these two world systems into a single global system. Define the global frame to coincide with one subsystem (e.g., the front-side world system), and then transform the back-side coordinates into that global frame through a homogeneous rigid transform T:

$$\tilde{\mathbf{X}}_f = \mathbf{T}\tilde{\mathbf{X}}_b \tag{2.37}$$

Once T is known, any reconstructed point (and displacement) on the back surface can be expressed in the same global coordinates as the front surface. A practical calibration challenge is that a standard calibration target printed on only one side cannot be viewed by front and back subsystems simultaneously, making it impossible to calibrate all four cameras at the same time using the conventional single-sided target. To address this, a double-side calibration board is used: cameras 1–2 observe the front pattern and cameras 3–4 observe the back pattern, while the two sides are manufactured to be parallel and their pattern is aligned well, as shown in figure 2.10. Importantly, the board thickness provides the separation parameter that enters the front–back transformation T so that the calibration procedure determines both (i) each camera's intrinsic/extrinsic parameters and (ii) the relation between the two world coordinate systems required for dual-side reconstruction.

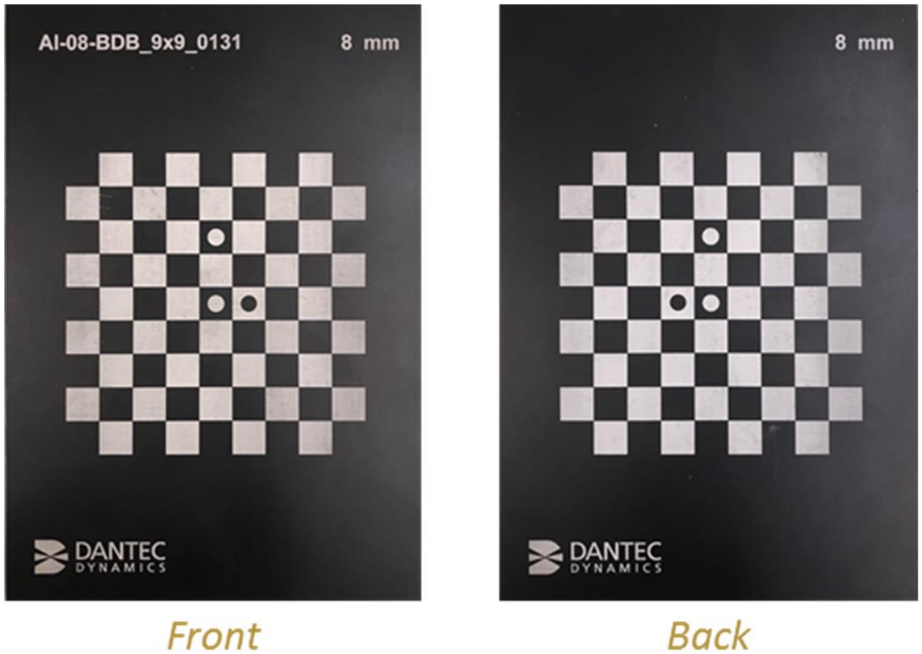

Figure 2.10 Double-side calibration board.

2.3.3 Thickness and thickness-strain evaluation

With the unified calibration described in Section 2.3.2, the front and back surfaces can be reconstructed independently by their respective stereo pairs and then expressed in the same global coordinate system. Let $\mathbf{X}_{r,f}$ and $\mathbf{X}_{r,b}$ denote the reconstructed 3D positions of a corresponding material location on the front and back surfaces in the reference state, and let $\mathbf{X}_{d,f}$ and $\mathbf{X}_{d,b}$ denote the corresponding 3D positions at a deformed state. Let $\mathbf{n}_0$be a unit normal vector representing the local through-thickness direction in the reference configuration. The initial thickness and current thickness at that location can be defined as:

$$\begin{cases} t_0 = (\mathbf{X}_{r,f} - \mathbf{X}_{r,b}) \cdot \mathbf{n}_0 \\ t = (\mathbf{X}_{d,f} - \mathbf{X}_{d,b}) \cdot \mathbf{n}_0 \end{cases} \tag{2.38}$$

Thickness change then follows directly as $\Delta t = t - t_0$. For strain reporting, an engineering thickness strain can be written as:

$$e_t = \frac{t - t_0}{t_0} \tag{2.39}$$

While a logarithmic (true) thickness strain is often preferred when deformation is large,

$$\varepsilon_t = \ln\left(\frac{t}{t_0}\right) \tag{2.40}$$

These expressions are fully geometric and remain valid as long as front–back correspondence is defined consistently.

2.3.4 Thickness-strain accuracy optimization

Although the dual-side framework enables direct thickness and thickness-strain measurement, the thickness channel is typically more sensitive to error than in-plane displacement because it relies on stereo depth from two independent reconstructions and then forms a difference between them. As a result, thickness strain can exhibit noticeable noise or bias if the two surfaces are not reconstructed with consistent accuracy, if the front–back transformation is imperfect, or if local outliers are not filtered. For sheet metals, the thickness is typically on the order of $\sim$1 mm, which makes through-thickness measurement challenging in a dual-side reconstruction framework. Because thickness strain effectively reflects the first-order variation of the thickness signal over deformation, so small fluctuations or bias in the reconstructed thickness field can translate into disproportionately large variations.

In this dissertation, following the strategy adopted in our multi-camera DIC studies, a random sample consensus (RANSAC) robust fitting procedure is applied to the thickness-related field to (i) identify and reject high-noise outliers and (ii) reconstruct a spatially continuous field by model-based interpolation at the rejected locations. This algorithm based on iterative method was proposed by Fischler to solve the problem of inaccurate solutions when using the least squares model on sample data with a large proportion of outliers. The basic algorithm is summarized as follows:

1. Randomly select several points in the thickness-strain data to calculate the polynomial thickness-strain history model.
2. Set a preset tolerance value ε and calculate the number of data points that match the mathematical model in step 1.
3. If the proportion of data points that meet the mathematical model in Step 2 exceeds the preset threshold τ, recalculate the thickness-strain history model to use these inliers and terminate the algorithm.
4. Otherwise, repeat steps 1 to 3 K times.

To ensure that the probability *p* of at least one set of random samples not including outliers is greater than 0.99, the number of iterations *K* should be large enough. Assuming that the probability that the data is selected as an inlier is *a*, then *b* = 1-*a* is the probability of observing an outlier. The required number of iterations of the minimum number of points, denoted *k*, where

$$1 - p = (1 - a^k)^K \tag{2.41}$$

$$K = \frac{\log(1-p)}{\log(1-(1-b)^k)} \tag{2.42}$$

Taking the tensile test of DP980 steel as an example, Figure 2.11 shows its thickness strain history curve. It can be seen that the thickness strain curve contains a large number of noisy outlier data points. Directly using the least squares method for fitting will be severely affected by these outliers, resulting in a large deviation in the fitting result. Figure 2.12 shows the result after using the RANSAC algorithm to remove outliers and then performing least squares fitting. Clearly, the result is more accurate than the direct least squares fitting. This strategy is particularly effective for thin sheet metals, where the small baseline thickness amplifies raw thickness measurement noise when converted to thickness strain.

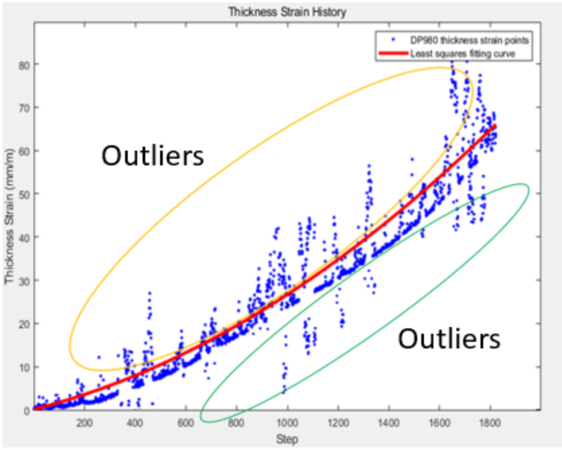

Figure 2.11 Thickness strain history with noise.

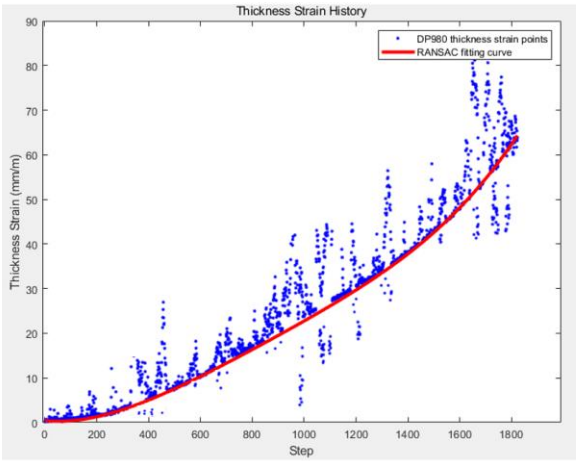

Figure 2.12 Thickness strain history after RANSAC fitting.

CHAPTER THREE

DIRECT R-VALUE MEASUREMENT

3.1 Introduction to R-value

Plastic anisotropy plays a central role in the formability and springback behaviour of sheet metals, and is therefore a key input in constitutive models and forming simulations. Among the various measures of anisotropy, the Lankford coefficient (or R-value) is one of the most widely used quantities in industrial practice [31-33]. For a uniaxial tensile test along a given loading direction, the R-value is conventionally defined as the ratio between the width strain and the thickness strain in the plastic regime, evaluated at a prescribed plastic strain level [34-36]. Materials with higher R-values generally exhibit better resistance to thinning and improved drawability, which is particularly important for automotive sheet forming and other applications involving complex stamping operations. In standard testing practice, the R-value is rarely measured from thickness directly. Instead, it is typically inferred from the in-plane strains under the assumption of plastic incompressibility (or volume constancy). For a uniaxial tensile state, this leads to a relation:

$$\varepsilon_t = -(\varepsilon_l + \varepsilon_w) \tag{3.1}$$

where ε_t is the thickness strain, and ε_l, ε_w are longitudinal and width strains, respectively. The R-value is then expressed as:

$$R = \frac{\varepsilon_w}{\varepsilon_t} = -\frac{\varepsilon_w}{\varepsilon_l + \varepsilon_w} \tag{3.2}$$

which can be determined from measurements of ε_l and ε_w alone. This indirect formulation is convenient because it avoids direct thickness measurement, but it also embeds the volume-constancy assumption, and its accuracy may degrade when the stress state deviates from ideal uniaxial tension or when localized deformation develops.

Several factors can cause the conventional R-value determination to deviate from the actual material response. First, the plastic incompressibility assumption is only approximate at the macroscopic scale, particularly in the presence of non-uniform deformation, texture evolution, damage, or microvoid growth. Second, once necking initiates, the local strain state becomes strongly heterogeneous, and the strain field in the gauge section may deviate significantly from the uniform uniaxial state assumed in the standard derivation. Third, specimen geometry, slight misalignment, and friction can introduce bending and non-uniformity across the thickness, which affect the relation between in-plane strains and thickness change. When combined, these effects can bias the inferred ε_t and therefore the estimated R-value, especially if only a single surface is observed.

Digital image correlation (DIC) has greatly improved the characterization of in-plane strain fields in sheet tensile tests by providing full-field, non-contact measurements. However, a conventional stereo DIC system still observes only one surface, so thickness strain must be obtained indirectly, either from the volume-constancy relation or from side-view imaging with limited spatial coverage and resolution. As discussed in Chapter 2, the dual-side multi-camera DIC configuration overcomes this limitation by reconstructing the front and back surfaces simultaneously in a unified coordinate system and by enabling direct evaluation of local thickness and thickness strain. This capability opens the door to a direct experimental determination of the R-value in which ε_t is no longer inferred from in-plane data, but measured from the front–back separation itself.

The objective of this chapter is to exploit the double-side DIC framework developed in Chapter 2 to establish and validate a direct R-value measurement method for sheet metals. In this approach, the longitudinal and width strains are obtained from the full-field in-plane components on one or both surfaces, while the thickness strain is computed from the dual-side reconstruction of thickness, using the front–back separation along a reference normal direction. The resulting R-value is therefore defined directly in terms of a measured thickness strain rather than through the volume-constancy approximation. This enables a quantitative comparison between conventional and direct R-value, provides insight into the validity of the incompressibility assumption over the measured strain range, and offers a more geometry-aware characterization of plastic anisotropy in materials where thickness change and localization behaviour are critical.

3.2 Experiment results and discussion

The experimental system is shown in figure 3.1. Four GigE cameras (maximum resolution 2752x2200) were used to form two independent DIC binocular measurement systems. One DIC system was placed in front of the test sample, while the other DIC system was placed behind the test sample. Two pairs of 50 mm fixed lenses were used to achieve a 300 mm×250 mm field of view. The spatial resolution is 0.1mm/pixel. Two powerful LED lights provide sufficient illumination for the front and back DIC measurement systems. A 50kN MTS tensile test machine was used to do the tensile test, and a 1 mm thick dog-bone shape sample made out of DP980 sheet metal was prepared for the test. The tensile speed was set at 3mm/min. The slow strain rate used for the test enabled more images to be taken before the sample cracked, thus providing more data to analyze. Figure 3.2 is a schematic diagram of this sample. Current limitations with this system include the cost of the cameras used for the DIC systems and the large amount of space required to accommodate the front and rear camera groups.

The double-side DIC system was calibrated following the unified procedure described in Section 2. A double-side calibration target with patterns printed on both faces was placed in the measurement volume and observed by all four cameras at multiple poses spanning the anticipated range of specimen positions and orientations. Intrinsic parameters, distortion coefficients, and camera poses were estimated for each camera, and a homogeneous transformation was determined to map the back-side reconstruction into the same global coordinate system as the front-side reconstruction. During the tensile test, image sequences from all four cameras were acquired at selected load or displacement increments. For each time step, 2D DIC was performed independently in each camera view to track subset centers relative to the reference image; stereo matching within each pair, combined with triangulation, yielded the 3D coordinates of the tracked material points on the front and back surfaces as functions of time. Applying the calibrated transform, the back-side reconstructions were expressed in the same global frame as the front side, so that the two surfaces could be compared pointwise.

The 3D contour and strain distribution on the surfaces of the DP980 was obtained through DIC measurement. Figure 3.3 illustrates the simultaneous measurement results of longitudinal stain map, width strain map and thickness strain map before fracture in the tensile test. The necking area, which is indicative of a strain concentration, can be clearly seen. R-value measurement results using two different methods are compared and analyzed. One method is the traditional measurement, or indirect measurement method, based on the volume constant assumption. The other method used is the direct thickness strain measurement method proposed in this paper, called the direct measurement method. The calculation method is shown in Eq. 8. Data in both the non-necking and necking area was selected for analysis to better show the difference between the two measurement methods.

A square area of 8×8 pixels subset is selected as a data point in the non-necking area, as shown in Figure 3.4 (a). The calculation results for the traditional and proposed methods are shown in Figure 12. According to the definition of R-value, the R-value for DP980 is equal to the slope of these two curves. It can be seen from the figure that the relationship between thickness strain and width strain is approximately linear, and the amount of noise in the data is low. Therefore, the least squares principle can be used to calculate the slope of the two curves. The directly measured R-value is 0.8546, while the indirectly measured R-value is 0.8656. Based previous research on the properties of DP980 material, its R-value generally ranges between 0.7-1.0, depending on the material's composition [24]. The results measured by both methods can be considered reasonable because they both fall within this range and the difference is very small. Therefore, both methods are acceptable.

When necking occurs during a tensile test, a large amount of strain is disproportionately distributed in a central location of the material. As the deformation continues, the strain in the necking area continues to increase until the material ruptures. In the necking stage, the cross-sectional area of the material decreases drastically, while the strain in the thickness and width directions increases sharply. Figure 3.5 displays an example of the strain increase sharply that can occur during the necking stage. An 8×8 pixels square area subset is selected in the necking area to obtain strain data, as shown in figure 3.4 (b). Figure 3.6 illustrates the R-value measured by the two methods in the necking area. In the linear elastic deformation stage, the thickness strain is proportional to the width strain. The R-value at this time is a constant, and the results measured by the two methods are 0.8471 and 0.8526 respectively; these results are similar to that measured in the non-necked area. This shows that the material is uniformly distributed, stable in nature, and isotropic. When the width strain exceeds 60mm/m, the strain value increases rapidly, and the material deformation enters the necking stage. It is worth noting that the direct method measurement curve no longer increases linearly; the growth rate reduces, and the R-value correspondingly becomes smaller. This shows that the ability of the material to resist strain in the thickness direction is reduced. Compared to the curve for the direct measurement method, the curve for the indirect measurement method remains linear in the early stage of necking, and the R-value does not decrease significantly until the late stages of necking. Several mechanisms can explain this divergence. First, damage and microvoid growth can cause a small but non-negligible volume increase, so that the sum $\varepsilon_l + \varepsilon_w + \varepsilon_t$ is no longer exactly zero. Second, localized necking produces a multi-axial stress state and strong gradients across the cross-section, which violate the assumption underlying the classical R-value derivation. Therefore, the R-value measured by the direct measurement method is more reliable and accurate in the necking stage. The R-values for DP980 in the three rolling directions are displayed in Table 1. The R-values in the three rolling directions are very similar, indicating that the material has similar resistance to thickness deformation in different rolling directions.

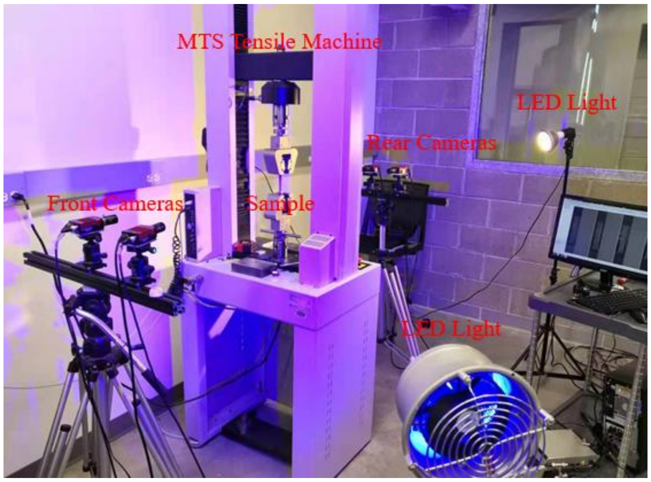

Figure 3.1 Experimental set-up of the R-value measurement.

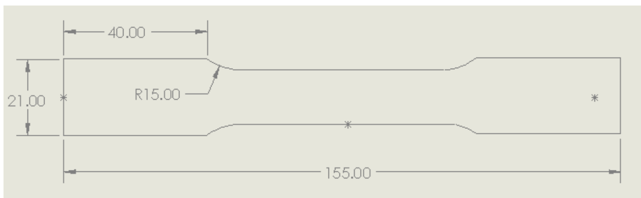

Figure 3.2 The schematic diagram of DP 980.

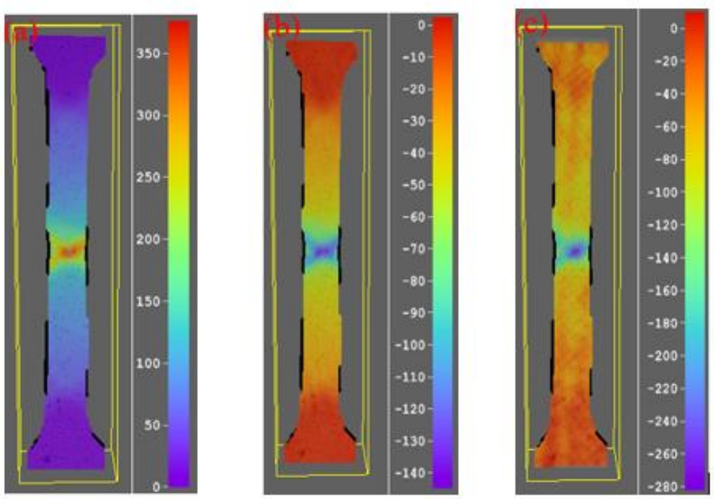

Figure 3.3 Full field strain distribution of sample surface measured by DIC system: (a) distribution of length strain; (b) distribution of width strain; (c) distribution of thickness strain.

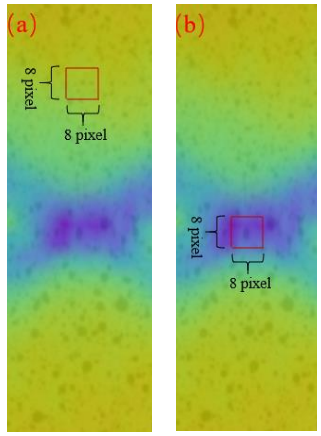

Figure 3.4 Calculation area of R-value: (a) Non-necking area; (b)Necking area.

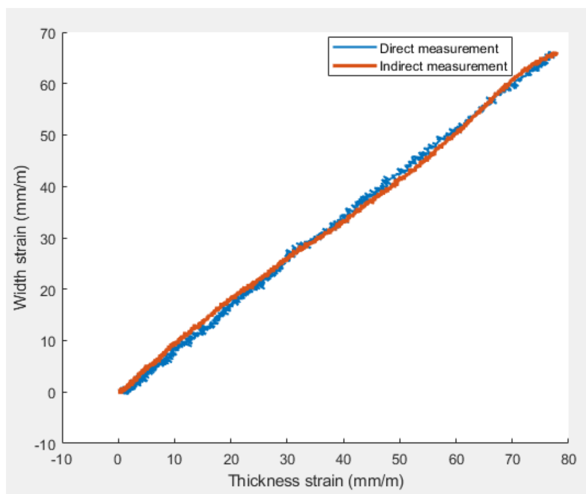

Figure 3.5 The R-value curve by two different measurement methods in the non-necking area.

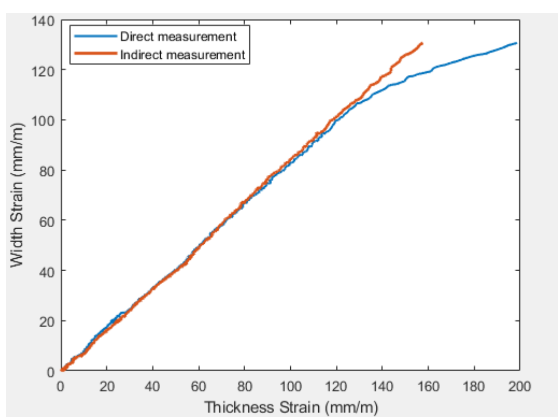

Figure 3.6 The R-value curve by two different measurement methods in the necking area.

3.3 Summary

This chapter has presented a direct R-value measurement methodology enabled by double-side DIC for thin sheet metals. Building on the dual-side framework developed in Chapter 2, the approach reconstructs the front and back surfaces simultaneously, expresses them in a unified global coordinate system, and uses their geometric separation to obtain a full-field thickness strain channel. Combined with conventional in-plane strain components, this provides the ingredients for a direct experimental evaluation of R-value, in which thickness strain is measured rather than inferred.

After reviewing the classical definition of the R-value and the common practice of using the volume constant assumption approximation to avoid direct thickness measurements, the experimental methodology was established. Thin sheet specimens were prepared with a well-defined specimen coordinate system, and a four-camera dual-side DIC setup was configured and calibrated using a double-side target to ensure a single global reference frame. During uniaxial tensile tests, full-field 3D kinematics were reconstructed on both surfaces, and longitudinal, width, and thickness strains were evaluated over a central gauge-region.

Using these strain fields, the direct R-value calculation results were compared with conventional indirect method. The comparison showed good agreement between direct method and indirect method in the early plastic regime, confirming both the validity of the volume constant assumption at small strains and the internal consistency of the dual-side measurement. At higher plastic strains, especially near the onset of necking, systematic deviations emerged. These deviations reflect the breakdown of the simple incompressible uniaxial model due to damage, non-uniform stress states, and geometry-induced effects, and they highlight the added value of directly measuring thickness strain.

CHAPTER FOUR

LOCALIZED NECKING DETECTION

4.1 Introduction to localized necking

Localized necking is a key instability phenomenon in sheet-metal forming and plays a central role in defining forming limits [37-38]. Once a localized neck forms, deformation concentrates in a narrow band and rapidly accelerates toward fracture, whereas the surrounding regions unload or deform only mildly. From an industrial point of view, the strain level at which localized necking initiates is often regarded as the practical limit of formability, and is used to build forming limit diagrams (FLD) and to calibrate material models for forming simulations. Accurate identification of localized necking onset is therefore crucial for both fundamental understanding and engineering applications.

Traditionally, forming limits have been determined using dedicated tests such as Nakajima or Marciniak–Kuczynski tests, where sheet specimens with different strain paths are stretched until fracture [39-45]. In classical practice, the onset of necking is inferred indirectly, for example from the curvature change of major strain versus time or from visual inspection of thickness or surface markings. With the adoption of digital image correlation in forming-limit testing, it has become common to analyze the evolution of full-field major strain and to define necking onset at the time when the spatial distribution of major strain begins to deviate strongly from a uniform pattern. A frequently used operational criterion is based on the time history of the maximum major strain in the gauge region: necking is assumed to initiate when the maximum strain accelerates relative to the average, or when a chosen measure of strain localization exceeds a threshold.

However, these strain-based criteria face several limitations. First, they rely exclusively on surface in-plane strain fields. While a strong gradient of surface major strain is a clear symptom of localization, it does not directly reflect the underlying change of the cross-sectional area, which is more closely linked to the material instability and load capacity. Second, strain fields obtained from DIC are subject to spatial smoothing and numerical differentiation, so that the details of the localization process, particularly near necking onset, can be sensitive to subset size, strain window, and filtering choices. Third, conventional stereo DIC measures only one surface, and thus requires indirect assumptions (such as volume constancy or plane stress) to relate in-plane surface strains to thickness reduction and cross-sectional area change. These assumptions may not hold locally once complex stress states or damage evolution become significant.

From a mechanics standpoint, localized necking is fundamentally associated with the evolution of local cross-sectional area. Under uniaxial tension, load carrying capacity is proportional to the minimum cross-sectional area; necking onset corresponds to the point where the cross-section at a particular location begins to decrease more rapidly than the rest of the gauge, leading to a localized loss of stability. This suggests that a criterion formulated directly in terms of local area evolution—rather than only surface strain patterns—might provide a more robust and physically interpretable identification of necking onset. To realize this idea experimentally, however, one needs access to both width and thickness change along the specimen, which is not straightforward with conventional single-side measurements.

The double-side DIC framework offers exactly this capability. By reconstructing the front and back surfaces in a unified coordinate system and providing direct thickness and thickness-strain measurements, it enables the local cross-sectional area to be evaluated along the gauge section as a function of load or time. Combined with the in-plane width information from the same DIC data, this allows local area evolution to be tracked continuously during tensile loading, and necking onset to be identified based on the change in behavior of the minimum cross-sectional area.

4.2 Localized necking detection based on cross-sectional area evolution

In the dual-side multi-camera DIC system, full-field engineering strains in the length, width and thickness directions can be measured directly during uniaxial tensile tests. This provides, in principle, all the information needed to monitor the evolution of the local cross-sectional area along the gauge section, which is the key geometric quantity governing necking. However, directly extracting the instantaneous cross-section from DIC images is non-trivial: the correlation domain does not exactly coincide with the specimen edges, and the algorithm itself has no explicit edge-detection capability. As a result, the color maps of strain or displacement typically under-cover the physical edges of the specimen, and the cross-section cannot be obtained simply by integrating a contour from the DIC field, as shown in figure 4.1. To overcome this difficulty, the localized necking detection method developed in this work reformulates the problem in terms of width and thickness engineering strains. Instead of measuring the cross-section directly from the image, the method reconstructs its evolution from the measured thickness and width strains along carefully defined virtual gauge lines, and then analyzes the different behaviors inside and outside the necking region.

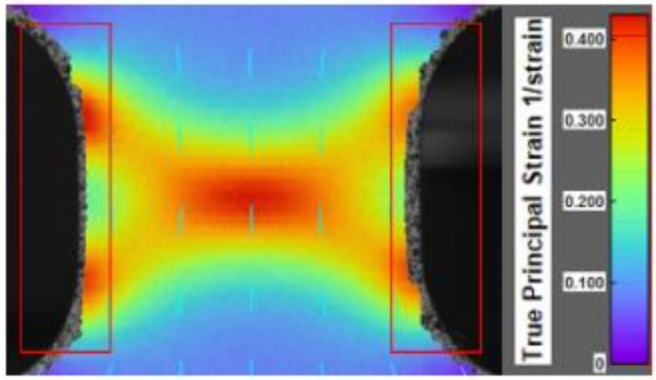

Figure 4.1 Areas not covered appear at the edge.

4.2.1 Cross-sectional area from thickness and width engineering strains

Let t_0, w_0 and A_0 denote the initial thickness, width and cross-sectional area of the specimen, respectively, at a given position along the gauge section. At some later time, the current thickness, width and area at the same location are denoted by t_i, w_i and A_i. The thickness and width engineering strains are defined as:

$$\varepsilon_{t,e} = \frac{t_i - t_0}{t_0} = \frac{t_i}{t_0} - 1 \tag{4.1}$$

$$\varepsilon_{w,e} = \frac{w_i - w_0}{w_0} = \frac{w_i}{w_0} - 1 \tag{4.2}$$

The instantaneous cross-sectional area then follows as:

$$A_i = t_i w_i = (1 + \varepsilon_{t,e})(1 + \varepsilon_{w,e}) t_0 w_0 = (1 + \varepsilon_{t,e})(1 + \varepsilon_{w,e}) A_0 \tag{4.3}$$

Figure 4.2 shows that the spatial distribution of the strain along the virtual line gauge fluctuates very little before the necking stage, which indicates that the deformation of the material in this section is uniform. However, after the material enters the necking stage, the thickness strain curve presents a concave shape, which indicates that there is a strain concentration in the middle region and the deformation is uneven. The average value of the strain on the virtual line gauge is taken as the strain in the necking area to calculate the percentage of cross-sectional area more accurately. Equation 4.3 can then be written as:

$$A_i = (1 + \overline{\varepsilon_{t,e}})(1 + \overline{\varepsilon_{w,e}})A_0 \tag{4.4}$$

where $\overline{\varepsilon_{t,e}}$ and $\overline{\varepsilon_{w,e}}$ represent the mean values of thickness strain and width strain on the virtual line gauge, respectively.

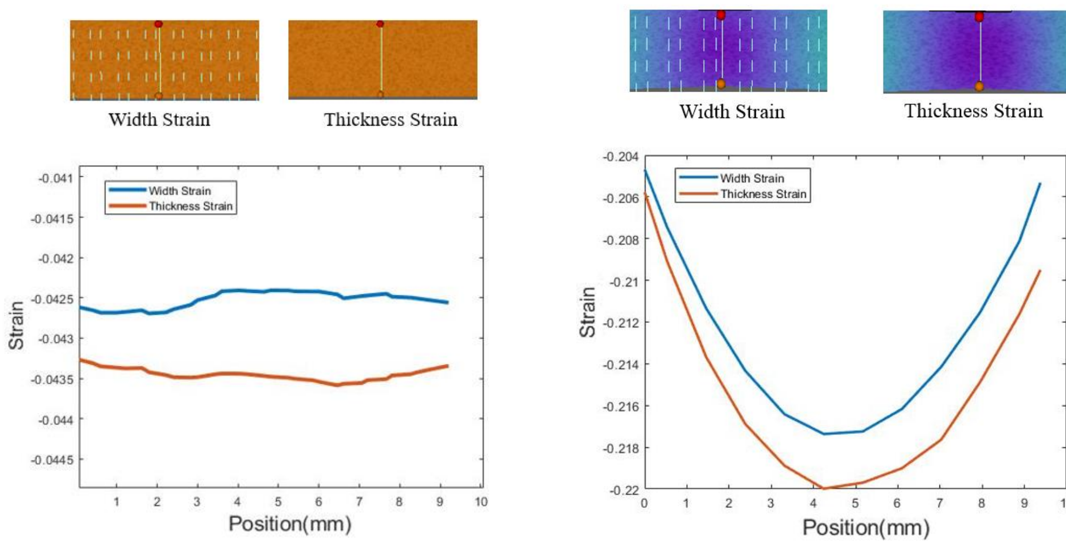

(a) (b)

Figure 4.2 Width and thickness strain distributions along the cross section: (a) Before necking; (b) Necking stage.

4.2.2 Determination of the necking region boundary

The proposed method is based on the observation that cross-sectional area inside and outside the necking region exhibits different evolutionary behavior once localized necking begins. To exploit this, it is first necessary to determine the spatial extent of the necking region, in particular the position of its boundary along the width direction. Because strain localization in uniaxial tension develops around the central axis of the specimen, a central virtual line gauge is defined along the loading direction in the last frame before fracture. As shown in figure 4.3, the thickness engineering strain distribution is extracted along this line, and its curvature with respect to the longitudinal coordinate is computed. Before necking, the thickness-strain profile is relatively flat, and its curvature remains small. During localized necking, the profile becomes strongly concave at the neck center, and the curvature in the vicinity of the necking boundaries becomes negative and decreases. In this work, the necking boundaries are identified from this curvature distribution in the final frame. The positions where the curvature first becomes negative and continues to decrease are taken as the two boundaries of the localized necking region on either side of the neck center.

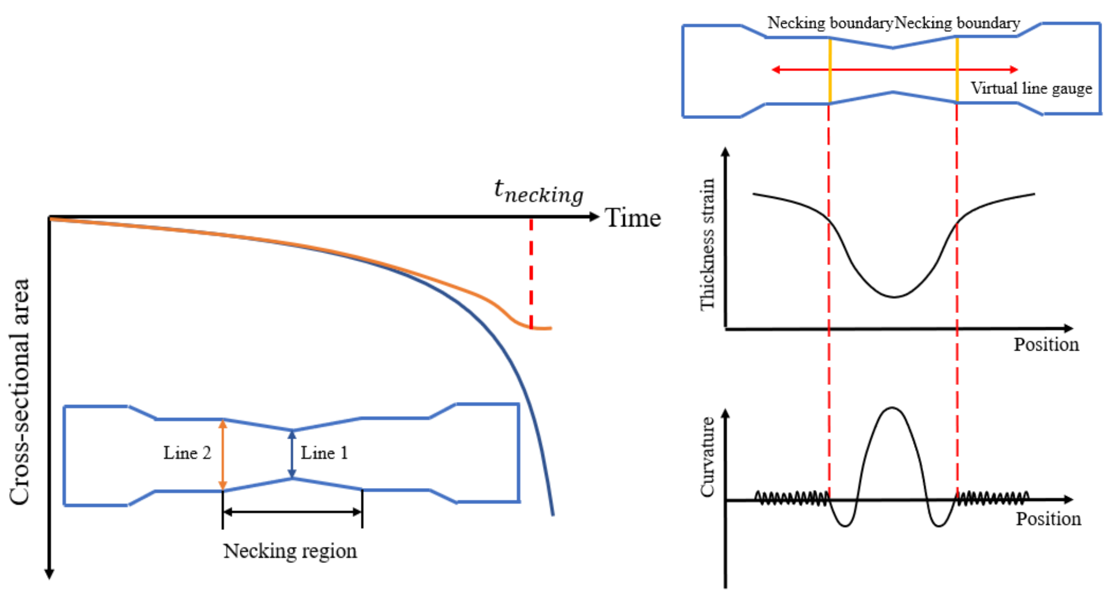

(a) (b)

Figure 4.3 The schematic of the proposed localized necking detection method: (a) Cross-sectional area evolution curve; (b) Determination of boundary of the necking region.

4.2.3 Time-dependent cross-sectional area criterion for necking onset

The central method of the proposed method is that localized necking is accompanied by distinct area-loss behavior at different positions across the necking region. Prior to necking, the cross-sectional areas at the center, in the boundary region, and outside the necking zone decrease in a similar manner as the specimen thins uniformly. Once localized necking develops, however, the cross-sectional area at the neck center continues to decrease rapidly, whereas the area at the boundary of the necking region gradually stops shrinking, and the area outside the necking region stabilizes even earlier. This behavior can be clearly seen by plotting the cross-sectional area histories for the multiple virtual line gauges introduced above. For the central line, cross-sectional area decreases monotonically throughout the test until fracture. For lines located between the center and the boundary, cross-sectional area initially follows the same trend but eventually begins to deviate and approaches a plateau. At the boundary line, cross-sectional area decreases initially, then reaches a turning point beyond which no further significant reduction occurs. Based on this observation, the onset of localized necking is defined as the time $t_{necking}$ at which the rate of change of the cross-sectional area at the necking boundary becomes zero:

$$\left.\frac{dA(t)}{dt}\right|_{t=t_{necking}} = 0 \tag{4.5}$$

where $A(t)$ denotes the area history at the boundary line. In numerical implementation, the first-order time derivative of is approximated by finite differences, and $t_{necking}$ is taken as the earliest time at which the derivative crosses zero and subsequently fluctuates around zero within a narrow band. Small oscillations near zero, caused for example by machine vibration or measurement noise, do not change the identification as long as the overall trend indicates that the boundary area has ceased to shrink.

4.2.4 Determination of limit strains at necking onset

After the necking onset time, is determined, the limit strains can be extracted directly from the DIC strain fields. Following standard practice in forming-limit determination, the limit major and minor strains are taken as the principal strain components measured in the central part of the necking region. In this work, a small neighborhood around the neck center is selected, and the average of the principal strains over this region is used to define the limit major strain and limit minor strain.

4.3 Experimental results

A standard tensile test was carried out on an MTS tensile testing machine with a maximum load of 50KN. Two low-carbon high-strength steels, BH240 and DP590, were tested using the experimental setup, and three specimens were tested for each steel to ensure repeatability. Two cameras with a resolution of 2750×2200 pixels (Prosilica GT 2750) were placed at each side of the machine to form two sets of DIC measurement systems. The measurement coordinate systems of the two systems were unified through the double-sided calibration strategy to achieve direct measurement of thickness and strain. Both sides of the specimen were sprayed with a randomly distributed speckle pattern before testing. Two LED lights with controllable lighting intensity were placed on both sides of the tensile test machine to provide a lighting environment for the test piece. The stretching rate of the tensile test machine was 5mm/min, the camera acquisition frequency was 10fps, and the four cameras were controlled by a trigger box to ensure pictures were taken synchronously. The lighting angle of the LED light and the camera exposure time was carefully adjusted to ensure that the surface of the specimen was illuminated evenly without reflective areas. The commercial DIC software ISTRA 4D was used to obtain the full-field displacement/strain data.

The width and thickness of the BH240 specimen was measured to be 12.87mm and 0.90mm, respectively. Figure 4.4 shows the distribution of engineering length strain, engineering width strain and engineering thickness strain of BH240 in the last frame before fracture. The presence of obvious strain concentrations of the specimen indicates the region where localized necking occurs. The process of determining the boundary of the necking region using the proposed method is illustrated in figure 4.5. Taking the last frame of DIC measurement data, both the thickness strain distribution and its curvature on the virtual line gauge are plotted. The boundary of the necking area can be identified as the point where the curvature curve starts to become negative, which can be located at two obvious positions on the curvature curve. As the strain of the specimen is symmetrically distributed around the necking area, the cross-sectional area evolution on one side can be selected for analysis. Figure 4.6 presents the cross-sectional area history curves for four different positions. The cross-sectional areas of four distinct positions, labeled as line 1, 2, 3, and 4, were analyzed. Line 1 is placed at the center of the necking area, while line 3 is at the boundary of the necking area. Line 2 is located between line 1 and line 3, and line 4 is placed outside the necking area. The cross-sectional areas at the four different positions begin to separate after diffused necking occurs. The cross-sectional area at line 1 continues to decrease until the sample breaks, while the cross-sectional areas of the other three positions outside the center of necking shrink to a certain extent then stops decreasing. Of particular interest is the change in cross-sectional area at line 3 placed at the boundary of the necking region. The time $t_{necking}$ when the localized necking begins to occur corresponds to the point when the first-order derivative of the cross-sectional area of the boundary of the localized necking region is equal to zero. Figure 4.7 shows the evolution of the first-order derivative. The first-order derivative value fluctuates slightly after becoming zero, which may be due to the noise effect caused by the vibration during the tensile test. Using the proposed methods, the limit major strain and limit minor strain were determined to be 0.469 and -0.277 respectively in Figure 4.8.

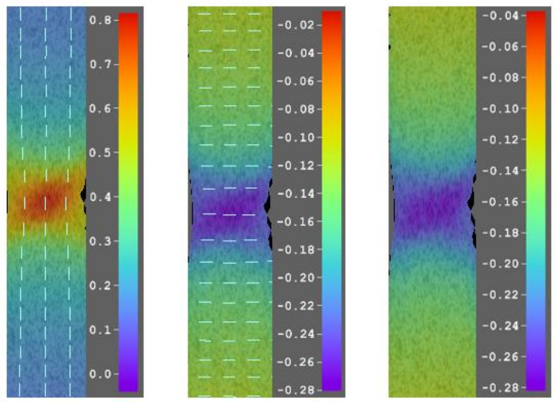

(a) (b) (c)

Figure 4.4 Full field engineering strain distribution of BH240: (a) Length strain; (b) Width strain; (c) Thickness strain.

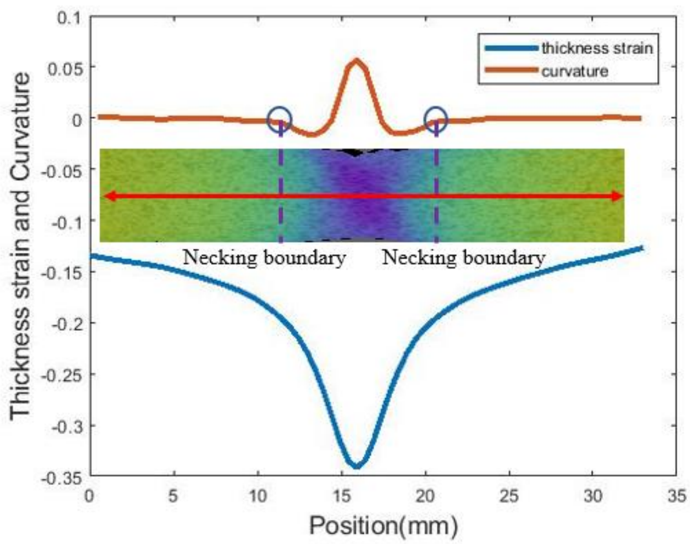

Figure 4.5 Spatial distribution of thickness strain and curvature of BH240.

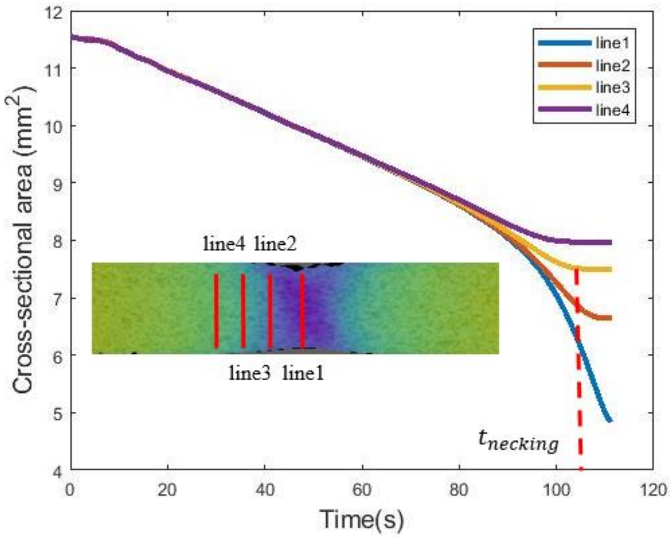

Figure 4.6 Cross-sectional area evolution curves located in different regions for BH240.

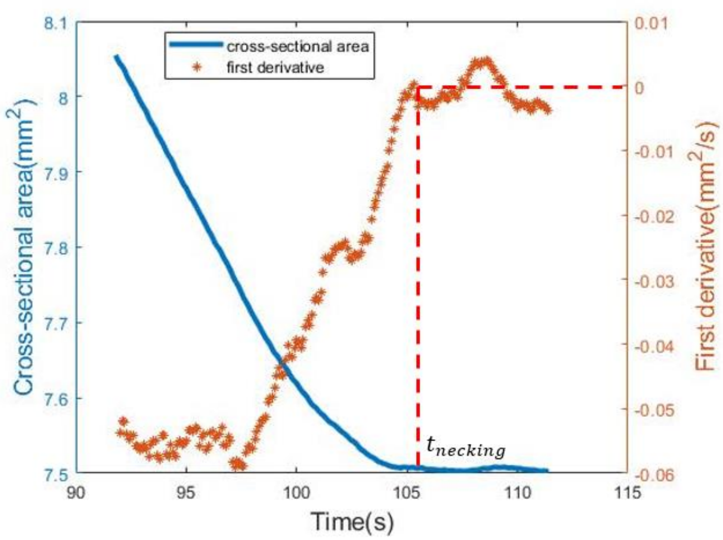

Figure 4.7 First-order derivative of line 3 for BH240.

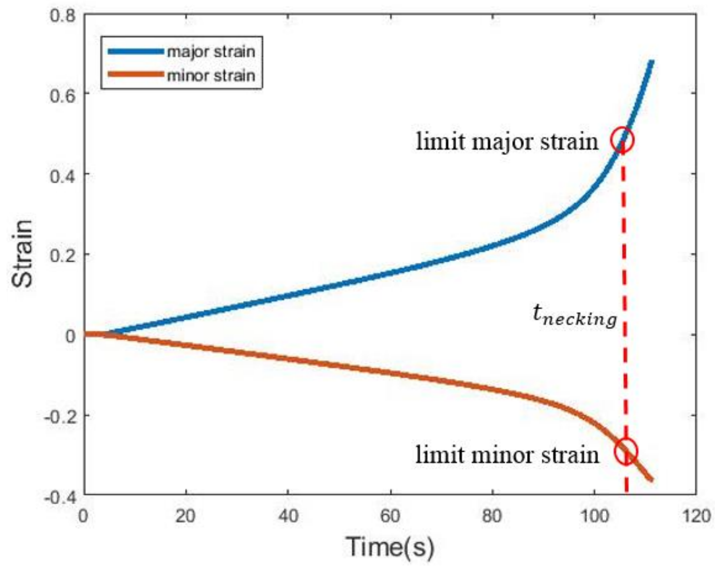

Figure 4.8 Determination of limit major strain and limit minor strain at localized necking time for BH240.

DP590 has higher strength and lower ductility than does BH240. The width of the test specimen was measured to be 12.89mm, while the thickness of the test specimen was 0.89mm. Figure 4.9 shows the engineering strain distribution in the length, width, and thickness directions of the last frame before fracture. A significant strain concentration develops along the 45° direction and finally forms a fracture at this location. Figure 4.10 displays the necking boundary as determined by the spatial distribution of the thickness strain and curvature at the last frame. The evolution of the cross-sectional area of four lines placed at different positions at and near the center of necking is shown in figure 4.11. The cross-sectional area located in the necking area was found to continually shrink, while the cross-sectional area located at the boundary of the necking area and outside the necking area was found to gradually stops shrinking. Figure 4.12 and figure 4.13 illustrate the limit major strain for DP590 was determined to be 0.337 and the limit minor strain was -0.144.

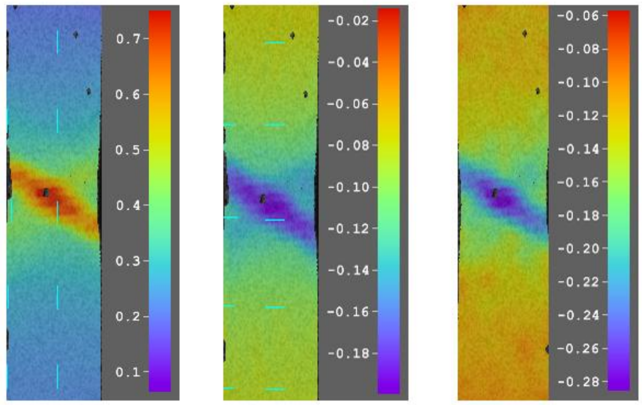

Figure 4.9 Full field engineering strain distribution of DP590: (a) Length strain; (b) Width strain; (c) Thickness strain.

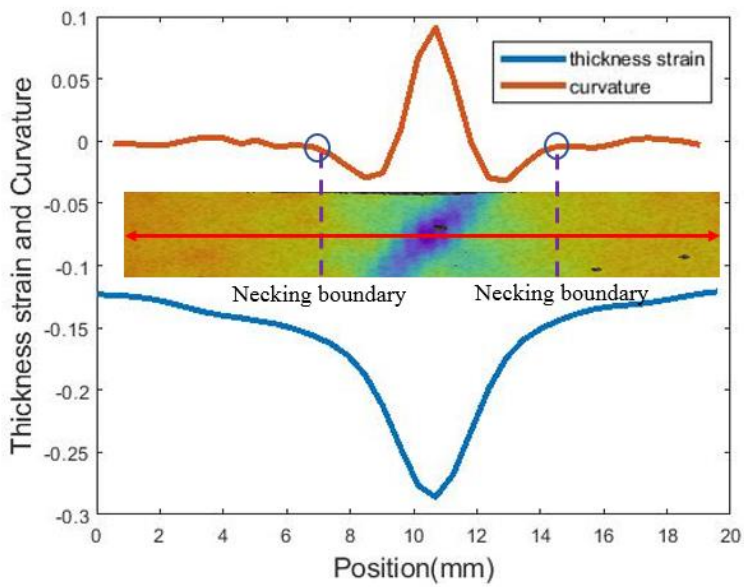

Figure 4.10 Spatial distribution of thickness strain and curvature of DP590.

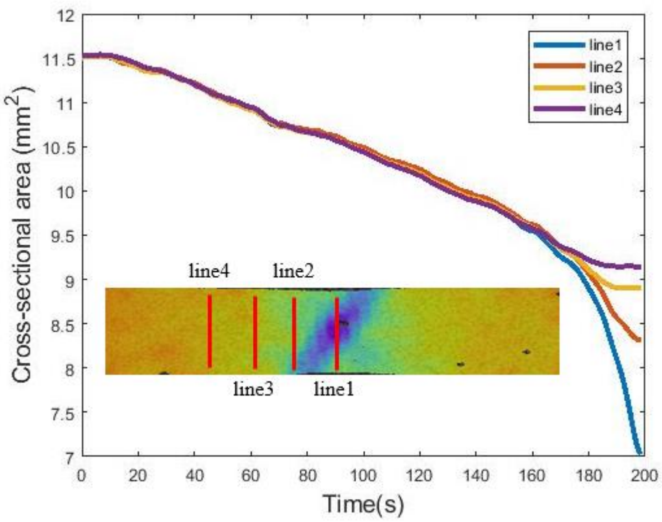

Figure 4.11 Cross-sectional area evolution curves located in different regions for DP590.

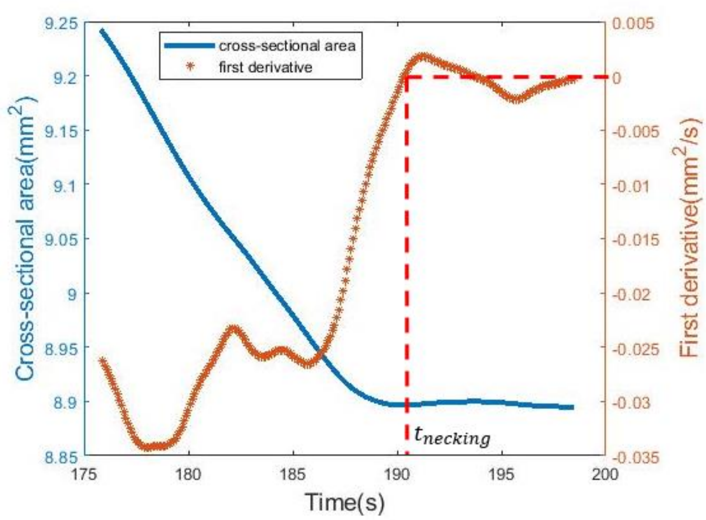

Figure 4.12 First-order derivative of line 3 for DP590.

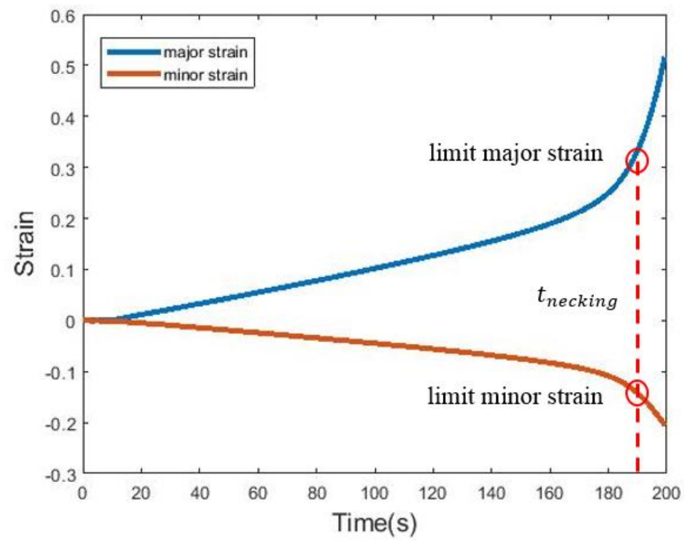

Figure 4.13 Determination of limit major strain and limit minor strain at localized necking time for DP590.

4.4 Comparison and discussion

The limit strain of BH240 and DP590 were also determined by several different methods in uniaxial tensile tests to verify the effectiveness of the proposed method. The methods used to evaluate the proposed method's effectiveness include the ISO method, the curvature method, the bifurcation method and the second derivative method. Figure 4.14 shows the local necking process of BH240 determined using different methods. The ISO method is a typical spatial determination method. Strain data on a virtual gauge line perpendicular to the necking region before specimen fracture was used for analysis. The limit strain was determined by fitting inverse parabolas through the data points of the inner and outer boundaries, which were defined by the second derivatives of the strains. As shown in figure 4.14(a), the limit major strain and minor strain correspond to inverse parabolic values at the fracture site. The curvature method is based on surface topography to determine onset of localized necking. The curvature of the surface perpendicular to the necking area was calculated at each frame, and the onset of localized necking was detected by comparing the root mean square of the curvature with the curvature value at the fracture. Figure 4.14(b) shows the surface curvature for each frame, and the red line is the curvature distribution when localized necking occurs. The bifurcation point detection method is based on the analysis of the evolution of strain through the thickness. The onset of localized necking corresponds to the intersection of two bifurcated curves fitted by two cubic polynomials, as shown in figure 4.14(c). The second-order derivative method assumes that localized necking begins when the second-order derivative of the principal strain becomes constant. However, in actual measurement, the change of the second-order derivative is a process of gradual increase. Therefore, 10% of the maximum value of the second-order derivative is used as the threshold to determine the beginning of localized necking, as shown in figure 4.14(d). Tables 1 and 2 respectively show the limit strain results for BH240 and DP590 as determined by the previously mentioned methods. Three uniaxial tensile tests were performed for each material. The limit strain obtained using the ISO method is taken as a reference value since it has been widely accepted. Tables 4.1 and 4.2 show that the limit strain value determined using the method proposed in this paper is very similar to the strain values using the ISO method, thus showing good consistency. The strain values using the curvature method are slightly lower, deviating by approximately 8% for both materials. Similarly, the bifurcation point method yields strain values that are approximately 10% lower for BH240 and 24% lower for DP590. This discrepancy can be attributed to the sensitivity of this method to the range of fitted data and function order used. Additionally, the strain values determined using the second derivative method appear to be overly conservative due to the 10% threshold selection used.

The proposed method has several advantages over existing methods. Its focus on the evolution of the cross-sectional area is more straightforward and simpler to implement than the ISO method. Furthermore, the calculation required for this method is less cumbersome compared to the curvature method, which needs to compute the curvature of the space coordinates for each frame. In addition, during the localized necking stage, the material may form voids and render the assumption of constant volume invalid. As a result, the results obtained from the bifurcation method based on the analysis of the evolution of thickness strain may be impacted. For the proposed method, the calculation of the cross-sectional area is derived from the direct measurement of the width strain and the thickness strain, and the limit strain is more accurate. Finally, determining the threshold of the second-order derivative method requires empirical settings, which are not applicable universally to different materials.

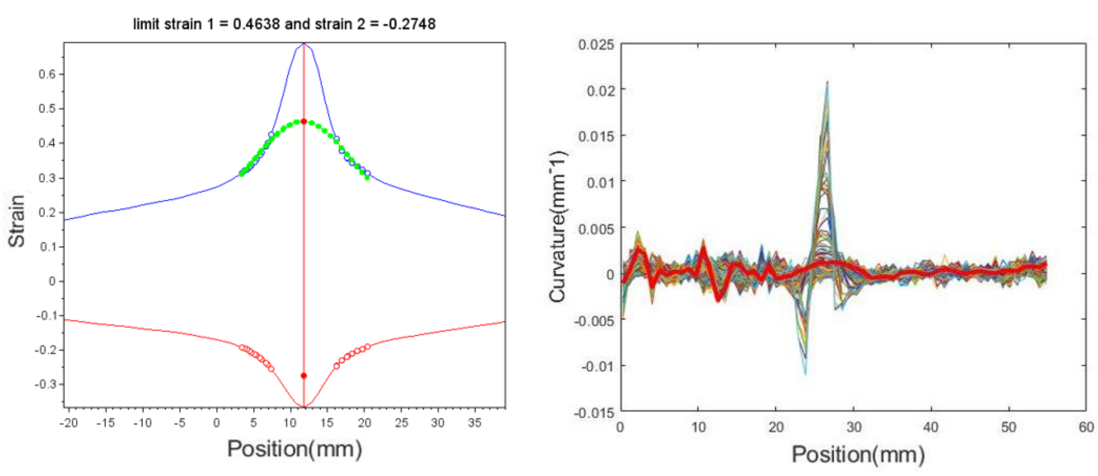

(a) (b)

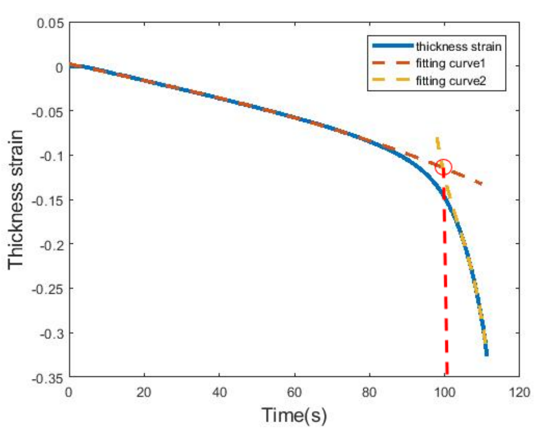

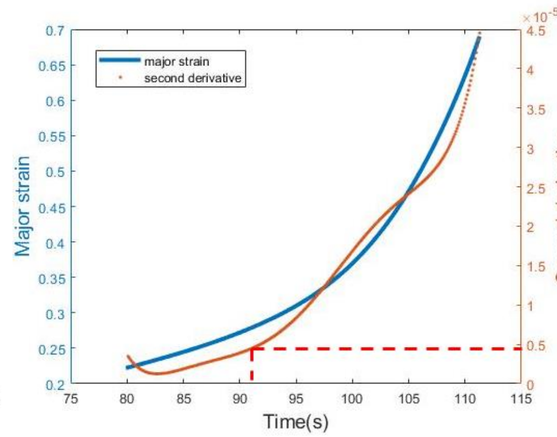

(c) (d)

Figure 4.14 Determination of localized necking strain for BH240 by different methods.: (a) ISO method; (b) Curvature method; (c) Bifurcation method; (d) Second derivative method.

Table 4.1 Results of limit strain for BH240.

Sample	ISO method		Proposed method		Curvature method		Bifurcation method		Second derivative method	
	Major strain	Minor strain	Major strain	Minor strain	Major strain	Minor strain	Major strain	Minor strain	Major strain	Minor strain
1	0.464	-0.275	0.469	-0.277	0.424	-0.253	0.404	-0.242	0.286	-0.175
2	0.450	-0.265	0.460	-0.272	0.411	-0.244	0.398	-0.235	0.297	-0.180
3	0.456	-0.266	0.458	-0.271	0.415	-0.245	0.410	-0.245	0.292	-0.178
Mean	0.457	-0.269	0.462	-0.273	0.417	-0.247	0.404	-0.241	0.292	-0.178

Table 4.2 Results of limit strain for DP590.

Sample	ISO method		Proposed method		Curvature method		Bifurcation method		Second derivative method	
	Major strain	Minor strain	Major strain	Minor strain	Major strain	Minor strain	Major strain	Minor strain	Major strain	Minor strain
1	0.326	-0.142	0.337	-0.144	0.303	-0.131	0.242	-0.106	0.228	-0.100
2	0.338	-0.145	0.343	-0.147	0.311	-0.134	0.258	-0.112	0.245	-0.106
3	0.341	-0.147	0.348	-0.149	0.315	-0.136	0.263	-0.114	0.252	-0.108
Mean	0.335	-0.145	0.343	-0.147	0.310	-0.134	0.254	-0.111	0.242	-0.105

4.5 Summary

This chapter has presented a new localized necking detection method for uniaxial tensile tests, developed on top of the dual-side multi-camera DIC system introduced earlier in this thesis. The method is built around a physically intuitive idea: when localized necking develops, the cross-sectional area at different positions across the necking region behaves differently. In particular, the cross-sectional area at the center of the neck continues to decrease sharply, whereas at the boundary of the necking region it eventually stops decreasing, and outside the necking region it stabilizes even earlier. The chapter then proposed a time-dependent area-based necking criterion. The boundary of the necking region was identified from the curvature of the thickness-strain profile along the specimen axis in the last frame before fracture: positions where the curvature became negative and continued to decrease were taken as necking boundaries. With this boundary known, cross-sectional area histories were computed at several positions (center, intermediate, boundary, and outside) using the virtual gauge approach. It was observed that, after diffuse necking, the area curves begin to separate: at the center they continually decrease, while at the boundary and outside they decrease to a certain level and then stop. Based on this, localized necking was defined to initiate when the first derivative of the cross-sectional area at the boundary position becomes zero, and the corresponding limit major and minor strains were taken from the neck center at that instant.

The method was implemented and validated on uniaxial tensile tests of BH240 and DP590 sheet steels using a four-camera DIC setup with front–back synchronization and double-sided calibration. For each material, three repeated tests were analyzed. The limit strains obtained with the proposed method were compared against those obtained from several established necking criteria, including the ISO inverse-parabola method, the curvature method, a bifurcation method based on thickness-strain evolution, and a second-derivative method with a prescribed threshold. For both materials, the limit strains from the proposed method showed very good agreement with the ISO method, which was taken as a reference, while the curvature and bifurcation methods generally yielded lower (more conservative) strains, and the second-derivative method was even more conservative due to the empirical 10% threshold.

Finally, the chapter discussed the advantages and limitations of the proposed area-based criterion. Compared to the ISO method, it is conceptually simpler and avoids fitting inverse parabolas and defining inner/outer boundaries in strain space. Compared to curvature methods, it does not require frame-by-frame surface curvature computation in 3D space. Unlike bifurcation approaches based solely on thickness strain, it does not rely on volume constancy, which may be violated in the presence of void formation and damage. It also avoids empirical thresholds required by second-derivative methods. On the other hand, the method currently relies on a multi-camera DIC configuration with sufficient space and access around the specimen, and the assumption that a virtual line gauge across the width remains sufficiently straight in the necking stage introduces some approximation. These limitations suggest natural directions for future work, including extending the approach to biaxial tests and other forming paths, and refining the treatment of large inhomogeneous strains and gauge-line distortion. Overall, this chapter demonstrates that the cross-sectional area-based necking criterion, enabled by double-side multi-camera DIC, provides a new tool for determining localized necking strains in sheet metals.

CHAPTER FIVE

TENSILE PROPERTIES OF HAZ IN TAILOR-WELDED BLANKS WITH UNEVEN THICKNESS

5.1 Introduction to HAZ

Tailor welded blanks (TWB) made from advanced high-strength steels are widely used in automotive body structures as an effective light weighting strategy [46-48]. By welding together sheets with different thicknesses and/or grades into a single tailored blank, material can be placed where it is most needed, enabling weight reduction, cost savings, and improved crash performance. During laser welding, however, the base sheets experience highly non-uniform thermal cycles, which produce a fusion zone (FZ) in the melted region and heat-affected zones (HAZ) on either side where the material is not melted but undergoes microstructural changes. For TWBs made from the same base material, it is generally recognized that the HAZ exhibits lower strength than both the base material and the FZ, so that the global formability of the welded blank is often governed by the mechanical response of the HAZ. Accurately characterizing the tensile properties of the HAZ is therefore essential for reliable forming feasibility assessment and numerical simulation of TWB components.

Experimentally, two families of methods are commonly used to investigate weld properties: indentation-based techniques and tensile tests. Microhardness and nanoindentation measurements provide local information on hardness and elastic modulus [49-52]. They are particularly useful for mapping the spatial extent of the FZ and HAZ and for distinguishing softened and hardened regions near the weld. Under assumptions on the correlation between hardness and flow stress, hardness profiles can also be used to estimate strength variations across the weld. However, the relationship between hardness and tensile strength is not strictly linear, especially at lower hardness or strength levels, and may introduce non-negligible uncertainty when used to infer detailed stress–strain curves [53]. Uniaxial tensile tests on welded coupons, often assisted by digital image correlation (DIC), offer a more direct route to tensile stress–strain behavior. In principle, sub-sized specimens extracted from individual zones (FZ, HAZ, base material) can be tested, and full-field strain measurements can be used to obtain local stress–strain curves [54-61]. In practice, preparing small, defect-free coupons from narrow zones and ensuring accurate load transfer is demanding. When standard-size welded coupons are used instead, additional difficulties arise. In particular, for TWBs with uneven thickness, the step in sheet thickness across the weld produces an eccentric load path. Even if the specimen is carefully aligned in the grips, a local bending moment is generated in the gauge section, and the nominal stress (force divided by nominal cross-sectional area) no longer represents the actual stress state in the HAZ. At the same time, differences in thickness and microstructure between the two sides of the weld lead to stress concentration, strain gradients, and possible stress triaxiality near the HAZ.

To address these challenges, this chapter builds upon the multi-camera DIC framework and proposes a combined indentation–tensile methodology to obtain tensile properties of the HAZ in TWBs with different base-material thicknesses. The approach uses: (1)microhardness mapping to identify the FZ and HAZ boundaries and to estimate reference strength values; (2)nanoindentation to determine the elastic modulus in the HAZ; (3)a four-camera, dual-side DIC setup to measure full-field strains and thickness distributions on both surfaces of a standard tensile coupon; (4) a multiple linear regression model that links the nominal strain in the HAZ to the front- and back-surface strains, thereby correcting bending-induced errors in the stress–strain curve.

The method is demonstrated on laser-welded TWBs made from dual-phase steel DP1180 with sheet thicknesses of 1.0 mm and 1.4 mm. The corrected stress–strain curves of the HAZ are compared with strength estimates from microhardness, and the tensile behavior of the FZ and base materials is also examined for completeness. Through this study, the double-side DIC system is further shown to provide not only thickness-strain and necking information, as in the previous chapters, but also a practical route for calibrating local constitutive behavior in welded structures with geometric and material inhomogeneities.

5.2 Experimental methodology

5.2.1 Materials and sample preparation

The material tested in this paper is a dual-phase advanced high-strength steel, DP1180. Two steel sheets with thicknesses of 1 mm and 1.4 mm are welded together by laser. Dogbone samples, with a gage width of 12.7 mm (0.5 in.) and gage length of 57.15 mm (2.25 in.), are waterjet cut out of the welded sheets, as shown in figure 5.1. This section describes the microhardness, nanoindentation, and uniaxial tensile test methods performed to characterize the mechanical properties of the TWBs.

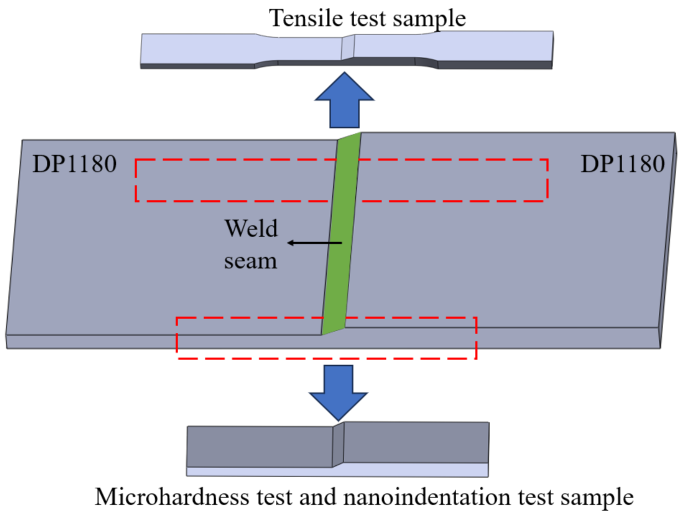

Figure 5.1 The schematic of specimen waterjet cutting.

5.2.2 Microhardness test

Three microhardness test lines were located at 1/4, 1/2 and 3/4 thicknesses of the specimen. Each line consisted of 35 microhardness indentations and the spacing between indentations was approximately 0.18 mm, as shown in figure 5.2. Vickers microhardness was determined using a load of 300 g and a dwell time of 13 s.

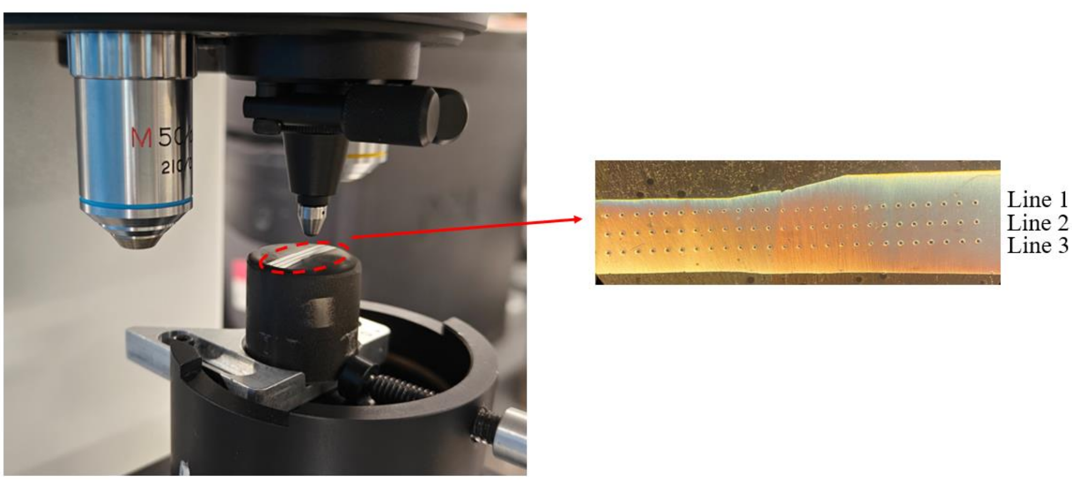

Figure 5.2 Microhardness test specimen and test lines.

5.2.3 Nanoindentation test

To determine the Young's modulus of the HAZ, a rectangular area measuring 5300 μm in length and 265μm in width near the weld seam was subjected to nanoindentation testing. The nanoindentation experiments were conducted on a Bruker TI980 TriboIndenter at room temperature. The sample was polished to a mirror surface before nanoindentation. The accelerated property mapping method, the XPM testing routine, was employed in 3 row x 24 column with 3 μm spacing between indents. And then the XPM tests were automated by stitching them in a row resulting in a 5.1 mm total length across the HAZ. The spacing between indents remains at 3 μm in the whole mapping area. The traperzoid load function was selected with 0.1 s on loading, holding, and unloading, respectively. The maximum load of 8000 μN was chosen. The nanoindentation data analysis was performed using Bruker Tribo iQTM software package.

The most widely used nanoindentation testing method currently is the Oliver-Pharr method [31]. Figure 5.3 shows the nanoindentation load-displacement curve. At the beginning of the loading process, the sample being tested is squeezed by the tip of the indenter, which first produces elastic deformation. As the indentation depth increases, the sample gradually begins to undergo plastic deformation with a nonlinear load-displacement curve. During the unloading process, the sample elastically relaxes. Upon complete unloading, an indention is visible on the surface due to irreversible plastic deformation. Figure 5.4 is a schematic cross-sectional view of the sample surface before and after loading. The microhardness H and reduced modulus E_r are defined by:

$$H = \frac{P_{max}}{A_c} \tag{5.1}$$

$$E_r = \frac{S\sqrt{\pi}}{2\beta\sqrt{A_c}} \tag{5.2}$$

where P_{max} is the maximum load, A_c is the contact area, $S = dP/dh$ is the contact stiffness at the initial unloading, and β is a constant which depends on the geometry of the indenter. The Young's modulus of the specimen can be calculated by

$$\frac{1}{E_r} = \frac{1-v^2}{E} + \frac{1-v_i^2}{E_i} \tag{5.3}$$

E_i is the elastic modulus of the indenter, and v and v_i are the Poisson's ratio of the specimen and the indenter, respectively.

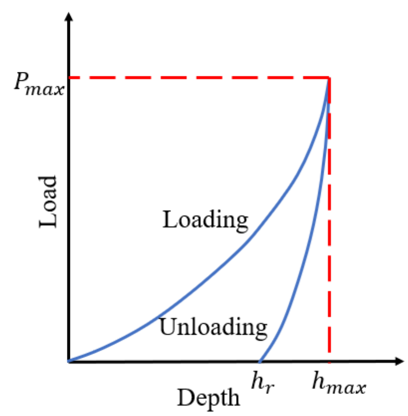

Figure 5.3 A typical load-depth curve.

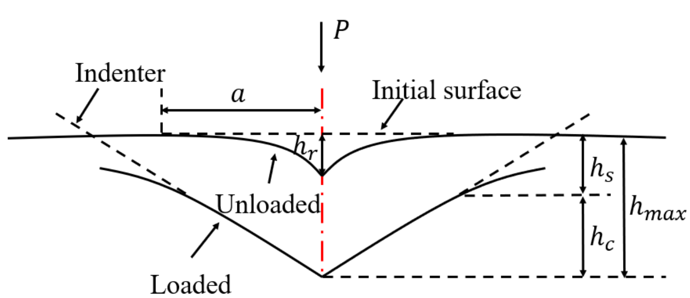

Figure 5.4 The schematic of the sample surface before and after loading.

5.2.4 Tensile test set up

In this study, the back side of the tensile coupon corresponds to the bottom surfaces of the joined sheets, which are flush. The front surface, which is incident with the applied laser, has a step with a height equal to the difference between the two sheet thicknesses. The traditional 3D-DIC testing system uses dual cameras to measure deformation on one side of the specimen, which is sufficient for metal specimens of uniform thickness because the deformation behaviors of the front and back surfaces are the same under uniaxial tension. However, there are different local deformation characteristics on the front and rear surfaces of unequal thickness weldments due to stress concentration in the tensile test. Dual-camera 3D-DIC becomes insufficient to provide strain information on both sides of the specimen, making it necessary to use a double-side DIC system to simultaneously measure strain on the front and rear surfaces of the specimen. Since the double-side DIC measurement system can provide strain information on both sides of the specimen, it becomes feasible to calculate the nominal strain under nominal stress using the results from both sides. This approach offers a new perspective for correcting stress-strain curve distortions caused by stress concentration. A standard-sized specimen was clamped on the MTS tensile machine. The thickness of the thin side of the specimen is 1.0 mm, and the thickness of the thick side is 1.4 mm. A 0.4 mm thick aluminum shim is bonded to the thin side of the specimen, to align the sample with the axis of the tensile test machine, therefore eliminating any bending moment that would be applied due to clamping. Both sides of the specimen were sprayed with randomly distributed speckle patterns. Two high-resolution cameras (Prosilica GT 2750) were placed on each side of the tensile machine to form a multi-camera DIC system, and the four cameras achieve synchronous trigger acquisition of images through the trigger box. Two LED lights with adjustable light intensity are located on both sides of the stretching machine to provide the best lighting environment for the test specimen. The tensile rate of the stretching machine was set to 5 mm/min, and the image acquisition frequency of the camera was 10 fps.

5. 3 Experimental Results and Discussion

5.3.1 Microhardeness distribution

The hardness measurement results are shown in figure 5.5. It can be seen that the results of the three lines are similar, which shows that the hardness of the specimen is uniformly distributed along the thickness direction and has similar material properties. In addition, the hardness distribution is in the shape of a peak with a high center and low sides. Different hardness values also mean different microstructures, which can be used to identify the HAZ, FZ and base zone. During the welding process, the elevated temperatures induce the formation of martensite in the FZ, exhibiting characteristics of high hardness, as evidenced by the high-hardness region observed in the hardness profile, spanning approximately 2 mm in width. Adjacent to the FZ, there is a region characterized by a rapid decrease in hardness followed by a gradual increase, identified as HAZ 1 and HAZ 2. Within the HAZ, portions exhibit reduced hardness compared to the base material due to martensitic tempering, referred to as the softened zone. The overall width of the HAZ is approximately 3.4 mm, symmetrically distributed between the FZ and the BZ. The average microhardness within the FZ measures 381 HV, marking a 33.2% increase compared to the average hardness in the HAZ (290 HV), and a 12.3% increase compared to the average hardness of the base material (339 HV).

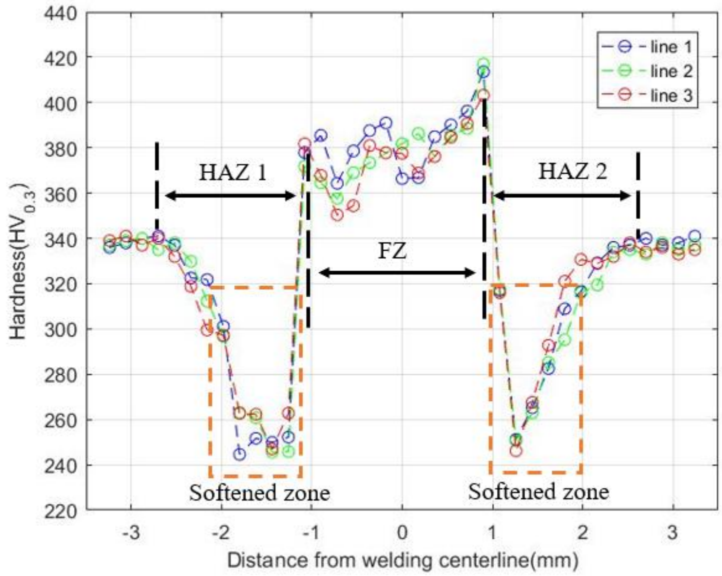

Figure 5.5 Vickers hardness profile across the weld seam.

5.3.2 Nanoindentation for Young's modulus measurements

Figure 5.6 shows the Young's modulus distribution results within the region of interest through nanoindentation testing. It can be seen that the Young's modulus is relatively evenly distributed in HAZ 1 and WZ, while there is an obvious decrease in HAZ 2. The average Young's modulus of the three regions are 207 GPa, 208 GPa and 195 GPa respectively. Due to the different thicknesses of HAZ 1 and HAZ 2, uneven heat transfer during laser welding may cause HAZ 1 and HAZ 2 to form different crystal structures, consequently resulting in variations in Young's modulus.

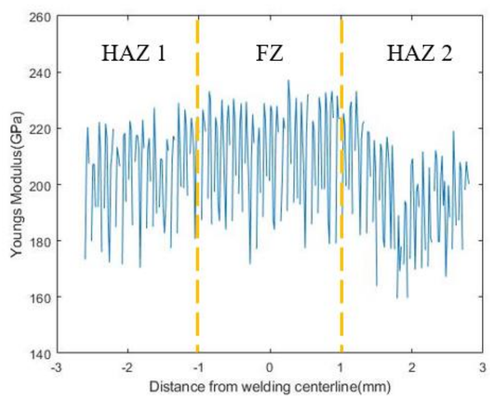

(a)

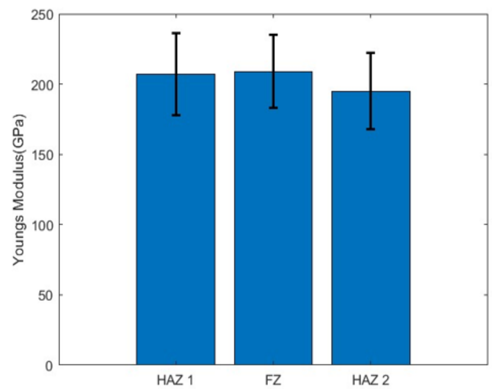

(b)

Figure 5.6 Nanoindentation test results of HAZ 1, FZ and HAZ 2: (a) Young's modulus profile; (b) Average Young's Modulus.

<u>5.3.3 Determination of HAZ position from the thickness distribution</u>

The multi-camera DIC system provides thickness information of the specimen to determine the location of the HAZ in the DIC images. As shown in figure 5.7 (a), the full-field thickness distribution of the specimen before the tensile test reveals regions colored in purple and orange, corresponding to the thin and thick sides of the specimen, respectively. The thickness of the thin and thick sides measures 1.13 mm and 1.50 mm. Figure 5.7 (b) illustrates the thickness distribution along a 10 mm-long line gauge spanning the weld seam. A transition region approximately 2 mm in length appears between the two sheets of different thicknesses. Comparison with the hardness distribution results indicates that this transition region corresponds to the FZ. Therefore, the rectangular area with a length of 1.7 mm on both sides immediately adjacent to the transition area is the position of the HAZ on the DIC image.

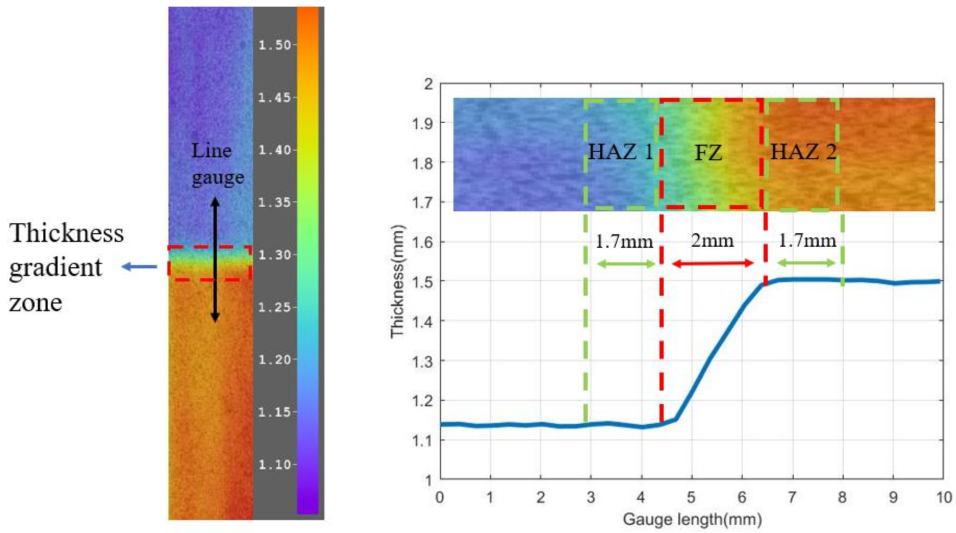

(a) (b)

Figure 5.7 Identification of HAZ: (a) Full-field color contour of thickness distribution; (b) Thickness profile along a 10 mm-long line gauge across the weld seam.

5.3.4 Temporal and spatial distribution of major strains

The full-field major strain at the front and back of the specimen under different maximum strains are shown in figure 5.8. The upper cloud image shows the front surface strain distribution, and the lower cloud image shows the back surface strain distribution. Major strains on the front and back surfaces of the specimen exhibit significant differences near the weld seam when the maximum strains are 0.5%, 5% and 10% respectively. Specifically, the weld seam strain on the front surface of the specimen is higher than the adjacent regions, while the corresponding weld seam strain on the back surface is lower than the adjacent regions. Similar strain distributions on the front and back surfaces are only evident near the point of specimen fracture (maximum strain is 16%). Along a 30 mm virtual line gauge centered on the specimen's central axis, the spatial distribution of strains in the weld seam area was quantitatively analyzed, as illustrated in Figure 5.9. The spatial distribution of strains on the front and back surfaces exhibits a similar uniform pattern in the base material region. However, in the HAZ and FZ, completely opposite trend of variations is observed until when the specimen approached fracture. In the HAZ 1, the strain on the front surface increases rapidly and reaches the maximum value near the junction of HAZ 1 and FZ. This is because the cross-sectional area of the specimen suddenly increases at the junction, causing stress concentration on the front surface. The corresponding strain decreases rapidly at the back surface. Within the FZ, the strain on the front surface begins to decrease steeply, attributed to the higher strength of the FZ compared to the base material and HAZ. Conversely, the strain on the back surface exhibits an increase, with stress concentration occurring at the junction of the back surface FZ and the HAZ 2, evinced by a local peak strain. Since the HAZ 1 is the weakest region of the entire specimen, localized necking occurs here. After localized necking, the strain on the back surface of the HAZ 1 gradually increases until the specimen fractures.

To illustrate the accuracy of the DIC strain measurement, Figure 5.10 shows the full-field distribution of the standard deviation of the principal strain. The standard deviation value does not vary significantly in the different stages of the tensile test and remains at a low level. During the elastic deformation stage, where the deformation is small, the measurement error is higher at lower strains compared to higher strains. At the 0.5% strain level, the average relative measurement error is the highest, amounting to approximately 12%, whereas at the 16% strain level, the average relative measurement error is only 0.1%.

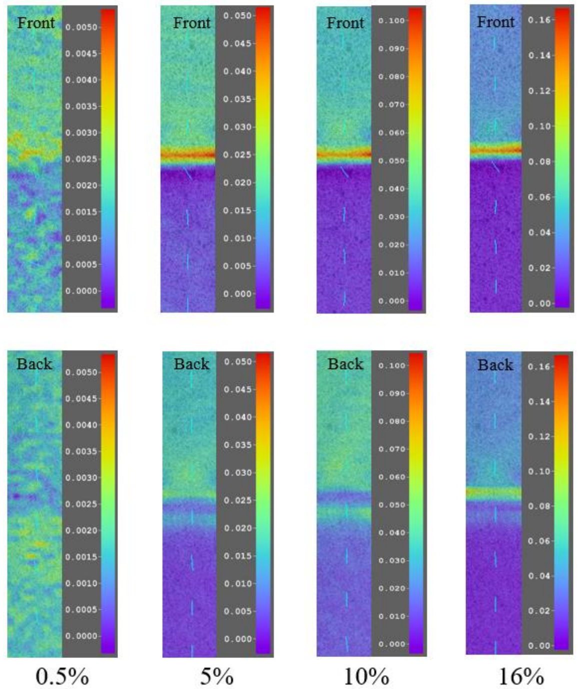

Figure 5.8 Full-field major strains distribution on the front and back sides of the tensile specimen at different maximum strain levels of 0.5%, 5%, 10% and 16%

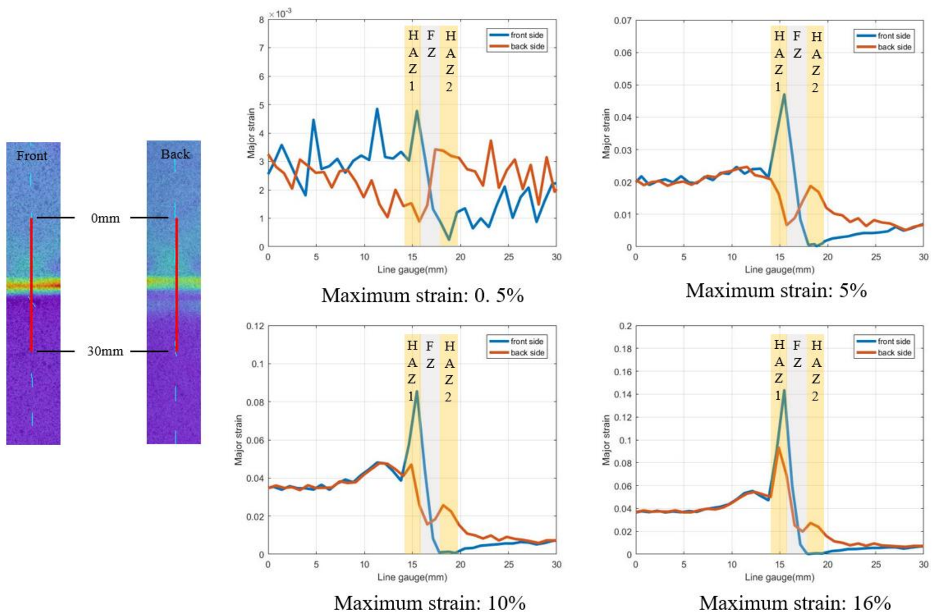

Figure 5.9 The spatial distribution of major strains across the weld seam at different maximum strain levels of 0.5%, 5%, 10% and 16%.

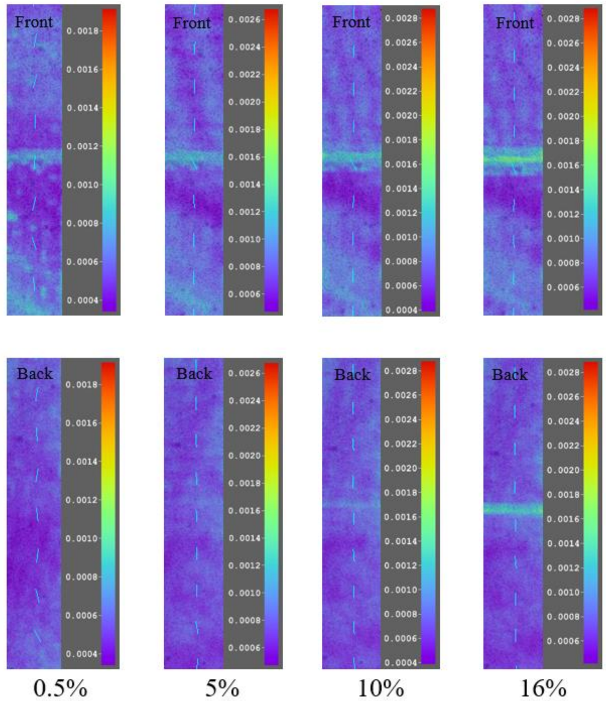

Figure 5.10 Full-field standard deviation of major strains distribution on the front and back sides of the tensile specimen at different maximum strain levels of 0.5%, 5%, 10% and 16%.

5.3.5 Effect of bending in tensile tests

A moderate bending moment is generated in dissimilar thickness TWBs due to their inherent imbalance, as shown in figure 5.11. With reference to the Figure, the sign and magnitude of the individual bending moments M_1 and M_2 is indeterminate and depends on several factors such as sample geometry and material properties, but the total (M_1 + M_2) must be equal to the tensile load P multiplied by half of the thickness difference (in this case 0.2 mm). In the elastic field, therefore, a zero-mean normal strain distribution is superimposed on the TWB's cross section. In order to effectively use tensile tests to characterize the HAZ, the effect of this phenomenon on the samples' surface strains must be considered.

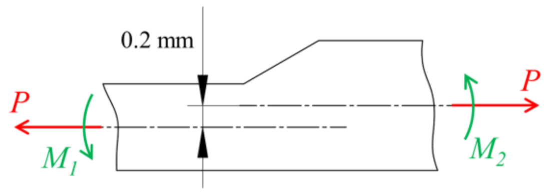

Figure 5.11 Section of TWB specimen with internal loads.

The bending moment causes a slight out-of-plane rotation of the gage portion of the blanks. The DIC setup shown in Figure 6 can be used to characterize the out-of-plane displacement and rotation of the specimens. For this purpose, a virtual gauge length of 50 mm located at the center line of the sample is selected to observe the spatial distribution of the out-of-plane displacement at different instants during a representative tensile test. The results are shown in figure 5.12. Clear differences can be observed between out-of-plane displacements in the thin portion (0-25 mm) and in the thick portion (25-50 mm). Notably, the inflection point remains stable at the weld seam throughout the duration of the test. As the tensile test progresses, the rotation in the HAZ increases, and differences in the magnitude of the out-of-plane displacement between the front and back surfaces become more pronounced.

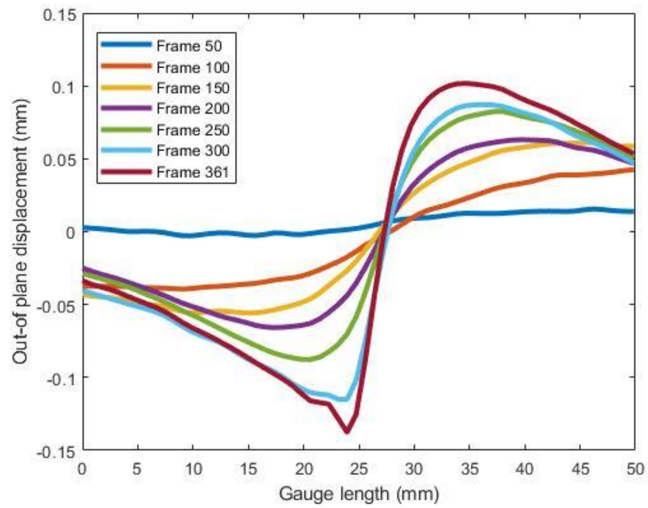

Figure 5.12 Spatial distribution of out-of-plane displacement at different times during tensile tests.

<u>5.3.6 Tensile behavior in HAZ</u>

To further investigate the tensile behavior in the HAZ with thickness gradient, a virtual rectangular gauge covering HAZ 1 of the specimen's front and back surfaces was selected. The evolutions of average major strains and the engineering stress-strain curves within these regions are depicted in figure 5.13(a). Throughout the entire tensile test, higher average principal strain in the HAZ 1 was observed consistently on the front surface than on the back surface. The maximum major strain reaches 0.148 on the front side of HAZ 1 and 0.098 on the back side. Similarly, the engineering stress-strain curves for the HAZ 1 on the front and back surfaces exhibit differences due to variations in strain evolution. However, neither the stress-strain curve on the front surface nor the back surface can truly reflect the actual tensile response of HAZ 1, due to the mismatch between the actual stress and the nominal stress caused by stress concentration. An indication of such deviation is that the apparent Young's modulus calculated based on the stress-strain curves of both front and back surfaces of the HAZ are 121GPa and 381GPa, respectively, which do not fall within the typical elastic modulus range of steels (190-215GPa). With reference to the stress-strain curve, the yield point of the front and rear surface HAZ was found. As shown in figure 5.13(b), plastic instability is first observed in the HAZ on the front surface, aided by the superimposed tensile stress deriving from the out-of-plane bending of the sample. The plastic zone then gradually propagates towards the back surface of the specimen, and global yielding ensues. The calculated apparent yield stress of the front and rear HAZ is 744 MPa and 1014 MPa, respectively.

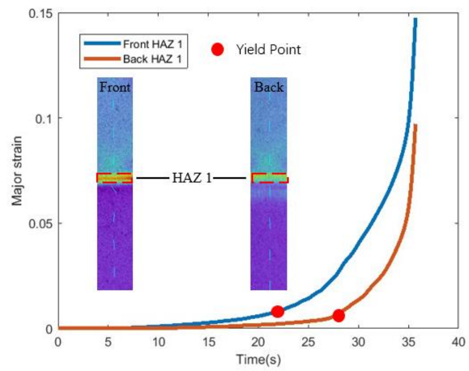

(a)

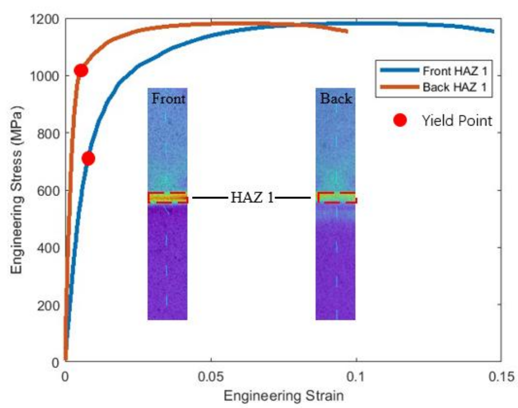

(b)

Figure 5.13 Tensile behaviors in HAZ: (a) Major strains history; (b) Engineering stress-strain curves.

The potential generation of triaxial stresses in the HAZ and in the adjacent areas can also affect the stress-strain behavior of the material near the centerline of the specimen. Two main sources of stress triaxiality can be observed: (1) The relatively abrupt change in cross section thickness and consequent stress concentration can cause localized three-dimensional stresses, evident when drawing the tensile stress lines for TWB specimens. (2) Triaxial stresses may appear at or near the interfaces between areas with different mechanical properties (i.e. heat-unaffected material to HAZ to weld seam). For example, the displacement of the HAZ is partially constrained by the displacement of the heat-unaffected portion on one side, and by the displacement of the weld seam on the other. This effect is more pronounced due to the discussed bending loads in the gage portion of the specimens.

Stress triaxiality in the HAZ can cause a potential increase in the maximum principal stress and a reduction in maximum shear stress just below the sample's surface, thereby affecting the measured strains (although this effect would be negligible when compared to the effect of the bending moment as described in the previous section) and promoting the onset of brittle fracture. While not the focus of this study, this is an interesting point that needs to be investigated in future works on TWB specimens.

5.3.7 A novel approach to calibrate stress-strain curves in HAZ with uneven thickness

To accurately determine the material properties in HAZ with uneven thickness during tensile test, it is essential to correct the stress-strain curve. As discussed in the previous section, the front and back surfaces within the HAZ exhibit slightly different tensile behaviors, caused in part by the bending moment acting on the gage portion of the specimens. Due to the difficulty of directly measuring the actual stress in the HAZ on its front and back surfaces, we propose to obtain the nominal strain under nominal stress to enable the correction of the surface derived stress-strain curves. Figure 5.14 is a schematic illustration of the proposed method. A multiple linear regression model is established, and the effect of the bending moment on the strain measurement in the HAZ is mitigated by the-facto averaging the strains on the tensile side with those on the compressive side of the curvature, thus achieving the desired correction of the specimen's true stress-strain curve. The specific steps for the calibration process are decribed as follows:

1) Obtain the strain history on the front and back surfaces of the uniaxial tensile specimen.
2) Determine the size and location of the HAZ: the location and size of the HAZ can be determined by microhardness tests since the mechanical properties of the FZ, HAZ and base materials are significantly different.
3) Calculate the Young's modulus of the HAZ based on nanoindentation test results using Eq. 3.
4) Calculate the nominal strain in the HAZ within the elastic deformation region using Hooke's law.
5) Apply a multiple linear regression model of nominal strain on the front and back surfaces of the specimen to calculate the true stress-strain material response:

   Assume that the output variable nominal strain is a function of the predictor variables (i.e., front surface strain and rear surface strain), and its multiple linear regression model is as follows:

$$\varepsilon_n = \beta_0 + \beta_1 \varepsilon_f + \beta_2 \varepsilon_b + e \tag{5.4}$$

Where, β_0 is a constant term; β_1 and β_2 are partial regression coefficients; ε_f and ε_b are the front and back surface strains; and e is a random error.

One of the estimation methods is the least squares method to minimize the sum of squares of the residuals:

$$\arg min \sum_{i=1}^{m}(\varepsilon_n^i - (\beta_0^i + \beta_1^i\varepsilon_f^i + \beta_2^i\varepsilon_b^i))^2 \tag{5.5}$$

6) Calibrate the stress-strain curve: the nominal strain in the plastic phase is predicted based on the multiple linear regression model of the elastic phase. The mechanical parameters of the HAZ are identified based on the calibrated stress-strain curves.

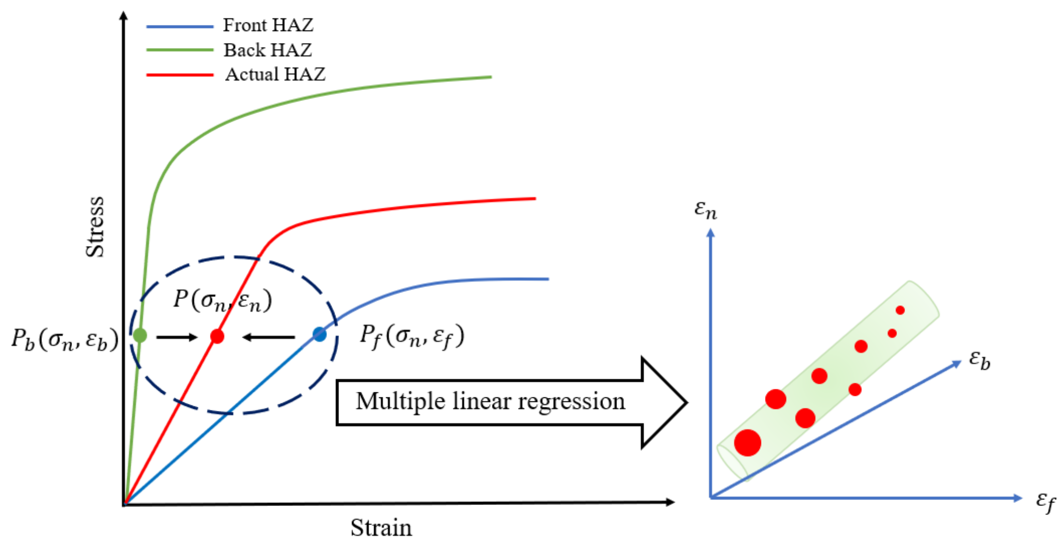

Figure 5.14 The schematic of the proposed stress-strain curve calibration method.

To determine the significance of a multiple linear regression model, the coefficient of determination, R^2, is typically calculated in Equation 8. R^2 represents the proportion of the variance in the dependent variable that is predictable from the independent variables. Typically, R^2 ranges from 0 to 1, with values closer to 1 indicating that the regression predictions are closer to the actual values, suggesting a more accurate regression model.

$$R^2 = \frac{\sum_{i=1}^{m}(\widehat{\varepsilon_n^i} - \overline{\varepsilon_n})^2}{\sum_{i=1}^{m}(\varepsilon_n^i - \overline{\varepsilon_n})^2} \tag{5.6}$$

Applying the above-described approach to the DP1180 TWB tensile test in this study, the regression statistical analysis of the nominal strain, front surface strain and back surface strain in the elastic stage is performed as shown in figure 5.15. The results of partial regression coefficient and coefficient of determination are shown in Table 5.1. The coefficient of determination of approximately 1 indicates that there is a strong linear relationship between the nominal strain and the front and back surface strain. In addition, the values of β_1 and β_2 are both close to 0.5, highlighting that the effect of a pair of additional tensile and compressive strains of equal magnitude and opposite directions generated by the bending moment can be almost eliminated. Major strain evolution curves and stress-strain curves in HAZ 1 are corrected according to the regression model and shown in figure 5.16.

The Young's modulus, yield strength, and tensile strength of the HAZ 1 extracted from the stress-strain curves before and after corrections were compared. To validate the accuracy of the proposed method, yield strength and tensile strength estimated from micro-hardness were used as references for validation. The comparison results of the two methods are shown in Table 5.2, showing that the yield strength and tensile strength are in good agreement with the estimated values though slightly higher.

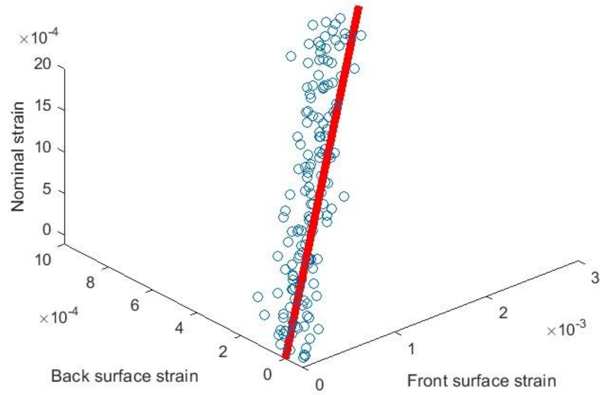

Figure 5.15 The regression statistical analysis of the nominal strain, front surface strain and back surface strain in the elastic stage.

Table 5.1 The results of partial regression coefficients and coefficient of determination.

β_0	β_1	β_2	R^2
-4.2×10^{-5}	0.47	0.53	0.989

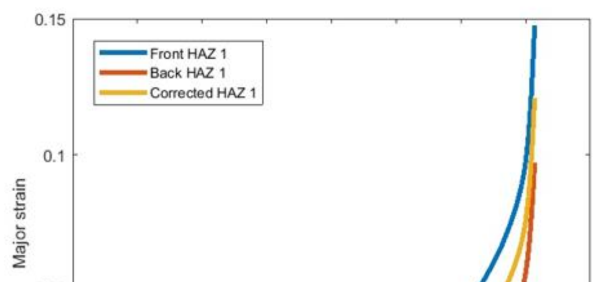

(a)

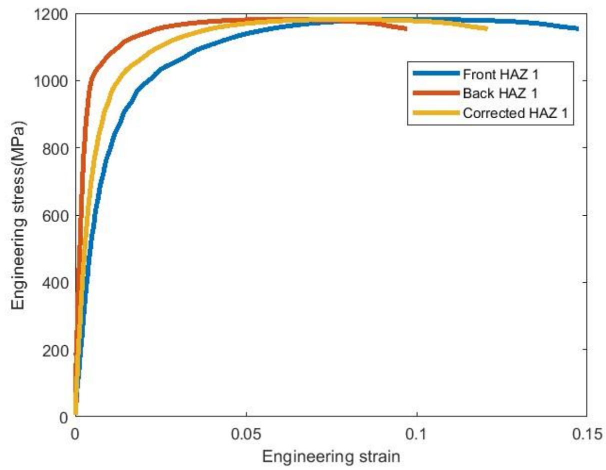

(b)

Figure 5.16 (a) Corrected major strain evolutions; (b) Corrected engineering stress-strain curves in HAZ 1.

Table 5.2 Comparison of Young's Modulus, yield strength and tensile strength.

	Young's modulus	Yield strength	Tensile strength
Front surface HAZ	130 GPa	744 MPa	1134 MPa
Back surface HAZ	381 GPa	1014 MPa	1134 MPa
Corrected HAZ	208 GPa	758 MPa	1134 MPa
Micro-hardness test	-	723 MPa	1002 MPa

5.4 Summary

This chapter addressed a practical but often overlooked challenge in tensile characterization of TWBs with dissimilar sheet thicknesses: the presence of a thickness step introduces an eccentric load path and produces bending and non-uniform stress/strain states in the gauge section. As a result, conventional practice—constructing a "local" HAZ stress–strain curve by combining nominal stress with the surface strain measured on only one face—can yield biased and even nonphysical material responses. The central goal of this chapter was therefore to establish an experimental methodology to recover a tensile response of the HAZ under such geometric and material inhomogeneity.

To achieve this goal, the chapter developed a combined indentation–tensile framework. Microhardness testing was used to identify the spatial extent of the FZ and HAZ. Nanoindentation was performed to determine the elastic modulus in the HAZ with high spatial resolution, supplying a reliable modulus baseline for subsequent constitutive calibration. Building upon these localized measurements, uniaxial tensile tests were carried out with a four-camera double-side DIC system, enabling synchronized full-field strain measurements on both the front and back surfaces, as well as thickness/topography information in a unified coordinate system. Compared to a conventional single-side stereo DIC arrangement, the dual-side configuration is essential here because it directly reveals the front/back strain asymmetry that originates from bending, rather than implicitly assuming a uniform through-thickness response.

As the core methodological contribution, the chapter introduced a regression-based calibration strategy to reconstruct a representative (nominal) HAZ strain from dual-side measurements. In the elastic regime, the nominal strain implied by Hooke's law (using the indentation-derived Young's modulus) was treated as the target response, while the simultaneously measured front- and back-surface strains in the HAZ were used as predictors. A multiple linear regression model was then established to link the nominal strain to the dual-side surface strains. The resulting coefficients naturally acted as physically interpretable weights: because bending produces opposite-sign strain contributions on the two faces, combining the two strains with near-symmetric weights suppresses bending effects. After determining the regression coefficients, the same relationship was used to predict the nominal strain throughout loading, thereby enabling construction of a corrected HAZ stress–strain curve. The corrected curve recovered a physically reasonable modulus and yielded yield/tensile strength values consistent with the relative strength trends inferred from hardness mapping.

Finally, several limitations and future directions were identified. The regression model assumes that the relationship between nominal strain and dual-side surface strains is well approximated as linear (particularly in the elastic regime used for calibration. Moreover, direct validation of the corrected HAZ curve is inherently difficult for dissimilar-thickness TWBs because stress concentration and bending cannot be fully eliminated; future work should therefore include complementary experiments on same-thickness welded coupons or alternative specimen designs that minimize eccentricity, enabling more direct validation of the calibrated constitutive response. Despite these limitations, the results in this chapter establish a clear pathway to obtain physically meaningful HAZ stress–strain curves in challenging TWB configurations and further highlight the broader utility of multi-camera double-side DIC for material characterization problems where through-thickness effects cannot be neglected.

CHAPTER SIX

LASER-LIGHT SPECKLE DIC FOR DISPLACMENT AND STRAIN MEASUREMENT

6.1 Introduction

Since the discovery of laser speckle in the early era of coherent optics, speckle-based metrology has developed into a broad family of non-contact measurement techniques for displacement, strain, and related physical fields. In experimental mechanics, DIC has become one of the most widely adopted full-field methods by treating surface speckles as information carriers and tracking their motion between reference and deformed images. The achievable accuracy and robustness of DIC strongly depend on the quality and characteristics of the speckle pattern, including contrast, randomness, and stability under illumination changes and deformation.

From the standpoint of illumination and pattern formation, DIC implementations can be broadly divided into white-light speckle DIC and laser-light speckle image correlation. White-light speckle DIC typically uses painted or printed stochastic textures, which are largely viewpoint-independent and therefore well suited for stereo/3D measurements and large-deformation tracking. Laser-light speckle correlation, in contrast, relies on coherent illumination of a rough surface, producing high-contrast speckles without requiring surface coating, and allowing optical control of speckle size through system parameters such as aperture [62-63]. Despite their shared correlation framework, these two approaches often exhibit markedly different performance envelopes in practice. Laser-light speckle correlation is attractive for applications where coating is undesirable (e.g., high-temperature environments, microscale tests, or delicate surfaces) [64-66], while white-light DIC remains the most robust choice for large motions, large deformations, and routine stereo 3D measurements. A central reason is decorrelation: under rigid-body motion or deformation, the phase/amplitude distribution of laser speckles can change such that original speckles vanish and new speckles form, degrading correlation quality and ultimately causing correlation loss.

Motivated by these practical tradeoffs, this chapter consolidates recent advances and provides a structured comparison of laser-light and white-light speckle correlation in terms of speckle formation, measurement accuracy, measurable range, and robustness, using both literature evidence and benchmark experiments. In particular, the chapter highlights a synchronized rigid-body micro-translation test in which the raw displacement error of laser speckle correlation is noticeably higher than that of white-light DIC ($\approx$ 3.5% vs $\approx$0.29%), while a simple linear calibration reduces the laser-speckle error to $\approx$ 0.59% and brings performance closer to white-light DIC. At small displacement gradients, both approaches show comparable accuracy when referenced to holographic interferometry, and in uniaxial tensile tests the total strain and elastic modulus measured by laser speckle correlation remain close to those obtained by white-light DIC (within ~2% for total strain and ~3.5% for modulus).

6.2 Generation and characteristics of laser-light speckle

6.2.1 Laser-light speckle pattern

Laser-light speckles are random interference patterns generated when a laser illuminates a rough surface. Laser-light speckles can be classified based on their generation mechanism and observation method as either objective speckles or subjective speckles. Objective speckles refer to speckle patterns formed in free space after a laser beam illuminates a rough surface. As shown in figure 6.1(a), when a laser beam strikes a rough surface, the microscopic irregularities on the surface cause phase differences in the reflected light waves. These light waves propagate through free space and interfere with each other, creating a random distribution of bright and dark spots known as objective speckles. The average objective speckle diameter is defined as [67]:

$$d_{obj} = \frac{2.4\lambda p}{D} \tag{6.1}$$

where λ is the laser wavelength, p is the distance from the surface to the imaging plane, and D is the diameter of the laser beam at the irradiated surface.

Subjective speckles refer to the speckle patterns formed on the image plane through an imaging system (such as a camera lens) after a laser illuminates a rough surface. As illustrated in figure 6.1(b), when a laser beam strikes a rough surface, the scattered light is collected by the imaging system and focused onto the image plane. On the image plane, the light waves interfere with each other, resulting in a random speckle pattern. The average subjective speckle diameter is defined as:

$$d_{sub} = \frac{2.4\lambda f}{A} \tag{6.2}$$

where f is the focal length of the imaging system and A is the diameter of the aperture.

Compared with objective speckles, subjective speckles usually have higher contrast because the imaging system can effectively collect and focus scattered light, enhancing the difference between light and dark in the speckle pattern. In addition, subjective speckle characteristics, such as size and contrast, can be precisely controlled by adjusting optical system parameters such as aperture size and focal length. Therefore, most of the current research focuses on subjective speckles.

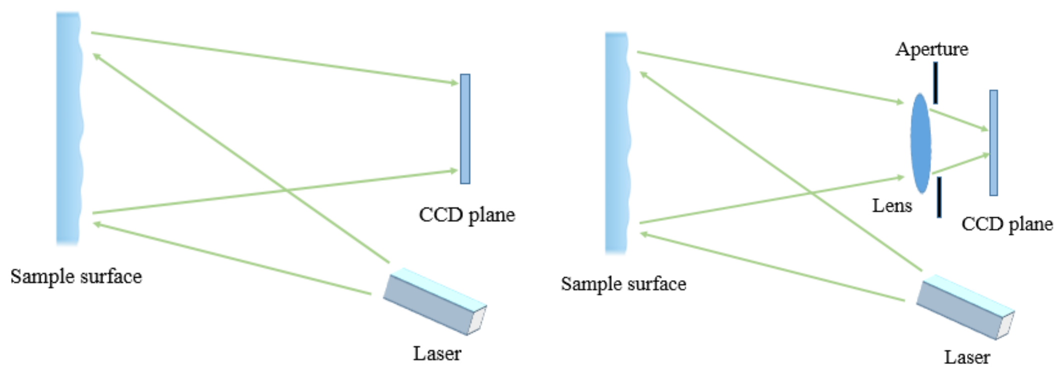

(a) (b)

Figure 6.1 Generation of laser-light speckle: (a) Objective speckle; (b) Subjective speckle.

6.2.2 Optimization of laser-light speckle quality

Usually, laser-light speckle is controlled by optical device parameters (such as aperture size, laser power, etc.), and its quality directly affects the measurement accuracy of DIC method. Therefore, it is necessary to set appropriate optical device parameters to produce high-quality speckles by evaluating the quality of laser-light speckles. In this study, the open-source software Glare was utilized to assess laser-light speckle quality from four aspects: speckle coverage, speckle size, systematic error, and random error [68].

(1) Speckle coverage

Speckle coverage refers to the ratio of the speckle area to the entire image area. A coverage of 50% is generally considered optimal.

(2) Speckle size

Speckle size refers to the pixel value occupied by each speckle particle. The optimal speckle size is 3-5 pixels.

(3) Systematic error

The systematic error refers to the bias caused by the interpolation operation when the DIC algorithm performs sub-pixel matching. Its mathematical expression is:

$$u_e \approx Csin\,(2\pi u_0) \tag{6.3}$$

where u_e represents the interpolation bias, u_0 represents the sub-pixel translation, C represents amplitude of the interpolation bias.

(4) Random error

Random error refers to the error in measurement results caused by image noise. The zero-order and first-order shape function random errors can be expressed as:

$$Std(u) = \frac{\sigma}{\sqrt{\sum_{m=-M}^{M}\sum_{n=-M}^{M} f_x^2(m,n)}} \tag{6.4}$$

where u represents the measured displacement, σ represents the standard deviation of image noise, $f_x(m,n)$ represents image gradient along the x axis at point (m,n).

In this chapter, three important optical device parameters that affect the speckle quality are considered: camera aperture (affects the amount of incident light), beam expander (affects the speckle magnification) and laser power (affects the speckle intensity). The subset size in the software is 31×31 pixels, and each subset contains 3-5 speckle dots to achieve reliable correlation calculation results.

(1) Camera aperture

Four different aperture values (f/4, f/8, f/16, f/32) were set, with a beam expander magnification of 40X and a laser power of 0.1W. The laser speckle image and quality assessment results are shown in figure 6.2. It can be observed that as the aperture decreases, the speckle size gradually increases, leading to an increase in speckle coverage. Simultaneously, both systematic and random errors tend to decrease. Therefore, reducing the camera aperture can effectively improve the quality of the laser speckle. It is worth noting that reducing the camera aperture will reduce the brightness of the image, which needs to be compensated by increasing the exposure time. In this experiment, an aperture of f/32 was selected as it achieved the optimal levels of speckle coverage and speckle size, resulting in the lowest systematic and random errors.

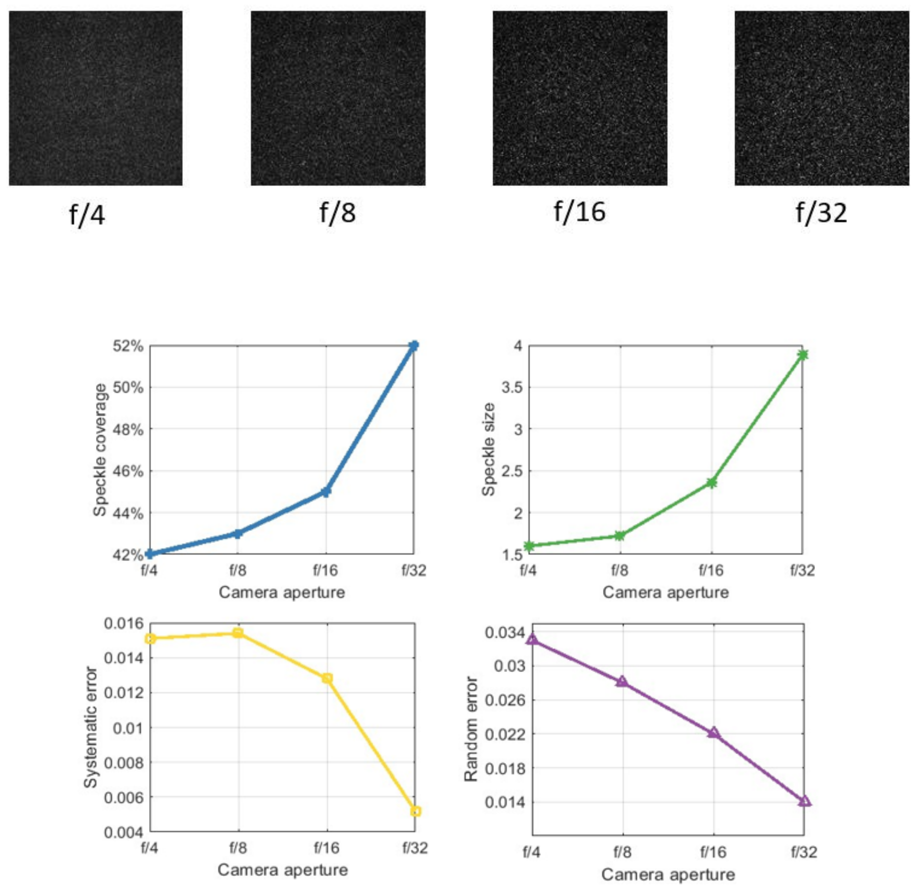

Figure 6.2 Laser speckle patterns at different apertures and quality assessment results.

(2) Beam expander

Four different collimating lens magnifications (10X, 20X, 40X, 60X) were set, with an aperture value of f/32 and a laser power of 0.1W. Figure 6.3 shows the laser speckle images and quality evaluation results. It can be observed that the speckle coverage at 10X is only 26%, primarily because the magnification is too low, resulting in insufficient laser speckle coverage over the entire field of view. As the magnification increases, the speckle coverage gradually improves to around 50%. For the speckle size, the systematic and random errors fluctuate slightly but are not significantly different. Based on the four speckle evaluation parameters, 40X or 60X beam expander is suitable choices.

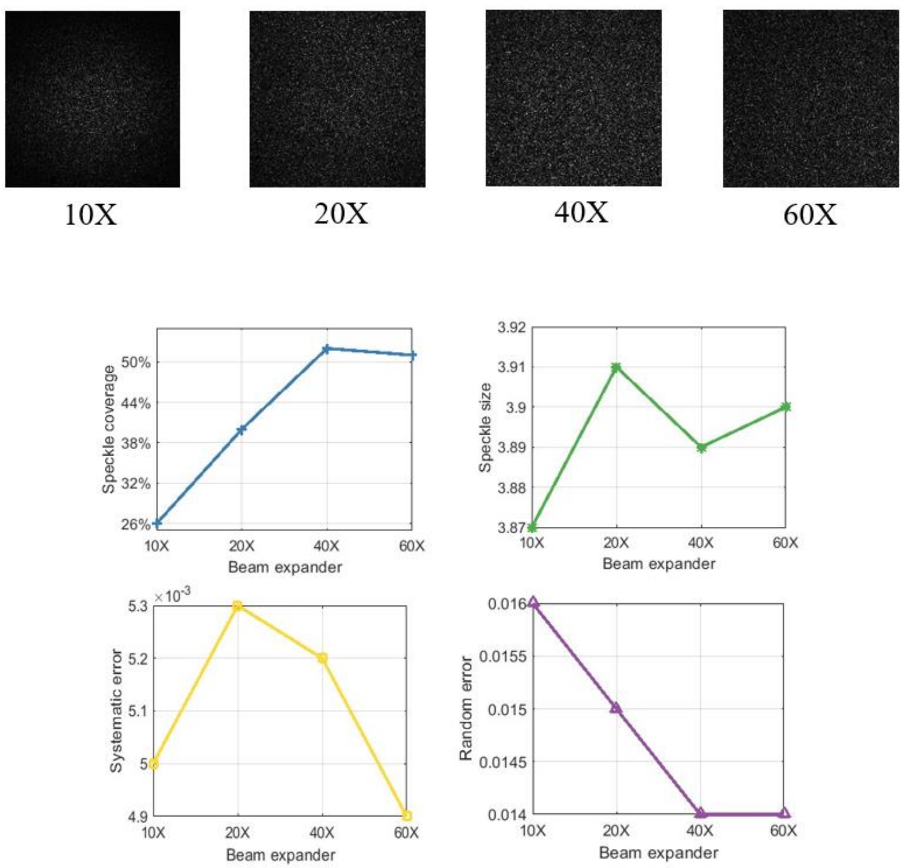

Figure 6.3 Laser speckle patterns at different beam expander and quality assessment results.

(3) Laser power

Four different laser powers (0.1W, 0.3W, 0.5W, 0.7W) were set, with an aperture value of f/32 and a collimating lens magnification of 40X. The laser speckle images and quality assessment results are shown in figure 6.4. It can be seen that as the laser power increases, the white speckle particle area increases significantly. The speckle coverage and speckle size in the image increase accordingly. Especially at 0.7W power, local areas of the image are already overexposed, and the speckle coverage and speckle size reach 68% and 5.1pixel respectively. However, random error decreases significantly with increasing laser power, as the image gradient increases and is inversely related to random error. Therefore, considering all factors, a laser power of 0.5W is the most suitable.

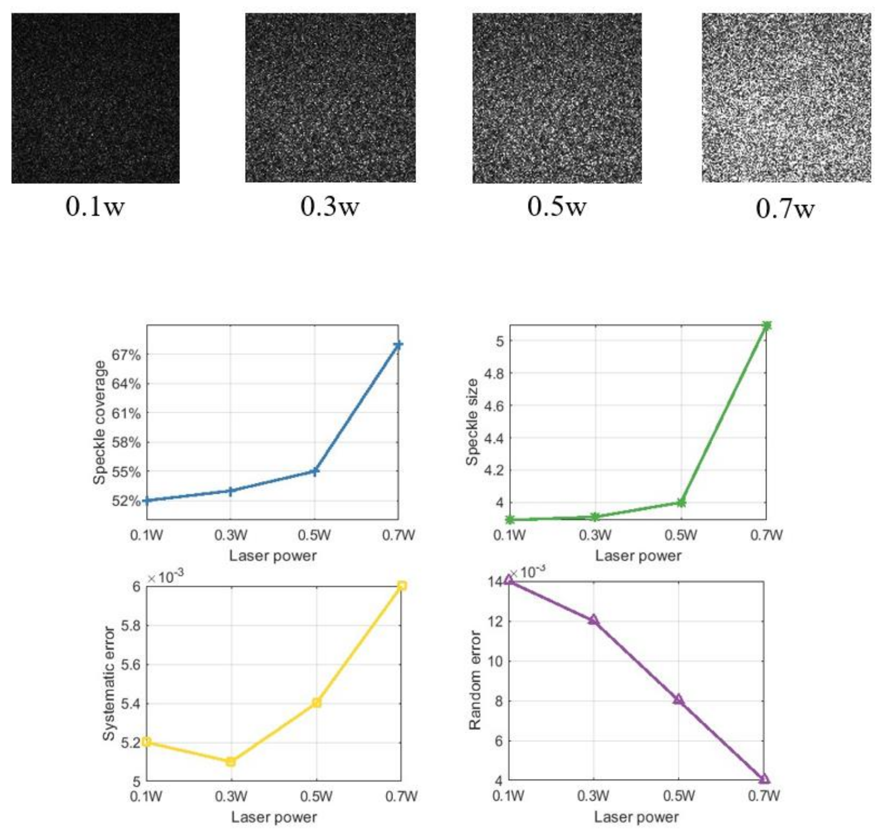

Figure 6.4 Laser speckle patterns at different laser power and quality assessment results.

Smaller apertures (down to f/32) increased speckle size and coverage, reducing errors but requiring longer exposure times. Beam expanders with higher magnifications (40X, 60X) provided better speckle coverage (~50%) without significant error changes. Laser power affected speckle coverage and size, with 0.5W providing the optimal balance. Excessive power (0.7W) caused overexposure, while increasing power generally reduced random error due to higher image gradients. The optimal settings for speckle quality were f/32 aperture, 40X magnification, and 0.5W laser power. It should be noted that the optimal parameters depend on different experimental conditions.

6.3 Experiment for displacement and strain measurement

6.3.1 Decorrelation

The core of DIC technology is displacement measurement, and its accuracy can reach 0.01-0.1 pixels for in-plane displacement measurements and about 0.1 pixels for out-of-plane displacement measurements. As the carrier for displacement computation, the speckle pattern plays an important role in measurement quality. A synchronized rigid-body translation experiment was conducted, as illustrated in figure 6.5, to compare the performance of laser-light and white-light speckle patterns for displacement measurements. A flat metal specimen was mounted on a micro-displacement platform. The left region of the specimen was coated with painted speckles, while the right region was illuminated by a coherent laser (wavelength: 532 nm) projected onto the surface to generate laser-light speckle patterns. A white plate was placed in the expanded laser beam path to prevent the left side of the sample from being illuminated by the laser. The average size of the white-light speckles was approximately 4 pixels, and the laser-light speckle size was adjusted by the aperture and beam expander to achieve comparable dimensions. The micro-displacement platform has a displacement of 25.4μm per step, and the experiment used a total of 50 steps. For both methods, the subset size was set at 21×21 pixels. The full-field displacement results after DIC evaluation are shown in figure 6.6. From these results, two conclusions can be intuitively obtained: (1) the measured displacement from laser-light speckles is consistently larger than that from white-light speckles, and (2) the regions of missing data in the laser-light speckle displacement map increase with increasing displacement, eventually leading to complete loss of measurable area. These effects are attributed to a phenomenon known as speckle decorrelation, in which rigid-body motion or deformation alters the speckle phase and amplitude distribution, causing original speckles to vanish and new ones to form [69-71]. Due to the change in the speckle shape and size, the correlation between the reference speckle pattern and the target speckle pattern decreases or even becomes completely uncorrelated, which seriously affects the measurement accuracy. To quantitatively assess the measurement precision of the laser-light speckle, figure 6.7 presents a comparison between the average DIC-measured displacement (from both speckle types) and the true displacement from the translation stage, prior to complete decorrelation. The results show that laser-light speckle measurements exhibit a general increased error trend, with an average error of 3.5% per step. In contrast, white-light speckles maintain stable performance, with an average error of only 0.29% per step.

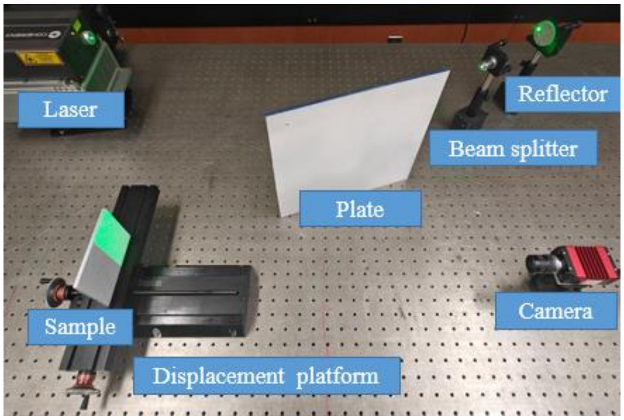

Figure 6.5 Experimental setup for displacement of laser-light speckle and white-light speckle.

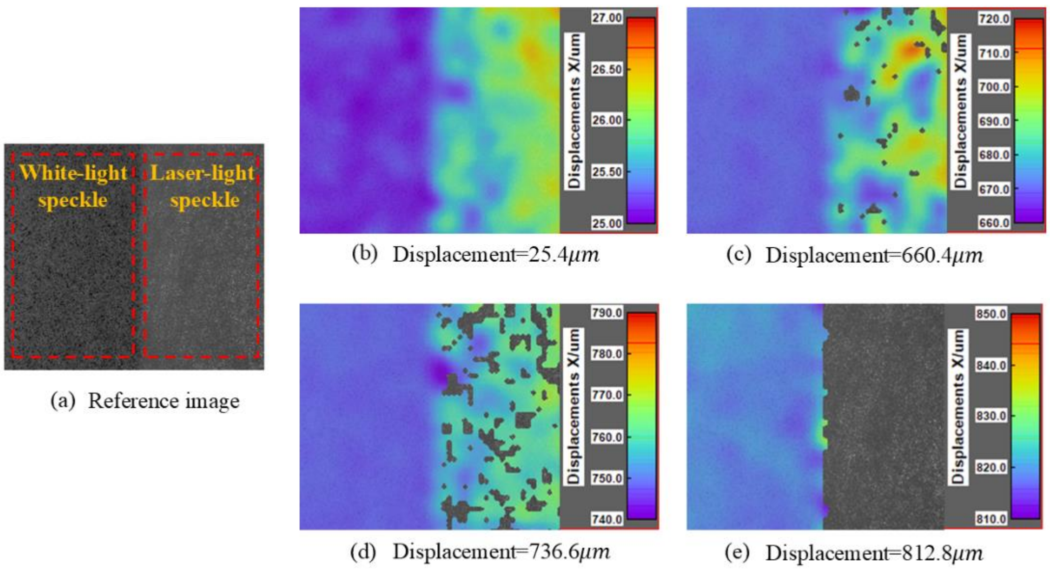

Figure 6.6 Full-field displacement results of laser-light speckle and white-light speckle.

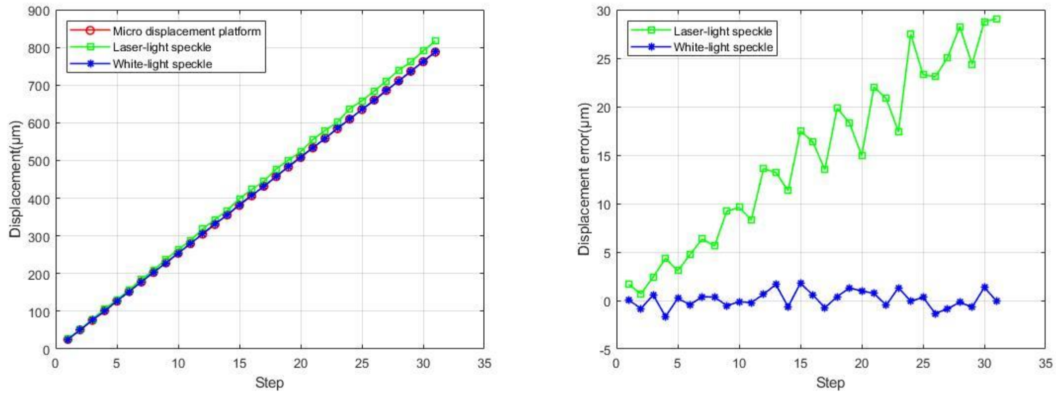

(a) (b)

Figure 6.7 (a) Average displacement results; (b) Displacement errors relative to the micro-displacement platform.

<u>6.3.2 Solutions for decorrelation</u>

The decorrelation issue has long been the primary challenge in the application of laser-light speckle DIC. This issue can be divided into two categories: (1) increased measurement error resulting from correlation degradation during small-displacement measurements; and (2) complete decorrelation that occurs under large displacements. A feasible approach to address the first problem is to calibrate the laser-light speckle DIC system and compensate for the displacement error. As shown in figure 6.8, the error curve exhibits a near-linear growth trend. Therefore, linear fitting can be applied to calibrate the system and correct the measured displacements. After calibration, the average error per step is reduced to 0.59%, representing an 83% reduction compared to the average error before fitting. Performance after calibration is also similar to that of white-light speckle DIC. In addition, Kobayashi and Paris both proposed feedback compensation methods [72-73]. By actively tracking the target displacement to drive the compensation stage to move, the speckle correlation coefficient after the compensation strategy is always greater than 0.99, and the measurement error is smaller than 0.7% and within the range of ±1 mm.

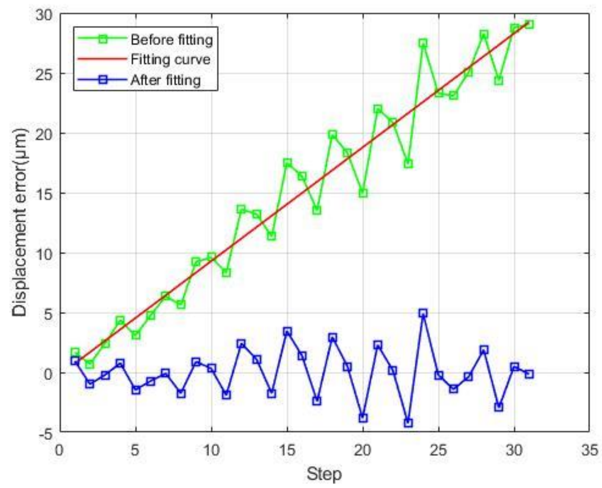

Figure 6.8 Laser-light speckle displacement error compensation by linear fitting.

For large displacement measurements, a typical strategy is to replace sequential correlation analysis with incremental correlation analysis [74] as shown in figure 6.9(a). In classic sequential correlation analysis, an image is recorded before loading as the reference image (image 0), then each image during the loading process (image 1, 2, 3, ...) is correlated with the reference image to obtain displacement information. In contrast, the incremental correlation method performs correlation between consecutive frames: Image 0 is correlated with Image 1, Image 1 with Image 2, Image 2 with Image 3, and so on. In this approach, the reference image is not fixed, but is continuously updated. By decomposing a large displacement into a series of smaller steps, this method significantly reduces the likelihood of decorrelation between the reference and deformed images. As shown in figure 6.9(b), the right region of the specimen containing laser-light speckles can be fully tracked using the incremental approach.

Although incremental DIC has become a very promising method to solve the decorrelation problem, the error of each correlation calculation will continuously accumulate and be transmitted to the final measurement result. As shown in figure 6.10, the measurement error after using incremental correlation is significantly greater than that after using sequential correlation. To address this problem, Pan et al. proposed an adaptive reference image update method [75]. This method first sets a seed point in the initial reference image and tracks the displacement of the point in the deformed image. If the calculated correlation coefficient is higher than the preset threshold (indicating that there is no significant decorrelation between the images), the conventional DIC method is directly used to calculate the full-field displacement. When the calculated correlation coefficient is lower than the threshold (significant decorrelation occurs between surface images), the system will automatically update the reference image to the last valid image before the current deformation and use the updated reference image as the benchmark for subsequent displacement analysis. By calculating the incremental displacement frame by frame and accumulating it, the overall displacement of the specimen is finally obtained. Zhang et al. proposed an improved calculation scheme composed of incremental DIC with the nearest integer pixel offset and Gaussian pre-filtering [76]. First, the speckle image was filtered before DIC analysis using a Gaussian low-pass filter to smooth the image noise and improve correlation calculation stability. Then, when updating the reference image, the subset center point was offset from the sub-pixel position to the nearest integer pixel position to avoid error introduced by sub-pixel interpolation. This step eliminates the cumulative error caused by sub-pixel interpolation in traditional incremental DIC.

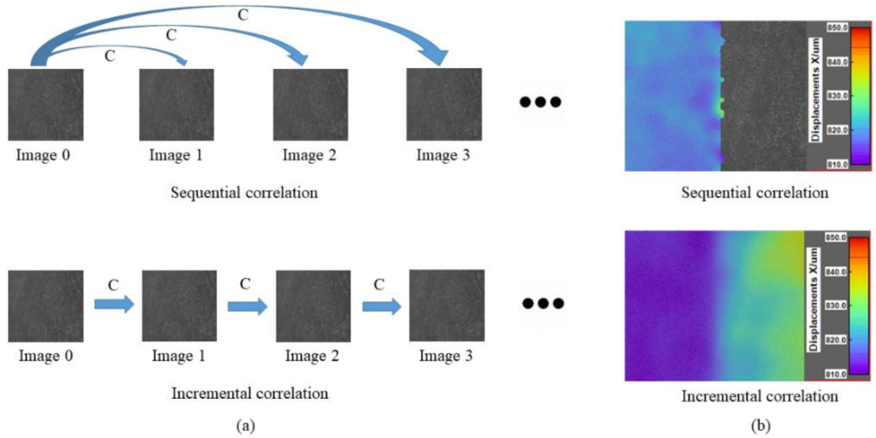

Figure 6.9 Comparison of sequential and incremental correlation.

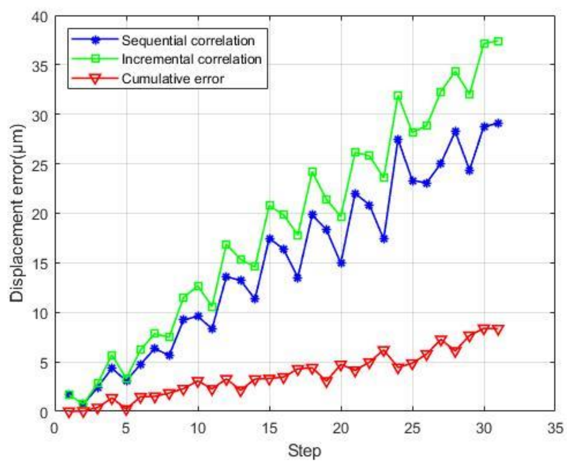

Figure 6.10 Cumulative error generation in the incremental correlation.

6.3.3 Small displacement gradient measurement

An experimental setup, shown in figure 6.11, was developed to further evaluate the measurement accuracy of laser-light speckle DIC under small displacement conditions. A circular aluminum plate was used as the test specimen, and submicron to micron-scale displacement gradients were introduced using a threaded knob. A holographic speckle interferometry system was employed as a reference for comparison, as it typically provides higher accuracy than DIC in submicron displacement measurements. The interferometer uses infrared laser illumination (wavelength: 780nm) and a dual-arm illumination system to achieve horizontal (x) and vertical (y) displacement measurements. Figure 6.12 presents the full-field vertical displacement for the circular plate measured by holographic speckle interferometry, laser-light speckle DIC, and white-light speckle DIC, respectively. A smooth and continuous horizontal displacement gradient is observed across the disk, ranging approximately from –6 μm to +7 μm. To enable a more precise comparison, a 120 mm horizontal line, labeled AB in Figure 13, was selected along the diameter of the plate to extract the spatial displacement profiles obtained by the three methods. Figure 6.13(a) shows the measured displacements, while figure 6.13(b) presents the average percentage error of laser-light speckle DIC and white-light speckle DIC compared to the holographic measurement in segmented regions (0–20 mm, 20–40 mm, ..., 100–120 mm). The results indicate that, under small displacement conditions, laser-light speckle DIC and white-light speckle DIC exhibit very similar error values. However, the error increases progressively toward the central region of the gauge line (40–80 mm), where the displacement magnitude lies between approximately –2 μm and +2 μm. Considering that the spatial resolution of the camera is 110 microns/pixel, the displacement magnitude is close to 0.01 pixels, which is the best achievable accuracy for DIC in-plane displacement measurement. Table 3 compares the displacement measurement performance of laser-light speckle and white-light speckle.

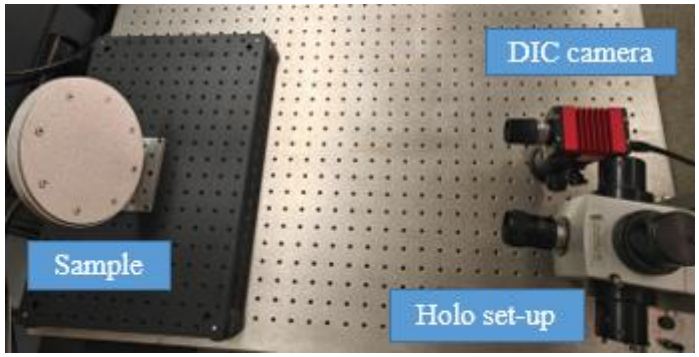

Figure 6.11 Experimental set-up for small displacement gradient measurement.

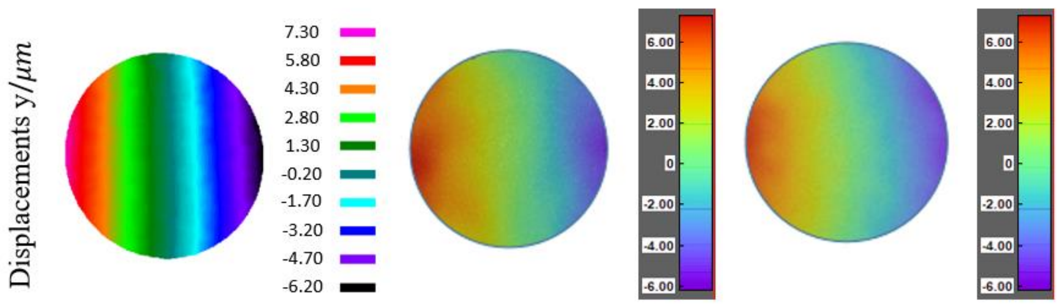

(a) (b) (c)

Figure 6.12 Full-field vertical displacement measurement results: (a) Holography; (b)Laser-light speckle DIC; (c) White-light speckle DIC.

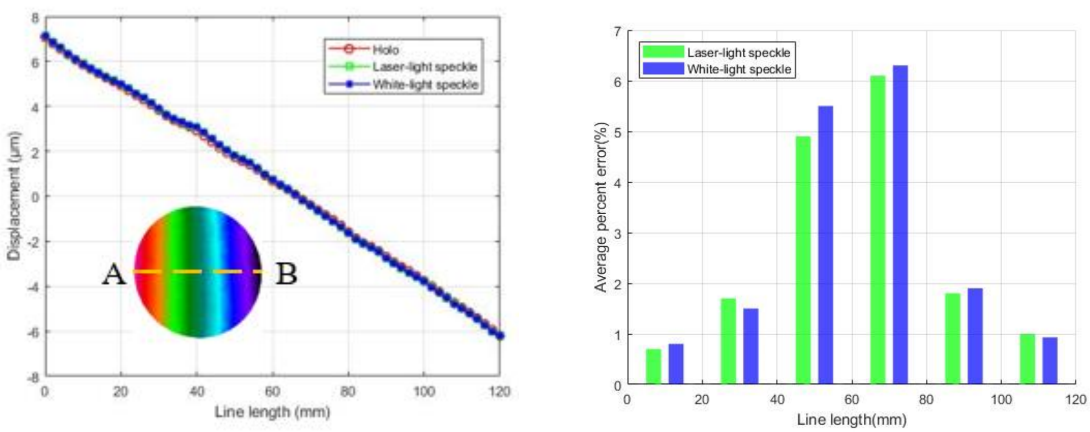

(a) (b)

Figure 6.13 (a) Spatial displacement distribution along the 120mm gauge line; (b) Average percent error relative to the holography.

Table 6.1 Displacement measurement performance of laser-light speckle and white-light speckle.

Category	Laser-light Speckle	White-light Speckle
Measurement Range	Narrow, 0.01pixel-2speckle diameters pixel. Incremental calculation is required to increase the measuring range.	Wide, no incremental calculation required.
Measurement Accuracy	Lower than white-light speckle. Compensation measures are needed to reduce errors.	High, 0.01-0.1pixel.
Correlation Robustness	Low, decorrelation beyond 1-2 speckle diameters.	High, almost no limitation for rigid body displacement
Out-of-plane displacement	Difficult, cannot be achieved with multiple cameras.	Easy, can be achieved with multiple cameras.

6.3.4 Out-of-plane displacement measurement

The most common approach for measuring out-of-plane displacement using DIC is to employ a stereo vision system with two cameras. Such a system enables three-dimensional displacement reconstruction based on the principle of triangulation. This method has been widely adopted in white-light DIC systems. However, laser-light speckle patterns are highly dependent on the viewing angle. As a result, the two cameras in a stereo configuration observe completely different speckle patterns due to their differing perspectives. As illustrated in figure 6.14, these different perspectives make it impossible to perform reliable stereo matching. This fundamental limitation significantly hinders the extension of laser-light speckle DIC to three-dimensional measurements

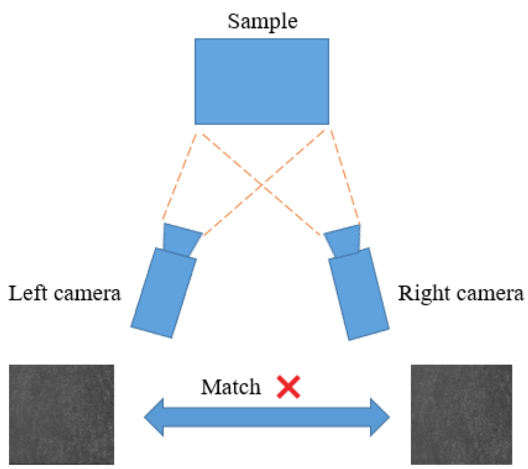

Figure 6.14 Failure of laser-light speckle dual camera matching.

6.3.5 Tensile test strain measurement

Accurate measurement of the deformation behavior of materials at room temperature is essential for understanding their elastic–plastic response, damage initiation, and fracture mechanisms. Laser-light speckle DIC has also demonstrated potential for use in deformation measurements. As shown in figure 6.15, laser-light speckle DIC and white-light speckle DIC were simultaneously employed on both sides of a DP980 specimen under uniaxial tensile loading using two independent 2D-DIC systems. Figure 6.16 presents the full-field principal strain distribution and the corresponding stress–strain curves obtained from both speckle types just prior to fracture. It can be observed that the total strain measured by laser-light speckle DIC is 2% higher, while the elastic modulus is 3.5% lower than that obtained using white-light speckles, indicating good overall agreement. It is noteworthy that laser-light speckle DIC also requires the use of incremental correlation to mitigate decorrelation effects during deformation. Furthermore, in large or rapid deformation scenarios, the camera acquisition rate must be appropriately selected to ensure that the inter-frame displacement remains within the measurable range of laser-light speckle DIC.

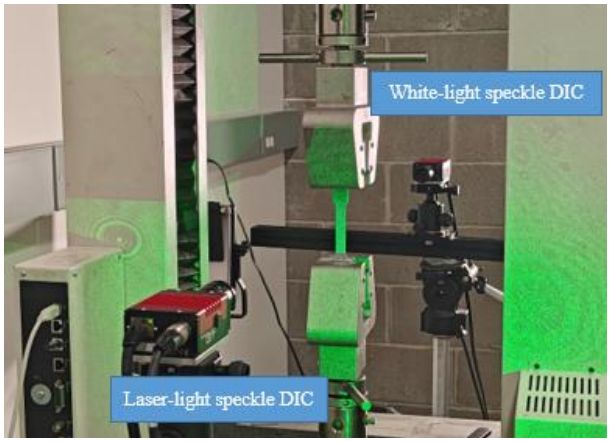

Figure 6.15 Experimental set-up for tensile test.

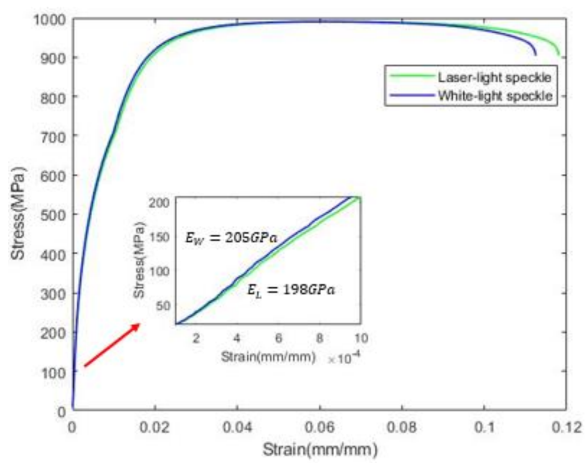

Figure 6.16 Stress-strain curve of DP 980.

6.4 Summary

This chapter examined the use of laser-light speckle DIC as an alternative to conventional white-light speckle DIC for full-field deformation measurement, and organized the discussion around the practical questions an experimentalist must answer: how speckles are formed and controlled, how accuracy and measurable range compare, why laser-light speckle decorrelates, and what strategies can mitigate the resulting limitations.

First, the chapter clarified that the two approaches differ fundamentally in pattern formation. White-light DIC typically relies on natural texture or artificially sprayed/printed patterns, whose quality is primarily governed by pattern preparation and is generally viewpoint independent, enabling mature 3D measurement. Laser-light speckle correlation, in contrast, uses coherent illumination of a rough surface to generate high-contrast subjective speckles through the imaging lens; as a result, speckle size and coverage can be tuned optically—most notably through aperture—while beam expansion, laser power, and surface roughness jointly affect texture quality. This distinction provides the basis for understanding why laser-light speckle correlation is attractive in coating-sensitive conditions. Second, the chapter highlighted that laser speckle correlation can achieve competitive accuracy in small-motion regimes but often exhibits a narrower "robust measurement window" when motion becomes large. In a synchronized rigid-body micro-translation benchmark, the raw displacement error obtained from laser-light speckle correlation was higher than that from white-light DIC, while simple calibration significantly reduced the laser-light speckle error. In small displacement-gradient conditions, both approaches showed comparable accuracy when referenced to interferometric measurements, and in uniaxial tensile tests, the strain and modulus measured by laser-light speckle correlation remained close to those from white-light DIC. Third, speckle decorrelation is the central challenge for laser-light speckle correlation in practice. As rigid-body motion or deformation increases, the laser speckle field can evolve such that original speckles diminish and new speckles emerge, degrading correlation and eventually losing correlation totally. Mitigation strategies reviewed in the chapter included incremental correlation with reference updating and compensation approaches.

Overall, laser-light speckle DIC have shown great potentials in displacement and strain measurement, especially when coating is undesirable, contrast is difficult to achieve with painted patterns. Recent developments in optical configuration and decorrelation compensation have significantly improved its applicability.

CHAPTER SEVEN

TEMPERATURE MEASUREMENT USING BOS WITH LASER SPECKLE AND HOLOGRAPHY

7.1 Introduction

Accurate measurement of temperature fields in air or gas flows is essential in many research and engineering contexts, such as understanding combustion processes and improving thermal/fluid performance [77-79]. Conventional contact sensing methods (e.g., thermocouples) require physical interaction with the flow and can disturb the local temperature and velocity fields; moreover, they typically provide only pointwise readings and therefore cannot directly deliver the full spatial distribution of the temperature field. These limitations have motivated sustained interest in non-contact, full-field optical temperature measurement techniques.

Among available non-intrusive approaches, Background-oriented Schlieren (BOS) has gained increasing attention in the past two decades because it offers a comparatively simple and practical route to quantitative flow-field measurements [80-87]. In BOS, images of a background pattern are recorded before and after a refractive-index field is introduced; a correlation algorithm is then used to estimate the apparent background displacement, from which density gradients—and ultimately temperature—can be inferred. A key practical advantage of BOS is that it does not rely on extracting intensity gradients in the way classical schlieren systems do; instead, it quantifies background-pattern motion through correlation, which improves robustness in the presence of ambient light and self-luminous flow fields (e.g., flames). BOS can also be implemented with relatively minimal optical components and is adaptable to large fields of view and multi-camera configurations.

Despite these strengths, a persistent challenge for BOS is experimental validation of accuracy, especially under realistic, unsteady flow conditions. The temperature and density fields in many flows can vary in time, and when BOS results are compared against another measurement taken at a different time (even seconds apart), apparent discrepancies may reflect true temporal variation rather than BOS error. In other words, the lack of synchronous validation can introduce a confounding factor that limits how confidently BOS uncertainty and sensitivity can be assessed. This motivates a comparative measurement approach that (i) provides higher accuracy than BOS and (ii) operates synchronously with BOS so that both methods interrogate the same instantaneous flow state.

Laser interferometry-based methods offer a reference for this purpose. Electronic Speckle Pattern Interferometry (ESPI) (also referred to as holographic interferometry in this context) can measure optical-path changes induced by refractive-index variations with very high sensitivity, and can be implemented as a full-field technique [88-92]. Phase-shifting ESPI, driven by a PZT actuator, enables rapid acquisition of the phase information needed for quantitative reconstruction, making it suitable as a validation tool when paired with BOS in a synchronized manner. However, BOS and ESPI are usually deployed as separate systems, and achieving truly synchronized measurements of the same flow field remains nontrivial. In this chapter, a new synchronous optical design is presented to address that gap. The core idea is to modify the ESPI object beam path by placing a rough background plate in the beam, so that coherent illumination generates a laser speckle background pattern for BOS while the ESPI system simultaneously records speckle interferograms. The laser beam is split into object and reference beams; the object beam is expanded and projected onto the rough plate to form the BOS background speckle, which then passes through the temperature field and reaches the camera, while the reference beam forms the interference required by ESPI at the camera plane. In this chapter, the temperature field above an alcohol lamp flame was selected as the measurement target. The BOS measurement results were compared with those obtained from holographic interferometry to analyze the accuracy, uncertainty, and sensitivity of BOS in temperature field measurements.

7.2 Fundamental of BOS and ESPI

7.2.1 BOS

In BOS, a background pattern consisting of a series of lines or dots, usually formed from natural textures or artificially created, lies on a plane behind the fluid under study. A charge coupled device (CCD) camera on the other side of the fluid then records the pattern. Any density change in the fluid causes the background pattern to distort in a characteristic way, which can be analyzed to obtain information about the density gradient in the fluid. The BOS technology schematic is shown in figure 7.1. Assuming paraxial recording and small deflection angles ($\varepsilon_y \approx \tan \varepsilon_y$), a formula for the image displacement Δy can be derived for the BOS technique.

$$\varepsilon_y = \frac{\Delta a}{L_b + L_c} \tag{7.1}$$

$$\Delta y = \frac{f}{L_b + L_c} \Delta a \tag{7.2}$$

where f is lens focus length, L_b is the distance between the background plane and the volume of interest, L_c is the distance between the lens and the volume of interest, Δa is the deflection displacement in the background plane.

The deflection angle can be derived from the refractive index,

$$\varepsilon_y = \frac{1}{n_0} \int \frac{\partial n}{\partial y} dz \tag{7.3}$$

The image displacement in the y direction can thus be rewritten as:

$$\Delta y = \frac{L_b f}{n_0 (L_b + L_c)} \int \frac{\partial n}{\partial y} dz \tag{7.4}$$

Similarity, the image displacement in the y direction can thus be rewritten as:

$$\Delta x = \frac{L_b f}{n_0 (L_b + L_c)} \int \frac{\partial n}{\partial x} dz \tag{7.5}$$

Therefore, the density gradient of the flow field satisfies the quantitative relationship shown in equations (7.4) and (7.5). Therefore, the density gradient of the flow field can be calculated by obtaining the displacement of the background pattern. Currently, the most used technique for calculating image displacement fields is digital image correlation algorithms.

Assume that the original subset center coordinate is (x_0, y_0), and the distorted subset center coordinate is (x_0', y_0'), then the displacement of the subset can be expressed as:

$$\begin{cases} \Delta x = x_0' - x_0 \\ \Delta y = y_0' - y_0 \end{cases} \tag{7.6}$$

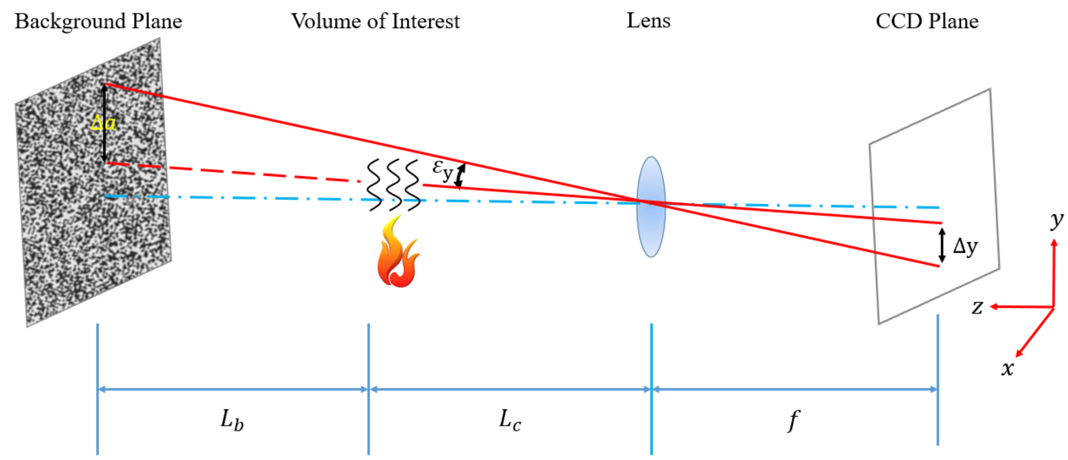

Figure 7.1 Background-oriented Schlieren schematic.

7.2.2 Holographic interferometry

The holographic interferometry method for measuring temperature fields is primarily based on the principle that temperature changes cause variations in the refractive index of air. These variations, in turn, lead to changes in the optical path length, resulting in the formation of interference fringes. Figure 7.2 shows a typical holographic interferometer setup for measuring the temperature field. A beam of laser light is divided into reference light and object light by a beam splitter. The reference light enters the CCD plane of the camera after passing through the reflector and the beam splitter, and the object light enters the CCD plane of the camera after passing through the measured temperature field. The superposition of the object and reference beams results in a speckle interferogram. The variation in temperature in temperature field will cause local changes in the refractive index of the air, which will result in local changes in the optical path of the object light, resulting in the light intensity variations in the speckle interferogram recorded on the CCD plane. Visible interference fringes can be obtained by calculating the intensity of the speckle interferograms on the CCD plane before and after introducing the measured temperature field. The intensity, *I,* of the speckle interferogram on the CCD plane before introducing the measured temperature field, can be written as:

$$I = I_0(1 + \gamma cos\theta) \tag{7.7}$$

where I_0 is the background, γ is the contrast, and θ is the phase difference between the object beam and reference beam.

After the measured temperature field is introduced into the optical path of the object beam, the intensity of the speckle interferogram on the CCD plane becomes:

$$I' = I_0[1 + \gamma \cos(\theta + \Delta)] \tag{7.8}$$

where Δ is a relative phase difference of the speckle interferograms before and after introducing temperature field.

High-quality phase images are obtained by four-step phase shifting technology. The phase shift is driven by the piezoelectric transducer (PZT) bonded to the reflector. The extremely high dynamic reaction of the PZT allows, recording the four images, with a π/2 phase shift between each two speckle interferograms, within one second. The four intensity expressions of the speckle interferograms are as follows:

$$\begin{cases} I_1 = I_0[1 + \gamma \cos\theta] \\ I_2 = I_0[1 + \gamma \cos(\theta + \frac{\pi}{2})] \\ I_3 = I_0[1 + \gamma \cos(\theta + \pi)] \\ I_4 = I_0[1 + \gamma \cos(\theta + \frac{3\pi}{2})] \end{cases} \tag{7.9}$$

The phase information can be extracted from the intensity variations:

$$\theta = arctan\frac{I_4 - I_2}{I_1 - I_3} \tag{7.10}$$

Similarly, the phase information after introducing temperature field (θ + Δ) can also be extracted and the relative phase difference Δ, resulting from the change in the refractive index of air in the temperature field can be obtained by subtracting calculated θ from (θ + Δ). The relationship between the relative phase difference Δ and refractive index can be written as:

$$\Delta = \frac{2\pi}{\lambda}\int_0^L (n - n_0)dl \tag{7.11}$$

where L is the length of the object beam passing through the temperature field, n is the refractive index of the temperature field, n_0 is the refractive index of air, λ is the wavelength of laser beam.

<u>7.2.3 Temperature field reconstruction</u>

In the experiment, it was assumed that the measured temperature field of the flame and the hot gas above it is distributed in an axisymmetric manner, so the refractive index is only a function of the radius r for each z-section. Taking the ESPI measurement as an example, the equation (7.11) can be written as:

$$\Delta = \frac{2\pi}{\lambda}\int_{-z_0}^{z_0} [n(r) - n_0]dz \tag{7.12}$$

where $z = \sqrt{r^2 - y^2}$, then becomes:

$$\Delta = \frac{2\pi}{\lambda}\int_{y_0}^{0} \frac{[n(r)-n_0]rdr}{\sqrt{r^2-y^2}} \tag{7.13}$$

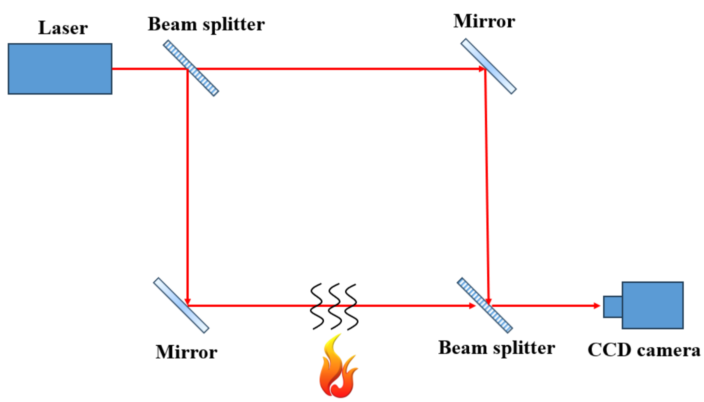

Figure 7.2 Holographic interferometry schematic.

Equation (7.13) is a typical Abel integral form, and the inverse transformation is:

$$n(r) - n_0 = \frac{\lambda}{2\pi^2}\int_r^{r_0} \frac{d\Delta(y)/dy}{\sqrt{y^2-r^2}}\,dy \tag{7.14}$$

The relationship between gas refractive index and gas density through the Gladstone-Dale equation is as follows:

$$\frac{n-1}{\rho} = K \tag{7.15}$$

where K is the Gladstone-Dale constant, n is gas refractive index and ρ is gas density. The ideal gas law gives the relationship between air density and temperature:

$$P = \rho RT \tag{7.16}$$

where P is the gas pressure, R is the gas constant.

Combining equation (7.15) and equation (7.16), the relationship between gas temperature and refractive index can be derived:

$$T = \frac{PK}{(n-1)R} \tag{7.17}$$

7.2.4 New synchronous measurement design

Figure 7.3 shows the schematic diagram of the experimental setup that realized the synchronous measurement of BOS and holographic interferometry. The laser beam emission is split by a beam splitter into an object beam and a reference beam. The reference beam passes through the PZT reflector and is reflected by the beam splitter into the camera. Meanwhile, the object beam is expanded by a beam expander and is projected onto a rough background plate, forming a speckle pattern on the surface. This speckle pattern passes through the measured temperature field and reaches at the camera position. In the holographic system, a speckle interferogram between object and reference beams is formed at the camera position, whereas, in the BOS system, just the object beam passing through the measured temperature field is needed. There are two options to use camera number. One is to use two cameras, one for holographic system to record the speckle interferogram, and the other for BOS system to record the speckle pattern from the object beam simultaneously. The other option is just to use one camera in combination of a switch in the path of the reference beam in the holographic setup. While taking BOS image, the reference beam will be closed by the switch and only the speckle pattern from the object will be recorded. This option will result in one to two seconds delay while taking holographic and BOS images. In our experiments, we used two cameras.

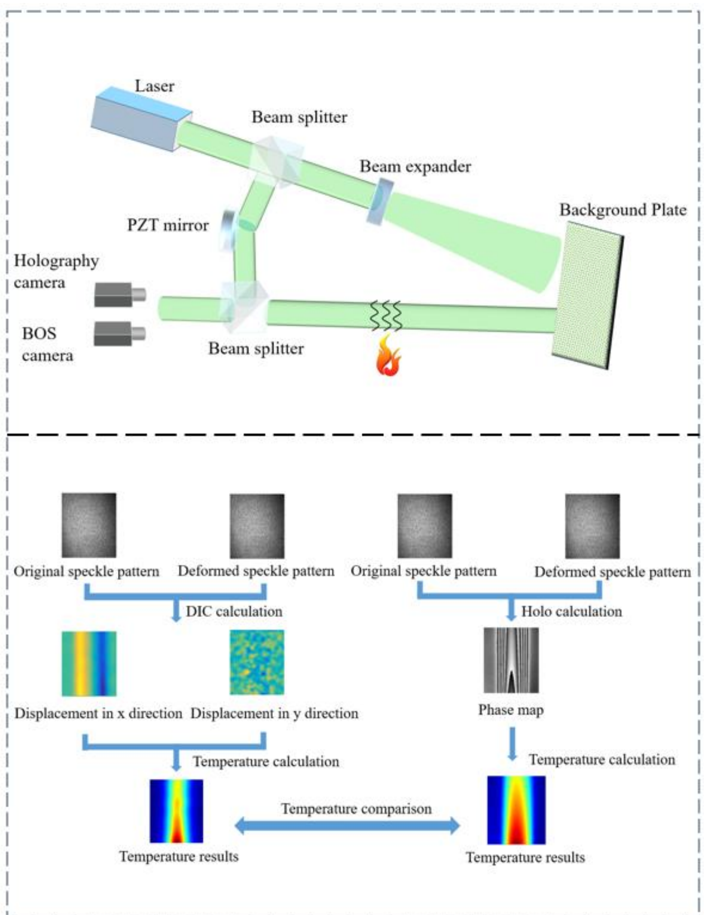

Figure 7.3 The schematic diagram of synchronous measurement of temperature field.

7.3 Experimental results and discussion

Figure 7.4 shows the experimental set-up which is consists of a laser source, two CCD cameras, a PZT mirror, a 90:10 beam splitter and background plate (plastic plate with rough surface). The measured target is the temperature field above the alcohol lamp flame. The wavelength of the laser is 532 nm and 500 mw power was used in the experiments (the maximum power of the laser is 5w). The diameter of the laser beam is about 2 mm, but it was expanded through a beam expander to a 300 mm beam to illuminate the background plate. As described above, two cameras were used, one for holographic system, and the other for BOS system.

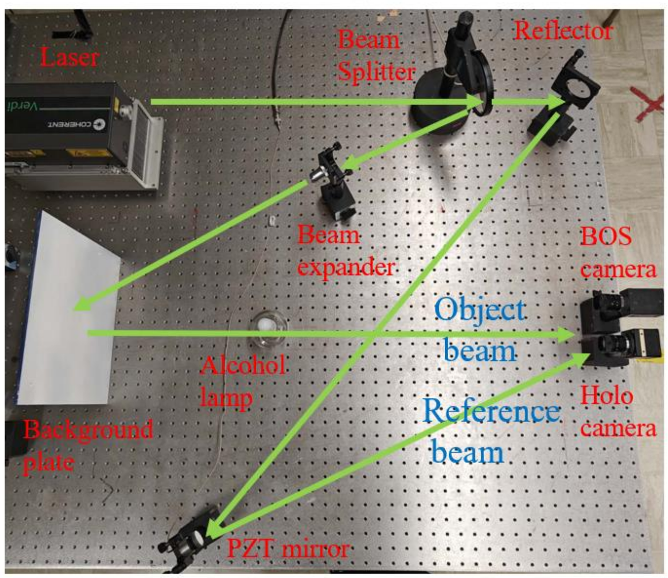

Figure 7.4 Experimental set-up.

The camera's field of view is 520mm x 600mm. The lower edge of the image field of view is about 5 mm from the top of the alcohol lamp flame. BOS measures the displacement distribution of the background speckles before and after the air is heated, as shown in Figure 7.5. It can be observed that the primary displacement component is in the x-direction (horizontal), indicating that the change in the air's refractive index due to heating causes the light to deflect horizontally. The positive and negative values of the displacement field indicate that the light is deflected in different radial directions. Unlike the BOS measurement results, holographic interference produces typical black and white fringe patterns. These fringes arise due to differences in the refractive index gradient, with a phase difference of 2π between each fringe in figure 7.6(a). It is important to note that the phase in the original fringe pattern is not continuous and requires phase unwrapping for temperature field reconstruction, as shown in figure 7.7(b). Figure 7.5(c) and figure 7.6(c) show the successful reconstruction of the temperature field above the alcohol lamp flame using both methods. The reconstructed temperature fields from the two methods exhibit a similar symmetric distribution. The highest temperature is located at the bottom center of the image, closest to the alcohol lamp flame. The temperature decreases radially away from the centerline and decreases more gradually with height, indicating that the air above the flame is heated, forming an upward-moving hot airflow that cools as it rises.

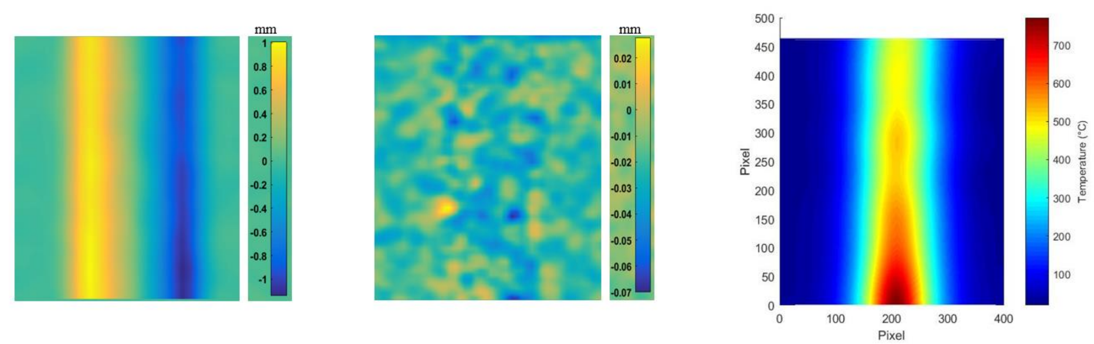

(a) Displacement in x direction (b) Displacement in y direction (c)Temperature field map

Figure 7.5 Experiment results from BOS: (a) Displacement in x direction; (b) Displacement in y direction; (c) Temperature field map.

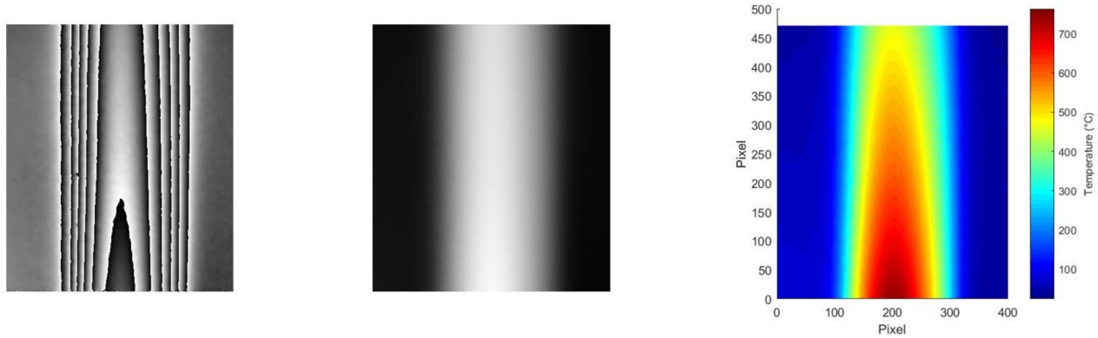

(a) Phase map (b) Unwrapped phase map (c) Temperature field map

Figure 7.6 Experiment results from holographic interferometry: (a) Phase map; (b) Unwrapped phase map; (c) Temperature field map.

7.3.1 Accuracy

In addition to comparing with holographic interferometry, thermocouples (K-type: -200ºC to 1372ºC) were also used as a supplementary comparative measurement method. The radial temperature calculation results at heights of 10mm, 30mm, and 50mm from the flame along were compared with thermocouple and holographic interferometry measurements, as shown in figure 7.7. Tables7.1, 7.2, 7.3 summarizes the percentage errors of BOS measurements compared to the other two methods at the same positions. Compared with holographic interferometry and thermocouples, at 10 mm height, the average BOS error is 7.0% and 8.5%, respectively. At 30 mm height, the average error is 5.1% and 7.3%, respectively. At 50 mm, the average error is 5.8% and 6.2%. The measurement error at 10 mm height is slightly higher than other heights. This may be because the temperature is higher there, and the refractive index gradient is larger, which causes the background speckle pattern in the camera to blur, thereby reducing the matching accuracy of the cross-correlation algorithm.

Compared to the errors with holographic interferometry, the measurement errors compared to thermocouples are larger. This might be due to a few reasons. Firstly, thermocouple measurements are intrusive and inevitably affect the temperature field. Secondly, it is challenging to determine the exact position of the thermocouple within the temperature field accurately. Thirdly, the flow field is not completely static. The flame and the gases are moving as the gas rises. The holographic and BOS techniques are recording at the same time, but the thermocouples have a physical response time that may not have been at the exact time of the image capture. In contrast, comparing BOS with holographic interferometry results involves simply extracting temperature values at the same time and positions in the images, whereas even slight positional differences of the thermocouple can lead to different temperature readings.

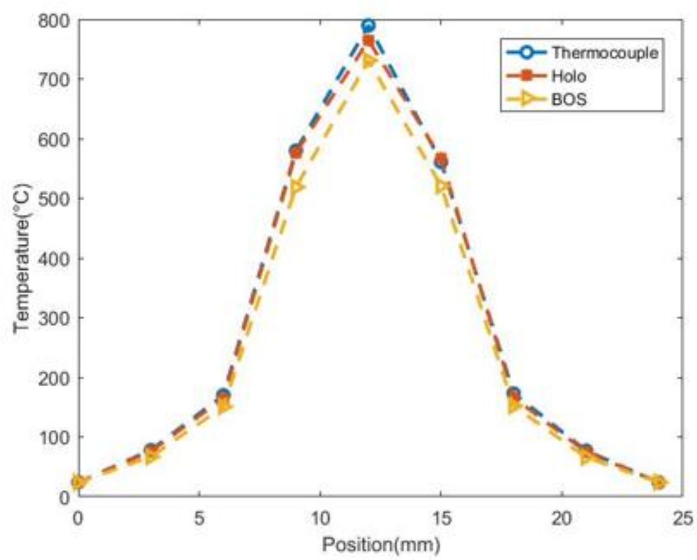

(a)

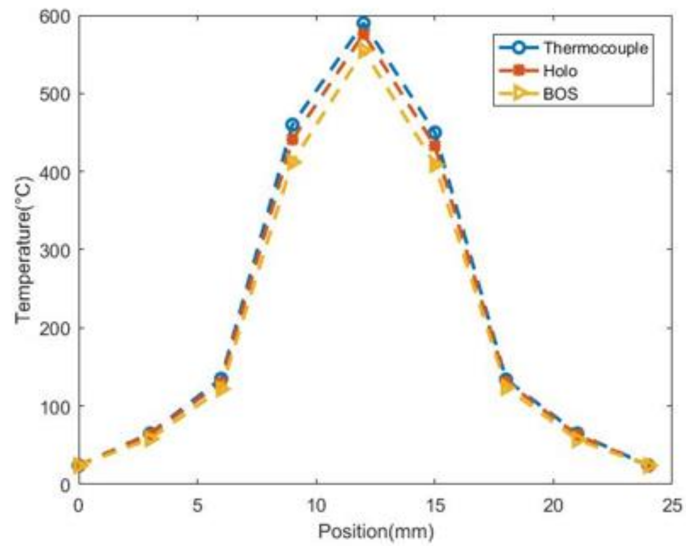

(b)

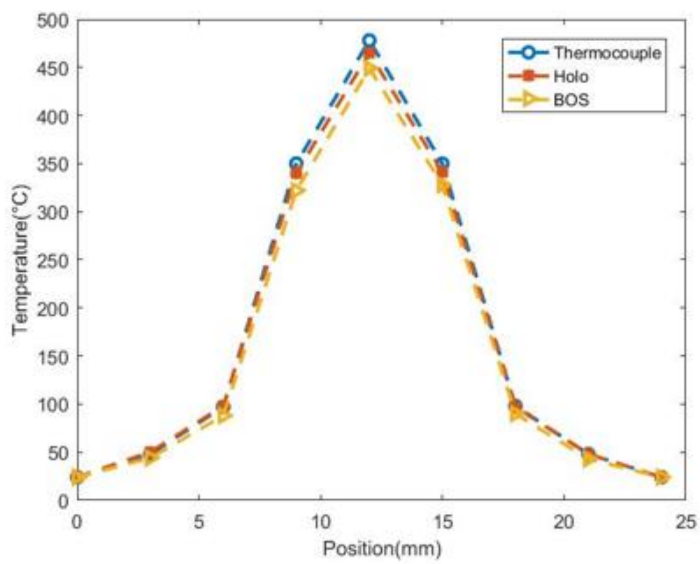

(c)

Figure 7.7 Temperature field distribution along the radial direction at different heights from the alcohol lamp flame: (a) 10mm height; (b) 30mm height; (c) 50mm height.

Table 7.1 Percent error of temperature of BOS method versus holographic interferometry and thermocouple along radial distributions at 10mm heights.

Position	0mm	3mm	6mm	9mm	12mm	15mm	18mm	21mm	24mm
Percent error (VS Holo)	0%	11.8%	8.5%	9.9%	4.4%	8.1%	8.4%	12.0%	0%
Percent error (VS Thermo)	0%	14.1%	11.2%	10.5%	7.5%	7.1%	12.1%	14.3%	0%

Table 7.2 Percent error of temperature of BOS method versus holographic interferometry and thermocouple along radial distributions at 30mm heights.

Position	0mm	3mm	6mm	9mm	12mm	15mm	18mm	21mm	24mm
Percent error (VS Holo)	0%	9.4%	6.2%	6.6%	3.6%	5.5%	5.3%	9.5%	0%
Percent error (VSThermo)	0%	10.8%	9.6%	10.4%	5.9%	9.1%	7.5%	12.3%	0%

Table 7.3 Percent error of temperature of BOS method versus holographic interferometry and thermocouple along radial distributions at 50mm heights.

Position	0mm	3mm	6mm	9mm	12mm	15mm	18mm	21mm	24mm
Percent error (VS Holo)	0%	12.0%	10.2%	5.3%	3.4%	3.8%	7.2%	10.4%	0%
Percent error (VSThermo)	0%	8.3%	9.3%	8%	6.1%	6.3%	8/2%	10.4%	0%

7.3.2 Uncertainty

The uncertainty in BOS measurement results arises from various sources of error introduced during the preparation, acquisition, and evaluation stages of the experiment. Analyzing and minimizing these error sources is essential for improving measurement accuracy.

(1) Speckle pattern

The quality of the speckle pattern is a significant source of error. An optimal background speckle pattern typically exhibits random positioning, uniform size, and good grayscale contrast. Although the laser speckle used in this study has been optimized through various evaluation parameters, some degree of error remains unavoidable.

(2) Camera

The random variations in brightness captured by the camera during data acquisition introduce noise, which is largely dependent on the sensor type and experimental conditions. Since image noise cannot be eliminated, the speckle pattern on the sample surface should contain sufficient grayscale contrast and appropriate size to ensure good measurement quality. In addition, during the operation of the camera, the internal electronic components will generate heat, which is called self-heating effect. Studies have shown that the camera will rise by several degrees Celsius to more than ten degrees Celsius before reaching thermal equilibrium. Capturing images before the camera stabilizes can result in virtual plane translation and virtual thermal expansion strain. Therefore, it is suggested to wait 5-10 minutes (depends on type of the camera) until the cameras reach a stable temperature [93-95].

(3) Lens

Lens distortion is one of the most serious problems that limit measurement accuracy. The distortion includes radial and tangential errors. The radial distortion is caused by the spherical shape of the lens, whereas tangential distortion is caused by the decentering and non-orthogonality of the lens components with respect to the optical axis. The most well-known method to eliminate these distortions is to do calibration by checkboard plate. The distortion model coefficients of the lens are calculated by shooting a calibration plate of known geometric shape, and then the distorted image is restored to a nearly distortion-free state through a calibration algorithm. The details of calibration can be found in reference. However, the measurement area at the corner of the image will still be affected by distortion, resulting in measurement uncertainty.

(4) Exposure time

In temperature field measurement, the rapid flow of the flow field will inevitably cause image blur during exposure, resulting in measurement errors. Therefore, the appropriate exposure time is not only important for lighting, but also can minimize the generation of errors. For typical BOS measurements, the threshold for image motion blur is about 0.1 – 0.3 pixels. The displacement (in pixels) of each exposure can be calculated as follows:

$$Displacement[px] = Velocity[\frac{mm}{s}] \times (Image\ Scale[\frac{px}{mm}]) \times (Exposure\ Time[s]) \tag{7.18}$$

Based on this formula, the appropriate exposure time can be calculated.

(5) Vibration

Any vibration on the BOS system may cause unexpected measurement errors, so it is very important to ensure that the BOS system is stably fixed. It is recommended to use an anti-vibration tripod and an optical table to minimize the effects of vibration.

(6) Facet size and grid spacing

The facet size, also called as subset size, defines the dimensions of a discrete elemental area that will be tracked, correlated, and evaluated in displacement calculation. Undoubtedly, the facet size has an important influence on the accuracy of the reconstructed temperature. A smaller facet size can improve the spatial resolution of the local area but will also amplify the effect of noise. A larger facet size can improve the evaluation stability and make the results smoother, but at the expense of reduced spatial resolution. Therefore, the actual facet size depends on many factors, such as the field of view size, camera pixel resolution, etc. The grid spacing is the distance between the facets and therefore sets the special resolution. A larger grid spacing results in a reduced density of data points and an aliasing effect. An optimal grid spacing is around 1/2 to 2/3 of the facet size.

(7) Boundary conditions

When converting displacement measurement results to refractive index values, it is crucial to consider the boundary conditions. Potential disturbances can lead to non-ideal boundary conditions, thereby introducing errors.

Since the BOS measurement method primarily relies on displacement analysis, the reliability of the displacement can be reflected by the correlation coefficient: the closer its value is to 1, the higher the degree of correlation, and the more reliable the calculated displacement results become. As shown in figure 7.8, the distribution of the correlation coefficient is similar to the distribution of the displacement. In regions with displacement, the correlation coefficient begins to decrease, particularly showing a downward trend as the displacement increases. This can be explained by the fact that areas with larger displacements correspond to regions with higher temperatures, where significant refractive index changes cause greater image blurring. As a result, the matching accuracy decreases and the measurement uncertainty increases. In regions without displacement data, the correlation coefficient remains close to 1, indicating that the matching process involves almost no error.

Figure 7.9 presents the measurement uncertainty of the x-direction displacement. It is observable that the measurement uncertainty closely aligns with the displacement distribution. Areas with larger displacements have greater measurement uncertainties, especially near the area of the alcohol lamp flame. This may also be one of the reasons for the larger temperature reconstruction errors in that area.

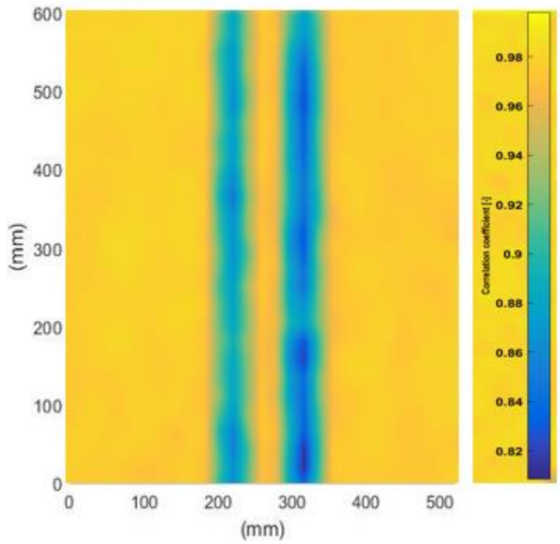

Figure 7.8 Correlation coefficient map.

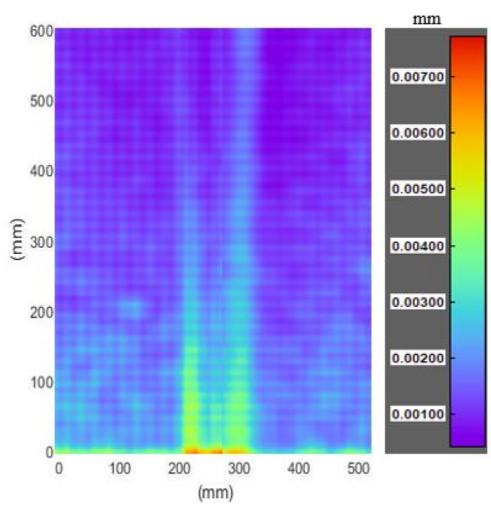

Figure 7.9 Uncertainty of x-displacement obtained by the software used from Dantec Dynamic GmbH, Germany.

7.3.3 Sensitivity

The BOS method directly measures the displacement of background speckles.

According to Eqn. 4, the magnitude of displacement is influenced not only by the refractive index gradient but also by the position of the measured flow field in the setup and the focal length of the lens, which affects the sensitivity of displacement measurements. To study the impact of these two factors, the distance from the lens to the background plate was fixed at 100mm, and the distance from the alcohol lamp to the background plate was set to 20mm, 40mm, 60mm, and 80mm. The lens focal lengths were set to 35mm, 50mm, 75mm, and 100mm. Figure 7.10 shows the horizontal (x-direction) displacement field distribution with a lens focal length of 50mm and the alcohol lamp positioned at distances of 20mm, 40mm, 60mm, and 80mm from the background plate. It can be observed that as the alcohol lamp moves further from the background plate (closer to the camera), the displacement field's range within the field of view increases, and the absolute displacement values also increase. This indicates that the further the flow field is from the background plate, the higher the BOS measurement sensitivity. Figure 7.11 shows the x-direction displacement field distribution with the alcohol lamp 60mm from the background plate at different lens focal lengths. It can be seen that the displacement field increases with increasing focal length. This indicates that the longer the focal length of lens, the higher the BOS measurement sensitivity. The average background displacement under different conditions is shown in Table 7.4 and figure 7.12. It can be seen that the background displacement is positively correlated with the distance between the object and the background (L_b) and the focal length of the lens (f). The maximum average displacement is 0.595 mm, occurring at the maximum focal length (f=100mm) and the farthest distance from the background plate (L_b=80mm). The minimum average displacement is 0.011 mm, occurring at the minimum focal length (f

=35mm) and the closest distance to the background plate (L_b=20mm). The sensitivity under the maximum displacement conditions is 54.1 times higher than under the minimum displacement conditions. It is important to note that as the focal length increases, the camera's field of view decreases, which means the observable fluid region is reduced. Therefore, an appropriate focal length of lens must be chosen to balance sensitivity and field of view size for different flow field observations.

Another noteworthy point is that under the experimental conditions set above, the measurement sensitivity of holographic interferometry remains almost unchanged, as shown in figure 7.13 and figure 7.14. The number of fringes, which characterize the sensitivity of holographic interferometry, is symmetrically distributed in six lines, with only the fringe width changing. According to Eqn. 16, the phase is affected only by the refractive index gradient and the laser wavelength, meaning that lens focal length and flow field position do not affect the measurement sensitivity of holographic interferometry.

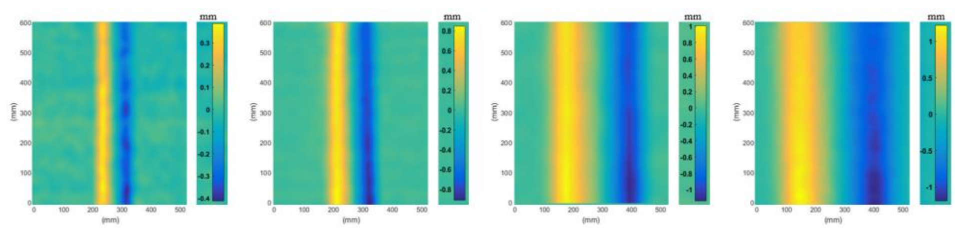

$L_b = 20mm$ $L_b = 40mm$ $L_b = 60mm$ $L_b = 80mm$

Figure 7.10 Horizontal displacement distribution under different L_b conditions.

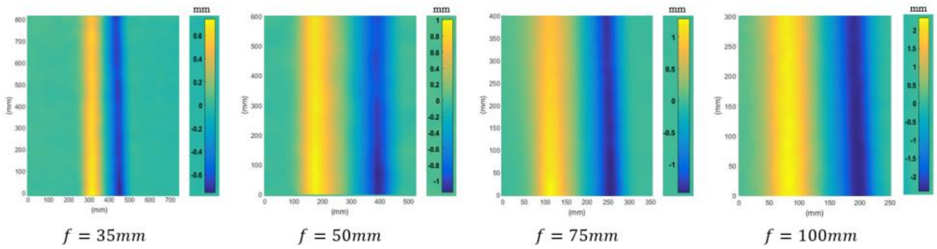

Figure 7.11 Horizontal displacement distribution under different f conditions.

Table 7.4 Average background speckle pattern displacement under different conditions.

f \ L_b	20mm	40mm	60mm	80mm
35mm	0.011 mm	0.058 mm	0.114 mm	0.191 mm
50mm	0.056 mm	0.122 mm	0.233 mm	0.367 mm
75mm	0.098 mm	0.203 mm	0.326 mm	0.468 mm
100mm	0.143 mm	0.299 mm	0.440 mm	0.595 mm

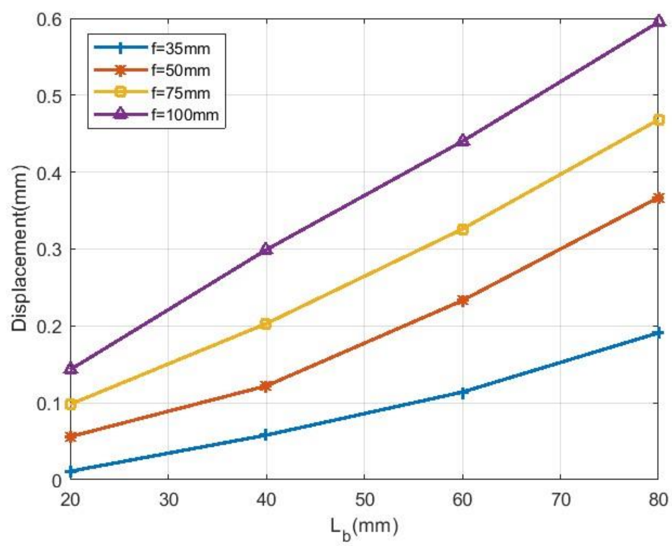

Figure 7.12 Average background speckle pattern displacement.

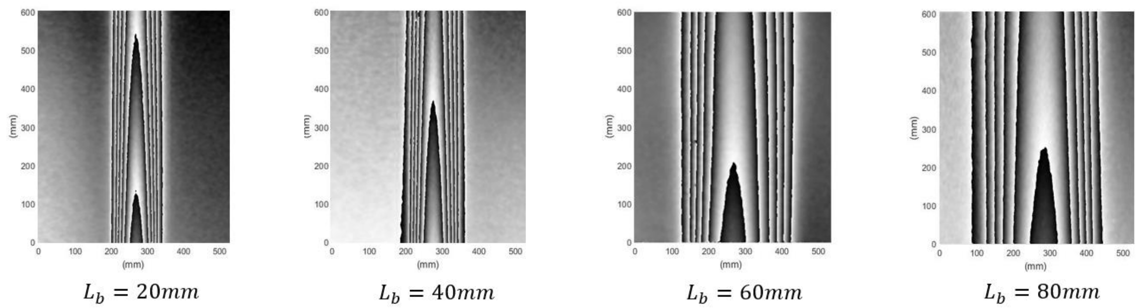

Figure 7.13 Phase map under different L_b conditions.

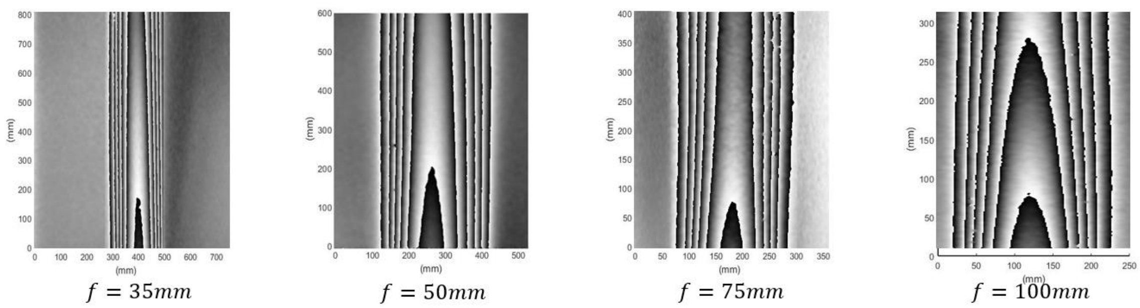

Figure 7.14 Phase map under different f conditions.

7.4 Summary

This chapter developed and validated a synchronous full-field temperature measurement framework that combines BOS with ESPI to address a key limitation in BOS practice: the lack of truly time-synchronized validation, which can otherwise confound accuracy assessment when the flow field is unsteady. The motivation is that BOS is attractive for temperature measurement due to its simplicity and practicality, yet its accuracy is difficult to verify when reference measurements are not taken at the same instant. By enabling BOS and ESPI to observe the same flow state simultaneously, the proposed approach avoids errors caused by slight temporal variations during non-synchronous comparisons.

A central contribution of this chapter is an innovative optical setup that physically integrates the two techniques. Specifically, a rough plate is inserted into the object-beam path of ESPI and illuminated by the laser to generate a laser-speckle background for BOS, while ESPI interferograms are recorded concurrently. In this way, BOS speckle images and ESPI data are acquired under the same optical path and the same thermal disturbance, forming a direct basis for cross-validation of reconstructed temperature fields.

Then, the chapter demonstrated synchronous temperature reconstruction in a controlled experiment measuring the hot air flow above an alcohol lamp flame. The BOS displacement fields showed a dominant horizontal component, consistent with refraction-driven background apparent motion in the measurement geometry, while ESPI produced characteristic fringe patterns that required phase unwrapping prior to temperature reconstruction. At a practical level, this agreement supports the feasibility of using synchronized ESPI as a high-sensitivity reference to evaluate BOS performance; the study further noted that BOS measurement sensitivity depends on the flow-field position and camera focal length, highlighting that BOS uncertainty is not spatially uniform and must be interpreted with system geometry in mind. These outcomes provide an experimental foundation for assessing BOS accuracy, uncertainty, and sensitivity.

CHAPTER EIGHT

LASER-LIGHT SPECKLE DECORRELATION FOR NDT

8.1 Introduction

Laser speckle–based optical techniques have long been used in NDT because defects such as delaminations, debonds, or local stiffness reductions often produce subtle, spatially nonuniform surface deformation under thermal, vacuum, or mechanical excitation. Conventionally, interferometric methods (e.g., holography and shearography) convert these small deformation responses into high-contrast fringe patterns and therefore provide outstanding displacement or displacement-gradient sensitivity. However, interferometric configurations typically require more stringent environmental stability and optical alignment.

In parallel with interferometric approaches, correlation-based methods such as DIC are widely adopted due to their operational simplicity and tolerance to ambient disturbances. A key practical challenge for laser-light speckle correlation, however, is decorrelation: even modest changes in surface tilt, local gradient, or optical path can substantially alter the speckle intensity pattern, causing correlation to degrade. Importantly, while decorrelation is often treated as an error source in speckle metrology, it also carries physically meaningful information: under small excitation, regions that exhibit elevated decorrelation frequently coincide with zones of strong local displacement gradients and nonuniform deformation, which are precisely the signatures expected above subsurface defects. This observation motivates treating speckle decorrelation not as a failure mode to be avoided, but as a diagnostic signal for NDT [96,97].

A major limitation of prior decorrelation-based NDT methods is that useful defect contrast often becomes apparent only when the speckle field approaches near-complete decorrelation under relatively large excitation. Under moderate loading, speckle patterns are commonly partially decorrelated, and defect-related signatures can be weak and easily masked by background fluctuations and illumination nonuniformity. To address this partial-decorrelation regime, this chapter proposes a practical framework built on a robust local similarity measure: zero-mean normalized cross-correlation (ZNCC). A decorrelation coefficient is defined as $D=1-ZNCC$, enabling decorrelation to be quantified and mapped before full decorrelation occurs. The mechanical relevance of D is clarified via a small-deformation analysis showing that the decorrelation measure increases with the magnitude of the local displacement gradient, explaining why defects often appear as ring-shaped responses in decorrelation maps.

To improve inspect ability when defect signatures are weak, an enhancement strategy is applied directly to the D maps, including background normalization, robust contrast stretching, and gamma correction. Furthermore, to reduce reliance on subjective visual judgement and to enable operator-independent inspection, an automated detection pipeline is developed using a YOLOv8 object detector trained on a single-class decorrelation dataset spanning diverse loading levels and defect morphologies. The dataset contains 500 decorrelation images with approximately 2200 annotated defects, and the trained detector achieves strong localization performance (mAP50 approaching 1.0 and mAP50:95 around 0.75–0.78), demonstrating the feasibility of reliable automatic defect localization from decorrelation maps. Finally, the chapter validates the proposed approach on composite specimens under thermal excitation and further provides a controlled comparison under identical vacuum loading against holography and shearography. The comparative results confirm the expected sensitivity differences—interferometric methods reveal defect signatures at lower pressure differentials—while showing that the proposed decorrelation method becomes clearly defect-correlated as excitation increases, and that combining enhancement and YOLOv8 detection improves practical detect ability when signatures are weak.

8.2 Decorrelation theory

8.2.1 Speckle field model under local surface tilt

Several works have established that, under coherent illumination, the decorrelation observed between a reference speckle pattern and a loaded one is governed primarily by the local surface tilt (i.e., the angular change of the surface normal projected onto the illumination–observation baseline). Intuitively, a small tilt introduces a phase ramp on the object wave, which produces a lateral or vertical shift of the speckle spectrum. The larger the shift, the lower the correlation between the two realizations.

A laser is directed onto the sample after passing through a beam expander. The complex speckle field in the image plane for the sample’s region of interest(ROI) without tilt is written as a convolution between the local object field and the system point-spread function：

$$\tilde{a}(r) = \tilde{g}(r) \otimes p(r) \tag{8.1}$$

where $r = (x, y)$ denotes image-plane coordinates, $\tilde{g}(r)$ is the complex object field associated with the ROI in the untilted (reference) state, $p(r)$ is the point-spread function, and $\otimes$ is convolution.

After loading, a small angular change of the surface normal, α, introduces a linear phase ramp across the ROI. In the image plane this appears as:

$$\tilde{a}(r) = \tilde{g}(r)e^{j2\pi\Delta v r}\otimes p(r) \tag{8.2}$$

where $\Delta v = (\Delta v_x, \Delta v_y)$ is the spatial frequency change corresponding to the amplitude spectrum shift.

Figure 8.1 schematically shows a defect region within the ROI before and after loading. The defect induces local out-of-plane deformation and an surface tilt α. Taking Fourier transforms to equation (8.1) and (8.2):

$$\tilde{A}(v) = \tilde{G}(v)P(v) \tag{8.3}$$

$$\tilde{A}(v) = \tilde{G}(v)P(v + \Delta v) \tag{8.4}$$

Thus, loading that produces a local tilt does not change the random object spectrum G but translates the spectrum by Δv. The spectral shift is linear in tilt and set by wavelength, magnification, and illumination–observation geometry:

$$\Delta v = \frac{1+cos\theta}{\lambda}\frac{1}{M}\alpha \tag{8.5}$$

here λ is the wavelength, θ is the laser incidence angle, M is the lateral magnification.

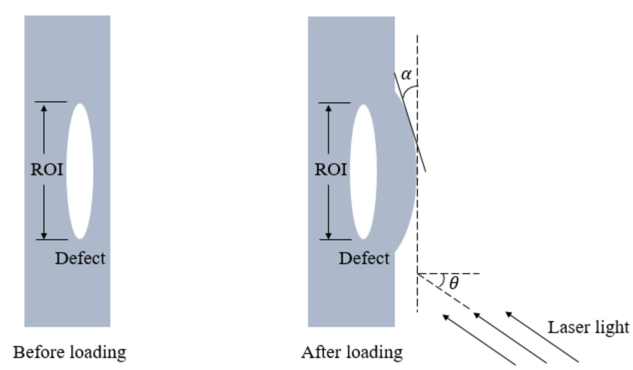

Figure 8.1 Schematic illustration of defect-induced local deformation before and after loading.

<u>8.2.2 ZNCC-based decorrelation operator</u>

The correlation coefficient, as a quantitative indicator describing the local similarity between the reference speckle image and the loaded speckle image, plays a central role in speckle metrology and digital image correlation. By calculating the correlation within a finite subregion, complex speckle intensity variations can be compressed into a dimensionless scalar, thus enabling quantitative comparison of local speckle evolution behavior. Among various correlation measurement methods, ZNCC is the most widely used due to its robustness to illumination changes, contrast variations, and noise disturbances. The value of ZNCC ranges from [0, 1], where 1 indicates that the two speckle images are perfectly correlated, and 0 indicates complete decorrelation. Therefore, its numerical value can directly reflect the degree of similarity between the speckle fields before and after loading. Based on this characteristic, ZNCC is also naturally suitable as a quantitative indicator of the degree of decorrelation. For ease of subsequent analysis and visualization, this paper further defines the decorrelation degree $D = 1 - ZNCC$, where $D \in [0, 1]$, and the closer the value of D is to 1, the more significant the speckle decorrelation phenomenon is in that region under the loading effect.

Although the ZNCC-based metric introduced above provides a convenient and robust means to quantify speckle decorrelation, its mechanical meaning must be clarified before it can be reliably used for nondestructive evaluation. In digital image correlation techniques, the motion of speckle patterns within a subset can be decomposed into rigid body translation and differential deformation components. Typically, under non-destructive testing conditions, the applied load is small, and the laser speckle pattern maintains local similarity after rigid body translation, thus having little effect on the

ZNCC value. However, differential motion within the subregion (e.g., displacement gradients, local tilt, or shear) introduces spatially varying phase and intensity changes to the laser speckle, leading to decorrelation. To establish a direct link between spatial domain correlation metrics and deformation, we analyze the ZNCC within a local window under the assumption of small deformations.

Let $I_0(x)$ and $I_1(x)$ denote the reference and loaded speckle intensities, respectively. Within a local window W centered at x_0 with normalized weights $w(x)$, the displacement field $u(x)$ is approximated as locally affine,

$$u(x) \approx b + A(x - x_0) \tag{8.6}$$

where b is a rigid translation and $A = \nabla u(x_0)$ is the local displacement gradient.

Allowing for affine photometric changes, the loaded image can be written as:

$$I_1(x) = \gamma I_0\big(x + u(x)\big) + \beta + \eta(x) \tag{8.7}$$

where γ is a gain, β an offset, and η additive noise.

Under small deformation within the subset, $I_1(x)$ is expanded by the first-order Taylor:

$$I_1(x) = \gamma[I_0(x) + \nabla I_0(x)^{\mathrm{T}}(b + A(x - x_0))] + \beta + \eta(x) \tag{8.8}$$

The ZNCC is:

$$\mathrm{ZNCC} = \frac{\int w\tilde{I_0}\tilde{I_1}dx}{\sqrt{\int w\tilde{I_0}^2dx}\sqrt{\int w\tilde{I_1}^2dx}} \tag{8.9}$$

Define the decorrelation score $D = 1 - \mathrm{ZNCC}$. After standard small-perturbation algebra, the leading term is:

$$D \approx \frac{1}{2\sigma_0{}^2}\mathrm{tr}(A^{\mathrm{T}}C_gAC_x) \tag{8.10}$$

with $\sigma_I{}^2 = E_w[\tilde{I_0}^2]$ the local intensity variance, $C_g = E_w[\nabla I_0 \nabla I_0{}^{\mathrm{T}}]$ the speckle gradient covariance, and $C_x = E_w[(x - x_0)(x - x_0)^{\mathrm{T}}$ the window second moment. For isotropic speckle and window, $C_g \approx \sigma_g{}^2 I$, $C_x \approx \sigma_x{}^2 I$, yielding:

$$D \approx \frac{1}{2} k \|A\|_F{}^2, k = (\sigma_g{}^2 / \sigma_0{}^2) \sigma_x{}^2 \tag{8.11}$$

Equation (8.11) demonstrates that ZNCC-based decorrelation grows quadratically with the local displacement gradient $\|A\|_F$ under small deformation. Additionally, D increases with speckle gradient power σ_g, which means finer speckle will increase sensitivity.

<u>8.2.3 Ring-shaped decorrelation pattern</u>

An important and distinctive feature of the proposed decorrelation-based analysis is the ring-shaped response observed over defect regions under loading. Figure 8.2 shows the decorrelation coefficient map of a defect area under thermal loading. When a subsurface defect is subjected to thermal or mechanical excitation, the surface above the defect typically undergoes an out-of-plane bulging deformation. Although the displacement amplitude is largest at the center of the bulge, the deformation in this region is nearly uniform within a finite subset, resulting in a smaller local displacement gradient. Consequently, the speckle pattern within the subset undergoes an almost rigid-body motion, and the decorrelation coefficient remains lower. In contrast, the transition zone surrounding the bulging region is characterized by a rapid spatial variation of displacement, giving rise to pronounced local gradients, which produces significant decorrelation. As a result, the decorrelation coefficient reaches its maximum not at the center of the defect, but along a circumferential band surrounding it, giving rise to a ring-shaped pattern. This pattern directly follows from the sensitivity of decorrelation coefficient to local displacement gradients, rather than to displacement magnitude itself, as established in section 8.2.2.

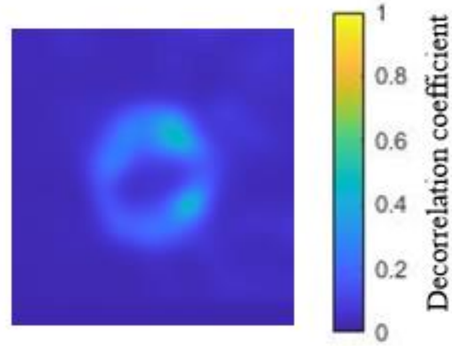

Figure 8.2 The typical ring-shaped decorrelation pattern.

8.3 Decorrelation image enhancement and automatic defect detection

While the analysis in Section 8.2 establishes the physical origin of ZNCC-based decorrelation and explains the emergence of ring-shaped responses over defect regions, practical nondestructive evaluation under small deformation conditions poses additional challenges. When the defect is small or is deep below the surface, defect-induced decorrelation often remains weak. In this situation, reliably identifying the location of defects becomes difficult. To address this limitation, decorrelation features are enhanced to improve contrast, and automatic defect identification provides excellent assistance for manual inspection.

8.3.1 Decorrelation image enhancement for weak responses

All enhancement operations are applied directly to the scalar decorrelation map D, rather than to the original speckle intensities, ensuring that the physical meaning of the correlation computation is retained. To suppress slow-varying background components caused by illumination nonuniformity, speckle statistics drift, or windowing effects, a background-normalized decorrelation field is first computed as:

$$D_{hp} = D - D * G_{\sigma_{hp}} \tag{8.12}$$

where $*$ denotes convolution and $G_{\sigma_{hp}}$ is a normalized Gaussian kernel with standard deviation σ_{hp}. This operation removes low-frequency trends while preserving localized peaks.

To further expand the dynamic range of weak decorrelation responses, a robust linear contrast stretching is then applied. Let μ and σ denote the median and scaled median absolute deviation (MAD) of D_{hp}, respectively,

$$\mu = \text{median}\ (D_{hp}),\ \sigma = 1.4826\ \text{MAD}\ (D_{hp}) \tag{8.13}$$

Lower and upper bounds are defined as $l = \mu - k\sigma$ and $u = \mu + k\sigma$, where k controls the stretch strength. The linearly normalized decorrelation map is given by:

$$D_{lin} = \text{clip}(\frac{D_{hp} - l}{u - l + \varepsilon}, 0{,}1) \tag{8.14}$$

where ε is a small constant preventing numerical instability. This mapping is monotonic within the clipping range and therefore preserves the relative ordering of decorrelation values.

Finally, a gamma transformation is employed to emphasize defect-induced responses occupying the mid-to-high range of the decorrelation distribution:

$$D_{\gamma} = (D_{lin})^{\gamma} \tag{8.15}$$

For gamma transformation, higher decorrelation values associated with strong local displacement gradients are selectively enhanced, whereas background fluctuations are comparatively suppressed. Since the gamma transform is a monotonic mapping on

[0,1], it does not change decorrelation pattern structures.

8.3.2 Automatic defect detection based on YOLOv8

While the enhancement strategy described in Section 8.3.2 substantially improves the visual contrast of weak decorrelation signatures, reliable nondestructive evaluation further requires an objective and automated means of identifying defect-related patterns. Rule-based approaches relying on fixed thresholds, connected components, or handcrafted geometric criteria are often sensitive to parameter tuning and may struggle when the decorrelation response is fragmented, irregular, or partially obscured by background fluctuations—conditions that frequently arise under different loading. To address these limitations, a data-driven detection framework based on the YOLOv8 object detection architecture is adopted. Unlike pixel-wise segmentation methods, YOLOv8 performs direct localization of target patterns via bounding boxes, making it well suited to the present problem where defect signatures manifest as spatially extended, ring-like decorrelation structures rather than isolated peaks. Importantly, the method does not require explicit assumptions regarding defect shape, size, or circularity, allowing it to accommodate irregular and partially formed annular responses.

As illustrated in figure 8.3, YOLOv8 formulates defect inspection as a single-stage object detection problem, where defect localization and confidence estimation are produced in a single forward pass from the input NDT image. The network first employs a backbone composed of stacked convolutional layers and C2f blocks to extract hierarchical features while progressively downsampling the image, enabling robust representation of both fine defect textures and higher-level structural patterns. A Spatial Pyramid Pooling-Fast (SPPF) module is further introduced to enlarge the effective receptive field and improve sensitivity to weak and multi-scale defect responses. The extracted features are then passed to the neck, which performs multi-scale feature aggregation via upsampling and lateral connections, and fuses complementary information through repeated Concat operations, thereby enhancing scale robustness for defects with varying apparent sizes and shapes. Finally, the detection head applies multi-level Detect branches to predict bounding boxes, class scores, and confidence values at different feature resolutions; the final predictions are obtained after confidence thresholding and non-maximum suppression (NMS) to remove redundant overlapping detections, yielding the detected defect regions in the output image.

For single-class defect detection, YOLOv8 is trained with a multi-task objective that jointly optimizes localization and detection confidence. The overall loss can be expressed as:

$$L = \lambda_{box} L_{box} + \lambda_{obj} L_{obj} + \lambda_{cls} L_{cls} \tag{8.16}$$

where L_{box} enforeces accurate bounding-box regression, L_{obj} learns an objectness score indicating whether a spatial location corresponds to a defect, and L_{cls} is the class loss.

The box regression loss is typically defined using an IoU-family criterion to maximize the overlap between the predicted box B and the ground-truth box B^*,

$$L_{box} = 1 - IoU(B, B^*), IoU(B, B^*) = \frac{|B \cap B^*|}{|B \cup B^*|} \tag{8.17}$$

The objectness and class terms are commonly implemented by the binary cross-entropy (BCE) loss. For a predicted probability $p \in [0,1]$ and target label $y \in \{0,1\}$,

$$BCE(p, y) = -[y log(p) + (1 - y)\log(1 - p)] \tag{8.18}$$

Accordingly, $L_{obj} = BCE(p_{obj}, y_{obj})$ encourages high confidence at defect locations and suppresses false alarms on background regions, while $L_{cls} = BCE(p_{cls}, y_{cls})$ penalizes incorrect defect predictions. This composite objective enables end-to-end learning of robust defect localization on decorrelation maps despite variations in defect morphology and contrast. Figure 8.4 summarizes the overall workflow of the proposed ZNCC-based decorrelation mapping, enhancement, and YOLOv8 detection.

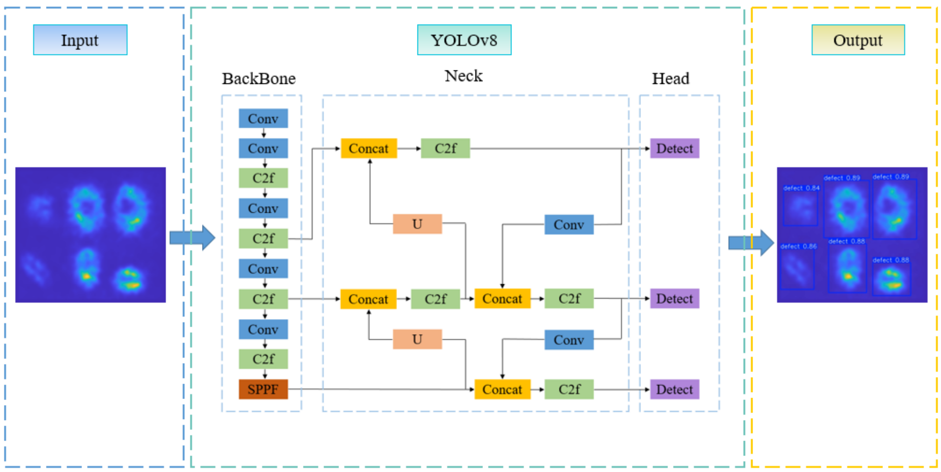

Figure 8.3 The YOLOv8 network for automatic defect detection.

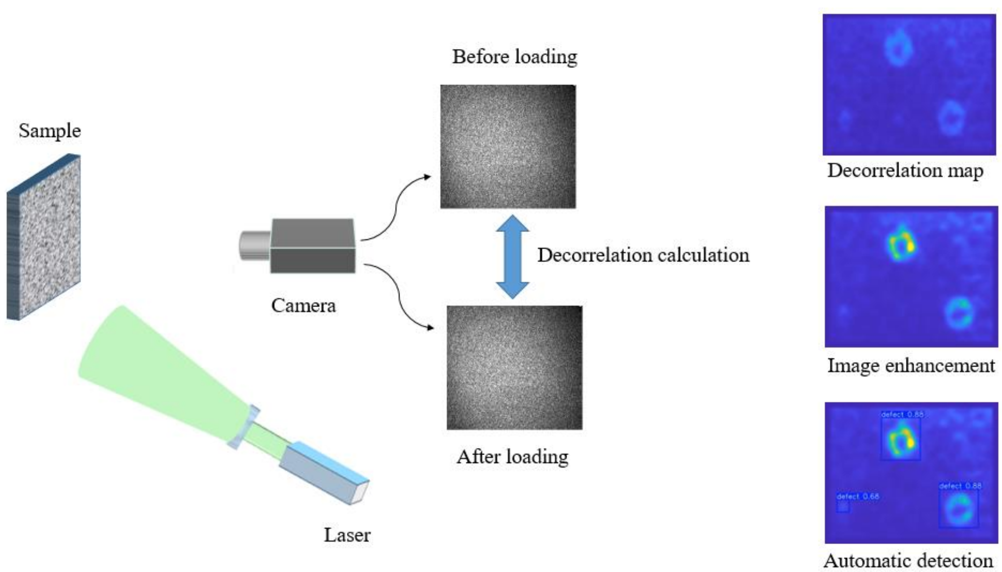

Figure 8.4 The workflow of proposed method.

8.4. Experiment results and discussion

8.4.1 Experimental set-up and decorrelation behavior

The experimental arrangement is shown in figure 8.5. A helium–neon (He–Ne) laser with a central wavelength of 632 nm was used as the coherent illumination source. The emitted laser beam was directed to a mirror and then expanded by a beam expander to obtain a larger and more uniform illumination area. The expanded beam illuminated the rough surface of the specimen, generating a high-contrast speckle pattern due to the coherent interference of the scattered light. A composite specimen with defects was clamped on the experimental platform, and surface heating was applied using a heat gun. During the loading process, a grayscale camera with a spatial resolution of 640 × 480 pixels continuously recorded a sequence of speckle images of the specimen surface.

Figure 8.6 presents the decorrelation map results of a specimen containing three defects under heat-gun excitation. As the thermal loading progresses, ring-shaped fringe patterns gradually emerge in the upper-middle, lower-left, and lower-right regions of the specimen. The locations of these ring-like responses are consistent with the actual defect positions, demonstrating that the proposed decorrelation analysis can effectively reveal defect-related anomalies. In addition, the observed ring-shaped patterns provide an intuitive visualization of the surface deformation gradient: regions with a higher decorrelation value correspond to areas experiencing a larger local deformation gradient, indicating stronger nonuniform deformation induced by subsurface defects.

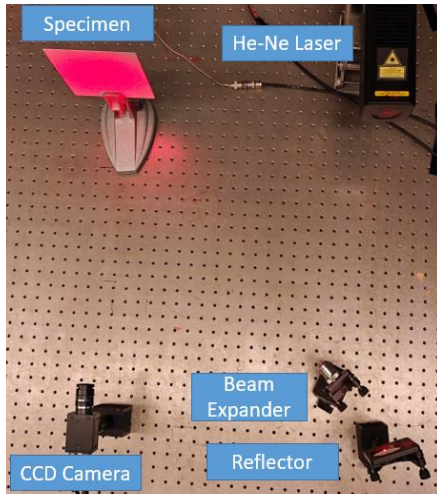

Figure 8.5 The experimental set-up.

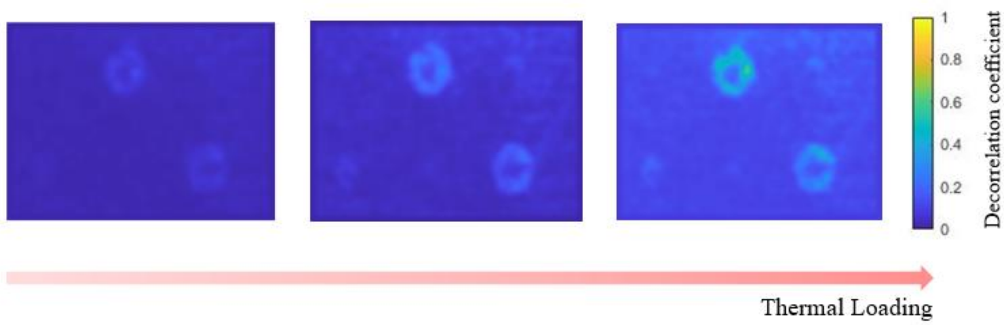

Figure 8.6 Evolution of decorrelation maps for a specimen with three defects under heat-gun excitation.

8.4.2 Image enhancement results

Figure 8.7 illustrates the effectiveness of the proposed image-enhancement strategy for visualizing weak defect signatures under low thermal excitation using the same specimen with three defects. Figure 8.7(a) shows the original decorrelation map obtained under a weak heat load. Because the induced deformation is small, the resulting decorrelation response is correspondingly weak, leading to low contrast between the defect regions and the surrounding intact area. In particular, the small defect located in the lower-left region is barely visible, making the decorrelation pattern difficult to distinguish by direct visual inspection. Figure 8.7(b) presents the enhanced decorrelation maps obtained with a fixed γ=1 and different linear stretching parameters (k=3,5,7,9). After applying the linear contrast stretching, the ring-like features associated with the upper-middle and lower-left defects become more discernible for all tested k values, although the lower-left defect remains relatively ambiguous. As k decreases, a larger effective dynamic range is assigned to high-decorrelation pixels, which produces a wider and more pronounced response around the defects. However, smaller k also amplifies background fluctuations in non-defective regions, indicating a trade-off between defect enhancement and background magnification. To further improve the visibility of weak defects, figure 8.7(c) investigates the effect of the gamma parameter under a fixed k=5. Increasing γ progressively suppresses decorrelation background regions while preserving high-decorrelation responses associated with defects. Consequently, the contrast between the defect-induced ring patterns and the intact area is further enhanced, yielding visually clearer defect signatures. This nonlinear mapping effectively attenuates residual background variations introduced by linear stretching and leads to cleaner decorrelation maps. These results demonstrate that the proposed enhancement scheme substantially improves the visibility of weak decorrelation features under small loading conditions, and that k and γ provide complementary control over peak amplification and background suppression.

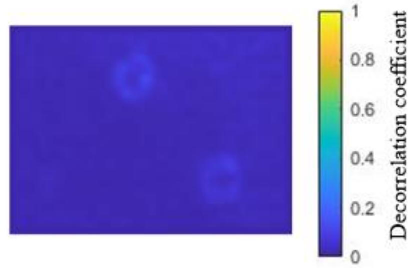

(a)

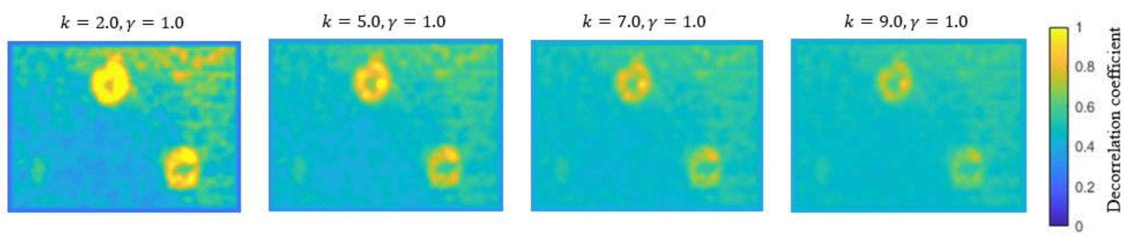

(b)

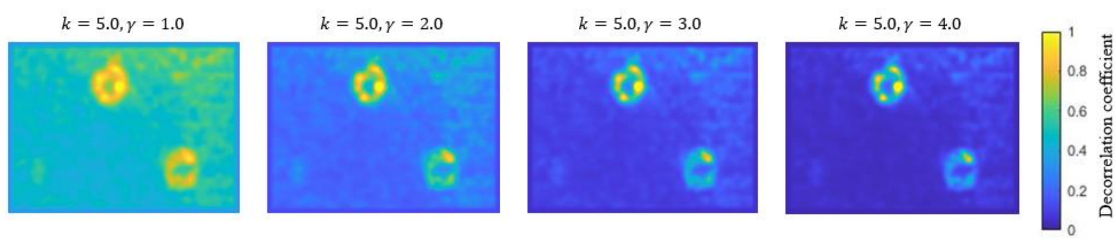

(c)

Figure 8.7 Enhancement of weak decorrelation signatures under small loading: (a) Raw decorrelation map under small thermal loading; (b) Effect of linear contrast stretching parameter k on the decorrelation map (γ=1); (c)Effect of gamma correction γ on the decorrelation map (k=5).

8.4.3 Automatic defect detection results

To enable fully automated defect localization from decorrelation maps, a YOLOv8-based object detection framework was adopted. The detection task was formulated as a single-class problem, where each defect instance was annotated by a bounding box and assigned the label defect. A dedicated dataset was constructed comprising 500 decorrelation images with approximately 2200 defects, covering a wide range of inspection conditions, including different loading levels, as well as defects with various sizes, shapes, and depths. Representative samples are shown in Figure 8. Model training was conducted on a computer equipped with an Intel® Core™ i7-7700K CPU @ 4.2 GHz and an NVIDIA GeForce GTX 1070 (8 GB) GPU. The network was trained for 40 epochs.

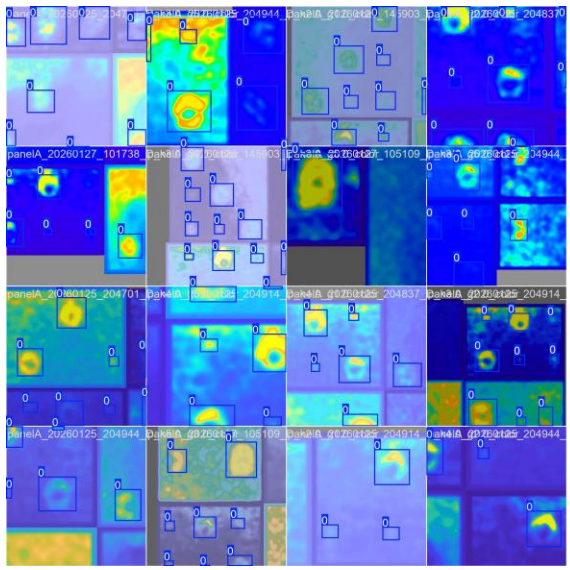

Figure 8.8 Representative decorrelation defect images in dataset.

To quantitatively evaluate the defect-detection performance of the YOLOv8 model, the mean Average Precision (mAP) primarily was evaluated, which summarizes the precision–recall behavior and jointly reflects classification confidence and localization accuracy. For a given IoU threshold τ, a prediction is regarded as a true positive when IoU$\geq\tau$. The Average Precision (AP) is then computed as the area under the precision-recall curve at that threshold. Since this study involves a single defect class, the mAP is identical to AP. In particular, mAP50 reports AP at τ=0.5, providing an overall measure of detection capability, whereas mAP50:95 averages AP over IoU thresholds from 0.50 to 0.95 (step 0.05), offering a stricter assessment of bounding-box tightness and localization precision.

Figure 8.9 summarizes the evolution of detection accuracy during training in terms of mAP50 and mAP50:95. As shown in figure 8.9(a), mAP50 increases rapidly in the early stage, rising from a low initial value to above 0.9 within the first ∼10 epochs, indicating that the model quickly learns to localize defect-related patterns on the decorrelation maps. After this stage, mAP50 continues to improve with minor fluctuations and approaches saturation, reaching a stable plateau close to 1.0 in the later epochs (approximately after epoch 25), which confirms a robust detection capability under the adopted training settings. A similar trend is observed for the stricter metric mAP50:95 in Figure 8.9(b). Although mAP50:95 follows the same overall upward trajectory, its absolute values remain lower than mAP50, as expected due to the progressively stricter IoU requirements. mAP50:95 rises steadily and converges to approximately 0.75–0.78 by the end of training. The performance gap between mAP50 and mAP50:95 suggests that the model reliably detects the presence and approximate locations of defects, while the remaining limitation is primarily associated with bounding-box tightness. This behavior is reasonable for decorrelation maps where defect signatures often appear as diffuse ring-like regions with gradual intensity transitions, which can make the precise delineation of box boundaries inherently ambiguous. Overall, the convergence of both metrics demonstrates stable training and strong detection performance.

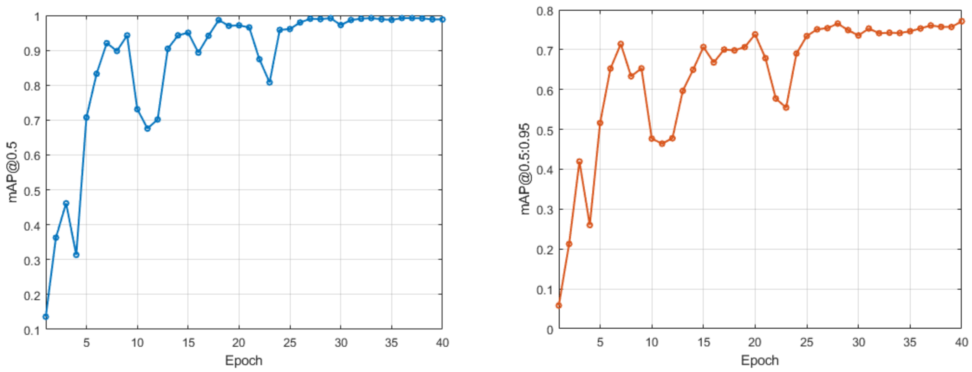

(a) (b)

Figure 8.9 Training convergence curves of YOLOv8 in terms of (a) mAP_{50} and (b) $\mathrm{mAP}_{50:95}$.

Figure 8.10 provides qualitative examples from the test set to demonstrate the detection capability of the trained YOLOv8 model under challenging conditions. Figure 8.10(a) corresponds to a specimen containing three defects under a relatively small thermal/mechanical excitation, where the decorrelation responses are weak. In this case, the lower-left defect is nearly imperceptible by visual inspection and remains difficult to distinguish even after image enhancement in figure 8.7(a). Nevertheless, the trained model successfully identifies all three defects, indicating strong sensitivity to subtle defect-related signatures. Figure 8.10(b) further shows that the detector generalizes well across defects with different sizes, where multiple defect regions are consistently localized with high confidence. Figure 8.10(c) demonstrates robustness to shape variability: the defect responses deviate from ideal ring-shaped patterns and exhibit irregular morphologies, yet the model still produces correct detections. These examples confirm that the proposed YOLOv8-based approach achieves reliable defect localization across varying excitation levels, defect scales, and defect morphologies, supporting its applicability for automated inspection of decorrelation maps.

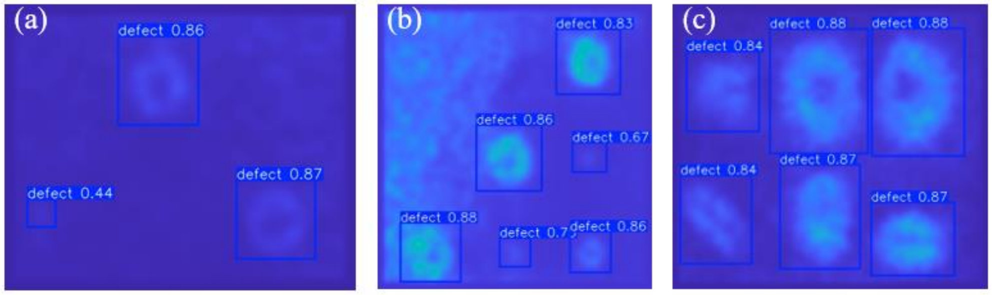

Figure 8.10 Representative YOLOv8 detection results on the test set: (a) Weak signature case. (b) Multiple defect case. (c) Difeerent defect shape case.

8.5 Comparison with holography and shearography

Holography and shearography are two representative coherent optical NDT techniques that have been extensively used for defect inspection. They are well recognized as benchmark methods because they provide high sensitivity to defect-induced displacement (holography) and displacement gradients (shearography) under external excitation. To enable a fair comparison under identical experimental conditions, vacuum loading was applied with pressure differentials of Δp=2,6,10, and 14psi on a composite plate containing two defects. Figure 8.11 compares the responses obtained by the proposed decorrelation-based method, holography, and shearography, respectively. At Δp=2psi, the decorrelation map in figure 8.11(a) does not exhibit a distinct defect pattern, indicating that the defect-induced decorrelation is too weak to be reliably distinguished from the background at this loading level. In contrast, both holography (figure 8.11(b)) and shearography (figure 8.11(c)) already reveal a weak response in the right-hand region, although the signatures are still subtle. When the pressure is increased to Δp=6psi, a ring-shaped pattern becomes clearly visible in the right defect region in the decorrelation result, and correspondingly, pronounced circular fringes and butterfly-like fringe signatures are observed in holography and shearography, respectively. At

Δp=10psi, the right-hand defect response further intensifies, and a weaker decorrelation increase becomes visible in the left region; correspondingly, the fringe order in holography and shearography increases for the right defect and the left defect begins to exhibit discernible fringes. Finally, at Δp=14psi, the decorrelation region around the right defect expands and deviates from an ideal ring structure, accompanied by elevated decorrelation in the central area due to the larger overall deformation, while a localized decorrelation concentration remains observable near the smaller left defect. Meanwhile, both holography and shearography show increased fringe density (higher fringe order) at larger loading, further confirming enhanced deformation/gradient responses around defects.

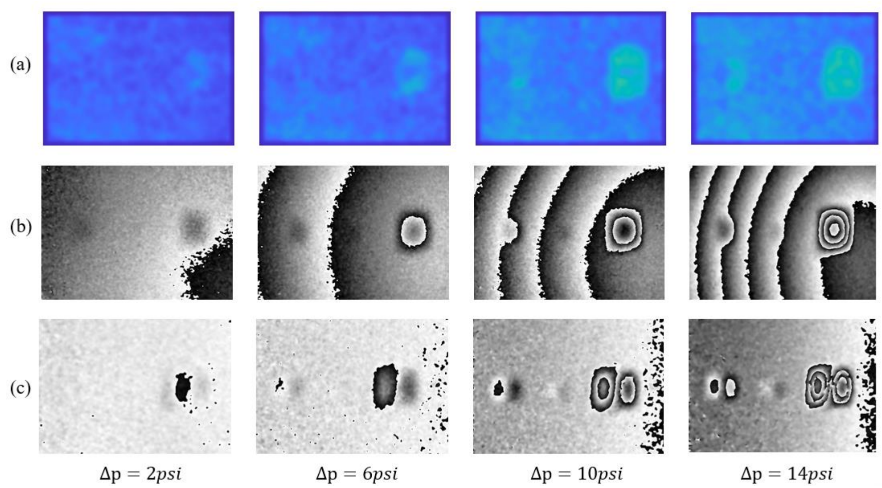

Figure 8.11 Sensitivity comparison under vacuum-loading conditions: (a) Decorrelation maps; (b) Holograms; and (c) Shearograms.

Figure 8.12 further illustrates the YOLOv8-based detection results on the decorrelation maps under the same vacuum-loading levels. At Δp=2psi, no defect is detected at the selected confidence threshold, which is consistent with the fact that the decorrelation response at this loading level is extremely weak and visually indistinguishable from background fluctuations. When the pressure increases toΔp=6psi, the model successfully localizes the dominant defect on the right-hand side. At Δp=10psi, the detector identifies both the right defect with high confidence and the weaker left defect with a lower confidence score, indicating that the second defect signature begins to emerge but remains relatively subtle. Finally, at Δp=14psi, both defects are consistently detected with high confidence. These results indicate that combining decorrelation mapping with a data-driven detector enables operator-independent defect localization and improves practical inspectability, especially when defect signatures are subtle and manual inspection is challenging.

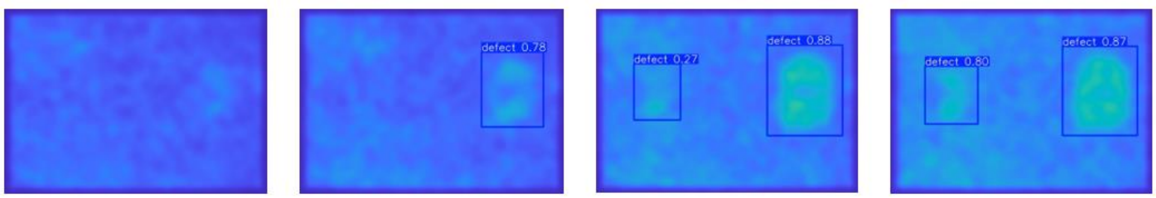

Figure 8.12 YOLOv8 detection results on decorrelation maps under vacuum loading.

Overall, it should be acknowledged that holography and shearography possess. intrinsically higher displacement sensitivity due to their interferometric nature. In principle, their basic displacement resolution is on the order of half a wavelength, and with phase-shifting techniques the effective sensitivity can be improved to approximately one-tenth to one-twentieth of a wavelength, enabling the detection of extremely small deformation responses. Consistent with our comparative experiments under identical vacuum loading, defect-related signatures become observable in holography and shearography at lower pressure differentials than in the decorrelation maps. Therefore, the proposed decorrelation-based approach does not aim to reach the sub-wavelength sensitivity achievable by interferometric methods. Nevertheless, it still provides high practical sensitivity to defect-induced nonuniform deformation, as evidenced by the clear emergence and evolution of defect-correlated patterns with increasing pressure change. More importantly, when combined with image enhancement and YOLOv8-based automated detection, the decorrelation maps can be interpreted in an operator-independent manner, improving the ability of detect for weak or ambiguous signatures.

8.6 Summary

This chapter developed a laser-speckle decorrelation–based NDT framework that treats decorrelation not merely as a limitation of speckle correlation, but as a useful defect-sensitive signal under mechanical/thermal excitation. The central idea is that subsurface defects often produce localized deformation gradients; these gradients perturb the speckle field and increase correlation loss, enabling defects to be revealed through a decorrelation map even when the surface displacement itself is small.

To quantify partial decorrelation in a robust and physically interpretable way, the chapter introduced a ZNCC-based operator and defined the decorrelation coefficient as $D=1-ZNCC$ within a finite window. The mechanical relevance of this definition was clarified by linking the growth of D to the magnitude of local displacement gradients under small deformation, providing an explanation for the characteristic ring-like signatures that appear around defect regions as the load increases. Recognizing that defect contrast can remain weak in the partial-decorrelation regime, the chapter further proposed a practical enhancement pipeline applied directly to the D maps—background normalization, robust contrast stretching, and gamma correction—which significantly improves visibility of weak signatures. Furthermore, to enable objective inspection and reduce dependence on human judgement, the chapter also presented an automated defect-localization workflow using YOLOv8 trained on decorrelation images spanning different loading levels and defect morphologies. The trained model demonstrated strong localization capability, showing that the deep-learning model can maintain strong detection performance across diverse defect shapes and under low-contrast conditions, where defect signatures may be faint and vary substantially from case to case.

Finally, the chapter assessed practical performance through experiments and comparisons with interferometric NDT methods. Under identical loading conditions, holography/shearography typically exhibited earlier sensitivity at low excitation, while decorrelation-based maps became increasingly defect-correlated as excitation increased. Importantly, the combination of (i) the ZNCC-derived decorrelation metric, (ii) enhancement for weak signatures, and (iii) automated detection provides a complete, inspection-oriented pipeline that is experimentally simple, and compatible with challenging environments where interferometric stability may be limiting.

CHAPTER NINE

CONCLUSION

This dissertation advanced optical full-field measurement for material characterization by developing and applying a double-side DIC framework and by exploring laser speckle as a versatile measurement carrier for deformation and thermal-field measurement.

On the sheet-metal side, the double-side DIC system reconstructs the front and back surfaces in a unified coordinate system, enabling direct measurement of thickness strain together with in-plane strains. This capability was then leveraged in three representative applications. First, a direct R-value measurement approach was demonstrated that does not rely on the common volume-constancy assumption, because thickness strain is measured rather than inferred. Second, a physically motivated method for localized necking onset identification was established by reconstructing the evolution of local cross-sectional area from the measured width and thickness engineering strains using virtual line gauges, and defining necking onset based on the time-dependent behavior of the area at the necking boundary. Third, for dissimilar-thickness tailor welded blanks, where eccentric loading introduces bending and causes distinct front/back strain responses near the weld, a combined indentation–dual-side DIC methodology was implemented to obtain a corrected HAZ stress–strain curve, using microhardness and nanoindentation to identify weld sub-zones and modulus and using double-side strain fields with regression-based calibration to reduce geometry-induced bending effects.

In parallel, this dissertation assessed the opportunities and limitations of laser-light speckle correlation relative to conventional white-light speckle DIC, emphasizing the roles of speckle formation, decorrelation, measurable range, and mitigation strategies. Laser speckle offers coating-free, high-contrast patterns with optically tunable speckle size, but is more susceptible to decorrelation and viewpoint dependence, which constrains large-motion tracking and conventional stereo 3D correspondence. Additionally, a synchronized optical configuration integrating BOS with holographic interferometry was developed to evaluate BOS temperature measurement under identical flow conditions; by optimizing laser-speckle background quality and performing synchronous measurements of a hot-air above an alcohol-lamp flame, the study demonstrated consistent temperature distributions between BOS and interferometry, quantified BOS accuracy and sensitivity, and highlighted uncertainty growth in regions of larger displacement. Beyond deformation and thermometry, this dissertation further explored laser-speckle decorrelation as a diagnostic signal for NDT. A ZNCC-based decorrelation metric was introduced to map partial decorrelation and reveal defect-sensitive responses under loading, and an enhancement pipeline was developed to strengthen weak signatures. To enable objective inspection, a YOLOv8-based detector was trained to localize defects from decorrelation maps, demonstrating strong detection performance across diverse defect shapes and under low-contrast conditions.

Overall, this dissertation advances optical full-field measurement for broader material characterization and engineering evaluation tasks through two research directions: (i) multi-camera double-side DIC for thickness-sensitive mechanics, and (ii) laser-speckle-based correlation for displacement/strain measurement, thermal-flow temperature measurement, and decorrelation-based NDT. The methods and findings presented here provide practical experimental pathways and physically interpretable criteria that can support future developments in sheet-metal forming characterization, welded-structure assessment, and speckle-based diagnostics.

REFERENCE

[1] Altan, T., & Tekkaya, A. E. (Eds.). (2012). *Sheet metal forming: fundamentals*. Asm International.

[2] Gronostajski, Z., Pater, Z., Madej, L., Gontarz, A., Lisiecki, L., Łukaszek-Sołek, A., ... & Ziółkiewicz, S. (2019). Recent development trends in metal forming. *Archives of Civil and Mechanical Engineering*, *19*(3), 898-941.

[3] Chu, T. C., Ranson, W. F., & Sutton, M. A. (1985). Applications of digital-image-correlation techniques to experimental mechanics. *Experimental mechanics*, *25*, 232-244.

[4] Hung, Y. Y., & Ho, H. P. (2005). Shearography: An optical measurement technique and applications. *Materials science and engineering: R: Reports*, *49*(3), 61-87.

[5] Di, H., Xin, Y., & Jian, J. (2018). Review of optical fiber sensors for deformation measurement. *Optik*, *168*, 703-713.

[6] Hild, F., & Roux, S. (2006). Digital image correlation: from displacement measurement to identification of elastic properties–a review. *Strain*, *42*(2), 69-80.

[7] Sutton, M. A., Orteu, J. J., & Schreier, H. (2009). *Image correlation for shape, motion and deformation measurements: basic concepts, theory and applications*. Springer Science & Business Media.

[8] Pan, B., Qian, K., Xie, H., & Asundi, A. (2009). Two-dimensional digital image correlation for in-plane displacement and strain measurement: a review. *Measurement science and technology*, *20*(6), 062001.

[9] Leclerc, H., Périé, J. N., Roux, S., & Hild, F. (2009, May). Integrated digital image correlation for the identification of mechanical properties. In *International conference on*

computer vision/computer graphics collaboration techniques and applications (pp. 161-171). Berlin, Heidelberg: Springer Berlin Heidelberg.

[10] McCormick, N., & Lord, J. (2010). Digital image correlation. *Materials today*, *13*(12), 52-54.

[11] Reu, P. (2012). Introduction to digital image correlation: Best practices and applications. *Experimental Techniques*, *36*(1), 3-4.

[12] McCormick, N., & Lord, J. (2012, November). Digital image correlation for structural measurements. In *Proceedings of the Institution of Civil Engineers-Civil Engineering* (Vol. 165, No. 4, pp. 185-190). Thomas Telford Ltd.

[13] Sutton, M. A., & Hild, F. (2015). Recent advances and perspectives in digital image correlation. *Experimental Mechanics*, *55*(1), 1-8.

[14] Palanca, M., Tozzi, G., & Cristofolini, L. (2016). The use of digital image correlation in the biomechanical area: a review. *International biomechanics*, *3*(1), 1-21.

[15] Li, J., Xu, W., Xie, X., Siebert, T., & Yang, L. (2016). Experimental study of FLD0 for aluminum alloy using digital image correlation with modified ISO method. *International Journal of Materials Research*, *107*(3), 245-253.

[16] Pan, B. (2018). Digital image correlation for surface deformation measurement: historical developments, recent advances and future goals. *Measurement Science and Technology*, *29*(8), 082001.

[17] Fang, S., Zheng, X., Zheng, G., Zhang, B., Guo, B., & Yang, L. (2021). A new and direct r-value measurement method of sheet metal based on multi-camera dic system. *Metals*, *11*(9), 1401.

[18] Fang, S., Zheng, X., Gerini-Romagnoli, M., Sheng, S., McCarty, E., Huang, L., & Yang, L. (2024). A novel methodology to determine tensile properties in the heat-affected zone of tailor welded blanks with different base material thicknesses. *Materials Science and Engineering: A*, *915*, 147268.

[19] Mguil-Touchal, S., Morestin, F., & Brunei, M. (2025). Various experimental applications of digital image correlation method. *WIT Transactions on Modelling and Simulation*, *17*.

[20] Li, J., Xie, X., Yang, G., Zhang, B., Siebert, T., & Yang, L. (2017). Whole-field thickness strain measurement using multiple camera digital image correlation system. *Optics and Lasers in Engineering*, *90*, 19-25.

[21] Steinchen, W., & Yang, L. (2003). *Digital shearography: theory and application of digital speckle pattern shearing interferometry* (Vol. 93). Bellingham, WA: SPIE press.

[22] Yang, L., & Ettemeyer, A. (2003). Strain measurement by three-dimensional electronic speckle pattern interferometry: potentials, limitations, and applications. *Optical Engineering*, *42*(5), 1257-1266.

[23] Goodman, J. W. (2007). *Speckle phenomena in optics: theory and applications*. Roberts and Company Publishers.

[24] Françon, M. (2012). *Laser speckle and applications in optics*. Elsevier.

[25] Yang, L., Xie, X., Zhu, L., Wu, S., & Wang, Y. (2014). Review of electronic speckle pattern interferometry (ESPI) for three dimensional displacement measurement. *Chinese Journal of Mechanical Engineering*, *27*(1), 1-13.

[26] De la Torre, I. M., Montes, M. D. S. H., Flores-Moreno, J. M., & Santoyo, F. M. (2016). Laser speckle based digital optical methods in structural mechanics: A review. *Optics and Lasers in Engineering*, *87*, 32-58.

[27] Zhao, Q., Dan, X., Sun, F., Wang, Y., Wu, S., & Yang, L. (2018). Digital shearography for NDT: phase measurement technique and recent developments. *Applied Sciences*, *8*(12), 2662.

[28] Zhang, B., Zheng, X., Guo, B., Fang, S., Sia, B., & Yang, L. (2022). Sagnac interferometer based digital shearography for simultaneous dual sensitivity measurement. *Optics and Lasers in Engineering*, *152*, 106984.

[29] Lecompte, D., Bossuyt, S., Cooreman, S., Sol, H., & Vantomme, J. (2007, June). Study and generation of optimal speckle patterns for DIC. In *Proceedings of the annual conference and exposition on experimental and applied mechanics* (Vol. 3, pp. 1643-1649).

[30] Dong, Y. L., & Pan, B. (2017). A review of speckle pattern fabrication and assessment for digital image correlation. *Experimental Mechanics*, *57*(8), 1161-1181.

[31] Lankford, W. T. (1950). New criteria for predicting the performance of deep drawing sheets. *Trans. ASM*, *42*, 1197.

[32] Stickels, C. A., & Mould, P. R. (1970). The use of Young's modulus for predicting the plastic-strain ratio of low-carbon steel sheets. *Metallurgical Transactions*, *1*(5), 1303-1312.

[33] American Society for Testing and Materials. (2006). *ASTM E517-00: Standard test method for plastic strain ratio r for sheet metal*. ASTM International.

[34] Seiner, H., Bodnárová, L., Sedlák, P., Janeček, M., Srba, O., Král, R., & Landa, M. (2010). Application of ultrasonic methods to determine elastic anisotropy of polycrystalline copper processed by equal-channel angular pressing. *Acta Materialia*, *58*(1), 235-247.

[35] Huh, J., Kim, Y. J., & Huh, H. (2011, May). Measurement of R-values at intermediate strain rates using a digital speckle extensometry. In *Dynamic Behavior of Materials, Volume 1: Proceedings of the 2011 Annual Conference on Experimental and Applied Mechanics* (pp. 317-322). New York, NY: Springer New York.

[36] Xie, X., Li, J., Sia, B., Bai, T., Siebert, T., & Yang, L. (2017). An experimental validation of volume conservation assumption for aluminum alloy sheet metal using digital image correlation method. *The Journal of Strain Analysis for Engineering Design*, *52*(1), 24-29.

[37] Keeler, S. P. (1963). Backofen,". *Plastic Instability and Fracture in Sheets Stretched over Rigid Punches", Transaction of the ASM*, *56*, 25-48.

[38] Huang, M., & Cheng, H. (2015). Determination of all elastic and plastic parameters for sheets of cubic metals only by uniaxial tension tests. *European Journal of Mechanics-A/Solids*, *49*, 539-547.

[39] Zhang, C., Leotoing, L., Zhao, G., Guines, D., & Ragneau, E. (2011). A comparative study of different necking criteria for numerical and experimental prediction of FLCs. *Journal of Materials Engineering and Performance*, *20*, 1036-1042.

[40] Song, Y., Green, D. E., & Rose, A. (2020). Investigation of various necking criteria for sheet metal formability analysis using digital image strain data. *International Journal of Material Forming*, *13*, 1015-1024.

[41] Min, J., Stoughton, T. B., Carsley, J. E., & Lin, J. (2017). Comparison of DIC methods of determining forming limit strains. *Procedia Manufacturing*, *7*, 668-674.

[42] Martínez-Donaire, A. J., García-Lomas, F. J., & Vallellano, C. (2014). New approaches to detect the onset of localised necking in sheets under through-thickness strain gradients. *Materials & Design*, *57*, 135-145.

[43] Huang, G., Sriram, S., & Yan, B. (2008, June). Digital image correlation technique and its application in forming limit curve determination. In *Proceedings of the IDDRG 2008 International Conference* (pp. 153-162). International Deep Drawing Research Group, Olofström, Sweden.

[44] Min, J., Stoughton, T. B., Carsley, J. E., & Lin, J. (2017). A method of detecting the onset of localized necking based on surface geometry measurements. *Experimental Mechanics*, *57*, 521-535.

[45] Min, J., Stoughton, T. B., Carsley, J. E., & Lin, J. (2017). An improved curvature method of detecting the onset of localized necking in Marciniak tests and its extension to Nakazima tests. *International Journal of Mechanical Sciences*, *123*, 238-252.

[46] Shi, M. F., Pickett, K. M., & Bhatt, K. K. (1993). *Formability issues in the application of tailor welded blank sheets* (No. 930278). SAE technical paper.

[47] Zadpoor, A. A., Sinke, J., & Benedictus, R. (2007). Mechanics of tailor welded blanks: an overview. *Key Engineering Materials*, *344*, 373-382.

[48] Kinsey, B., & Wu, X. (Eds.). (2011). *Tailor welded blanks for advanced manufacturing*. Elsevier.

[49] Bishop, R. F., Hill, R., & Mott, N. F. (1945). The theory of indentation and hardness tests. *Proceedings of the Physical Society*, *57*(3), 147.

[50] Johnson, K. L. (1970). The correlation of indentation experiments. *Journal of the Mechanics and Physics of Solids*, *18*(2), 115-126.

[51] Cheng, Y. T., & Cheng, C. M. (2004). Scaling, dimensional analysis, and indentation measurements. *Materials Science and Engineering: R: Reports*, *44*(4-5), 91-149.

[52] Arunkumar, S. (2018). A review of indentation theory. *Materials Today: Proceedings*, *5*(11), 23664-23673.

[53] Pavlina, E. J., & Van Tyne, C. J. (2008). Correlation of yield strength and tensile strength with hardness for steels. *Journal of materials engineering and performance*, *17*, 888-893.

[54] Lockwood, W. D., Tomaz, B., & Reynolds, A. P. (2002). Mechanical response of friction stir welded AA2024: experiment and modeling. *Materials Science and Engineering: A*, *323*(1-2), 348-353.

[55] Liu, S., & Chao, Y. J. (2004). Determination of global mechanical response of friction stir welded plates using local constitutive properties. *Modelling and Simulation in Materials Science and Engineering*, *13*(1), 1.

[56] Li, G., Xu, F., Sun, G., & Li, Q. (2014). Identification of mechanical properties of the weld line by combining 3D digital image correlation with inverse modeling procedure. *The International Journal of Advanced Manufacturing Technology*, *74*, 893-905.

[57] Saranath, K. M., Sharma, A., & Ramji, M. (2014). Zone wise local characterization of welds using digital image correlation technique. *Optics and Lasers in Engineering*, *63*, 30-42.

[58] Bai, R., Wei, Y., Lei, Z., Jiang, H., Tao, W., Yan, C., & Li, X. (2018). Local zone-wise elastic-plastic constitutive parameters of Laser-welded aluminium alloy 6061 using digital image correlation. *Optics and Lasers in Engineering*, *101*, 28-34.

[59] Sun, P. Y., Zhu, Z. K., Su, C. Y., Lu, L., Zhou, C. Y., & He, X. H. (2019). Experimental characterisation of mechanical behaviour for a TA2 welded joint using digital image correlation. *Optics and Lasers in Engineering*, *115*, 161-171.

[60] Peng, B., Zhang, M., & Ye, D. (2022). DIC/DSI based studies on the local mechanical behaviors of HR3C/T92 dissimilar welded joint during plastic deformation. *Materials Science and Engineering: A*, *857*, 144073.

[61] Yan, R., Xin, H., Yang, F., El Bamby, H., Veljkovic, M., & Mela, K. (2022). A method for determining the constitutive model of the heat-affected zone using digital image correlation. *Construction and Building Materials*, *342*, 127981.

[62] Yamaguchi, I. (1981). Speckle displacement and decorrelation in the diffraction and image fields for small object deformation. *Optica Acta: International Journal of Optics*, *28*(10), 1359-1376.

[63] Feiel, R., & Wilksch, P. (2000). High-resolution laser speckle correlation for displacement and strain measurement. *Applied Optics*, *39*(1), 54-60.

[64] Mashiwa, N., Furushima, T., & Manabe, K. (2017). Novel non-contact evaluation of strain distribution using digital image correlation with laser speckle pattern of low carbon steel sheet. *Procedia Engineering*, *184*, 16-21.

[65] Song, J., Yang, J., Liu, F., & Lu, K. (2018). High temperature strain measurement method by combining digital image correlation of laser speckle and improved RANSAC smoothing algorithm. *Optics and Lasers in Engineering*, *111*, 8-18.

[66] Yali, D. O. N. G. (2025). High-temperature deformation measurement using optical imaging digital image correlation: Status, challenge and future. *Chinese Journal of Aeronautics*, 103472.

[67] Sjödahl, M., & Benckert, L. R. (1994). Systematic and random errors in electronic speckle photography. *Applied Optics*, *33*(31), 7461-7471.

[68] Su, Y., & Zhang, Q. (2022). Glare: A free and open-source software for generation and assessment of digital speckle pattern. *Optics and Lasers in Engineering*, *148*, 106766.

[69] Oulamara, A., Tribillon, G., & Duvernoy, J. (1989). Biological activity measurement on botanical specimen surfaces using a temporal decorrelation effect of laser speckle. *Journal of Modern Optics*, *36*(2), 165-179.

[70] Hrabovsky, M. (1998, July). Theory of speckle displacement and decorrelation: application in mechanics. In *Laser Interferometry IX: Applications* (Vol. 3479, pp. 345-354). SPIE.

[71] Bruno, L., Pagnotta, L., & Poggialini, A. (2000). Laser speckle decorrelation in NDT. *Optics and lasers in engineering*, *34*(1), 55-65.

[72] Kobayashi, K., & Yamaguchi, I. (2011). High Accuracy and Wide Temperature Measurement by Non-Contact Speckle Extensometer. *Strain*, *47*, e98-e103.

[73] Paris, R., Thurner, T., & Schitter, G. (2013). Compensation based displacement measurement using objective laser speckles. *IFAC Proceedings Volumes*, *46*(5), 264-270.

[74] Anwander, M., Weiss, B., Zagar, B., & Weiss, H. (1999). A laser speckle correlation method for strain measurements at elevated temperatures. In *Local Strain and Temperature Measurement* (pp. 49-58). Woodhead Publishing.

[75] Pan, B., Dafang, W., & Yong, X. (2012). Incremental calculation for large deformation measurement using reliability-guided digital image correlation. *Optics and Lasers in Engineering*, *50*(4), 586-592.

[76] Zhang, X., Chi, Y., Yu, L., Wang, Q., & Pan, B. (2024). Laser speckle DIC revisited: an improved calculation scheme for large deformation measurement. *Optics & Laser Technology*, *168*, 109913.

[77] Green, S. F. (1986). Acoustic temperature & velocity measurement in combustion gases. In *International Heat Transfer Conference Digital Library*. Begel House Inc.

[78] Childs, P. R., Greenwood, J. R., & Long, C. A. (2000). Review of temperature measurement. *Review of scientific instruments*, *71*(8), 2959-2978.

[79] Jaremkiewicz, M. (2017). Accurate measurement of unsteady state fluid temperature. *Heat and Mass Transfer*, *53*(3), 887-897.

[80] Raffel, M., Richard, H., & Meier, G. E. A. (2000). On the applicability of background oriented optical tomography for large scale aerodynamic investigations. *Experiments in Fluids*, *28*(5), 477-481.

[81] Iffa, E. D., Aziz, A. R. A., & Malik, A. S. (2011). Gas flame temperature measurement using background oriented schlieren. *Journal of Applied Sciences*, *11*(9), 1658-1662.

[82] Tokgoz, S., Geisler, R., Van Bokhoven, L. J. A., & Wieneke, B. (2012). Temperature and velocity measurements in a fluid layer using background-oriented schlieren and PIV methods. *Measurement Science and Technology*, *23*(11), 115302.

[83] Raffel, M. (2015). Background-oriented schlieren (BOS) techniques. *Experiments in Fluids*, *56*, 1-17.

[84] Moumen, A., Grossen, J., Ndindabahizi, I., Gallant, J., & Hendrick, P. (2020). Visualization and analysis of muzzle flow fields using the background-oriented schlieren technique. *Journal of Visualization*, *23*, 409-423.

[85] Shimazaki, T., Ichihara, S., & Tagawa, Y. (2022). Background oriented schlieren technique with fast Fourier demodulation for measuring large density-gradient fields of fluids. *Experimental Thermal and Fluid Science*, *134*, 110598.

[86] Ichihara, S., Shimazaki, T., & Tagawa, Y. (2022). Background-oriented schlieren technique with vector tomography for measurement of axisymmetric pressure fields of laser-induced underwater shock waves. *Experiments in Fluids*, *63*(11), 182.

[87] Li, Y., Ren, Y., Mei, H., Ye, S., Tao, Z., Liu, S., ... & Rao, R. (2024). Background-oriented schlieren experimental and simulation study of the effect of sidewalls on optical turbulence anisotropy in a thermal convection turbulence simulator. *Optics & Laser Technology*, *177*, 111214.

[88] Reuss, D. L. (1983). Temperature measurements in a radially symmetric flame using holographic interferometry. *Combustion and Flame*, *49*(1-3), 207-219.

[89] Shakher, C., & Nirala, A. K. (1994). Measurement of temperature using speckle shearing interferometry. *Applied optics*, *33*(11), 2125-2127.

[90] Morad, M. R., Momeni, A., Fordoei, E. E., & Ashjaee, M. (2016). Experimental and numerical study on heat transfer characteristics for methane/air flame impinging on a flat surface. *International Journal of Thermal Sciences*, *110*, 229-240.

[91] Jiao, T., Meng, H., Deng, S., Liu, S., Wang, X., Wei, Z., ... & Huang, X. (2019). Simultaneous measurement of refractive index and temperature using a Mach-Zehnder

interferometer with forward core-cladding-core recoupling. *Optics & Laser Technology*, *111*, 612-615.

[92] Tong, R. J., Zhao, Y., Hu, H. F., & Qu, J. F. (2020). Large measurement range and high sensitivity temperature sensor with FBG cascaded Mach-Zehnder interferometer. *Optics & Laser Technology*, *125*, 106034.

[93] Handel, H. (2007). Analyzing the influences of camera warm-up effects on image acquisition. In *Computer Vision–ACCV 2007: 8th Asian Conference on Computer Vision, Tokyo, Japan, November 18-22, 2007, Proceedings, Part II 8* (pp. 258-268). Springer Berlin Heidelberg.

[94] Ma, S., Pang, J., & Ma, Q. (2012). The systematic error in digital image correlation induced by self-heating of a digital camera. *Measurement Science and Technology*, *23*(2), 025403.

[95] Pan, B., Shi, W., & Lubineau, G. (2015). Effect of camera temperature variations on stereo-digital image correlation measurements. *Applied optics*, *54*(34), 10089-10095.

[96] Owner-Petersen, M. (1991). Decorrelation and fringe visibility: on the limiting behavior of various electronic speckle-pattern correlation interferometers. *Journal of the Optical Society of America A*, *8*(7), 1082-1089.

[97] Nazarchuk, Z. T., Muravsky, L. I., & Kuts, O. G. (2022). Nondestructive testing of thin composite structures for subsurface defects detection using dynamic laser speckles. *Research in Nondestructive Evaluation*, *33*(2), 59-77.